RADIO FREQUENCY HEATING OF CARBON-BASED NANOMATERIAL FILMS

A Dissertation

by

MUHAMMAD ANAS

Submitted to the Office of Graduate and Professional Studies of
Texas A&M University
in partial fulfillment of the requirements for the degree of

DOCTOR OF PHILOSOPHY

Chair of Committee,	Micah J. Green
Committee Members,	Mohammad Naraghi
	Mustafa Akbulut
	Sreeram Vaddiraju
Head of Department,	Arul Jayaraman

August 2021

Major Subject: Chemical Engineering

ABSTRACT

Electromagnetic (EM) energy-induced heating of carbon-based materials has opened up novel routes in material synthesis and processing applications. Three-dimensional (3D) printed parts with strengths similar to bulk polymers are now possible due to rapid locally-induced radio frequency (RF) heating and welding of 3D printed interfaces. Automotive and aerospace assembly lines can be improved and sped up due to RF-induced curing to green strength of adhesives loaded with carbon nanomaterials. The flexibility in RF applicator designs to induce heating in a non-contact manner has also extended applications to synthesis of industrially-important ceramics such as silicon carbide. The applicable areas are wide-ranging and continue to increase; however, the fundamental understanding of the phenomenon is still limited and needs to be explored to further develop and improve the efficiency of the new processes.

It is known that electrical conductivity is required for RF heating of carbon-based materials. However, it is not well understood how RF heating rates vary with conductivity and if the pattern is generalizable for all types of RF susceptor-loaded structures. The goal of this work is to contribute to the fundamental understanding of the RF heating phenomenon and also extend its applications to other relevant areas.

In this work, we first show that the RF heating of semiconducting single-walled carbon nanotubes is significantly higher than that of the metallic single-walled carbon nanotubes primarily due to differences in electrical conductivity. Next, we confirm using experiments and simulation that the RF heating is non-monotonically related with the

electrical conductivity; the trend is similar at high frequencies and is universal for a range of carbon-based nanomaterials and their composites. We also demonstrate that RF heating response of carbon-based nanomaterials can be used to detect faults in printed carbon nanotube circuits which allows for rapid screening of nanomaterial-based electronics. Lastly, we show techniques to generate thermal patterns using direct current (DC) and alternating current (AC)-based heating of carbon.

ACKNOWLEDGEMENTS

Bismillah (In Allah's name)

I would like to acknowledge my advisor, Dr. Micah Green, for his contribution in my growth as a professional researcher. I greatly admire his effort in helping students in times of need, be it professional or personal. I would like to also thank my committee members: Dr. Mohammad Naraghi, Dr. Mustafa Akbulut, and Dr. Sreeram Vaddiraju for their feedback on my research work. I would like to also mention Dr. Mohammed Saed of Texas Tech University for his input on my work.

Thanks also go to my friends and colleagues and the department faculty and staff for making my time at Texas A&M University a great experience. Special thanks to Dr. Wanmei Sun, Dr. Smit Shah, Dr. Touseef Habib, Dr. Nutan Patil, and Dr. Martin Pospisil for helping me during my early years in the research group. Thanks also go to Victoria Hicks, Erin Porter, Aida Khalfaoui, Daniel Carey, Dr. Mazin Mustafa, Xiaofei Zhao, Julie Oh, Anubhav Sarmah, and Debopamaa Debnath for their input and contributions to my research work.

Finally, thanks to my mother, father, and siblings for their encouragement, patience, and love.

CONTRIBUTORS AND FUNDING SOURCES

Contributors

This work was supervised by a dissertation committee consisting of Professors Micah Green (advisor), Mustafa Akbulut, and Sreeram Vaddiraju of the Department of Chemical Engineering, and Professor Mohammad Naraghi of the Department of Aerospace Engineering.

The dispersions of semiconducting and metallic single-walled carbon nanotubes and their characterization data in Chapter 2 were provided by Dr. Yang Zhao of Dr. Kirk J. Zeigler's research group at the University of Florida. The carbon nanofiber-polyamide composite samples and printed carbon nanotube samples were provided by Dr. Eftihia Barnes and Dr. Lee Moores, respectively. The carbon nanostructures-polycarbonate composite samples were provided by Cabot Corporation. The simulation data in Chapter 3 and Chapter 5 were provided by Dr. Mazin Mustafa. The printed samples used for experiments in Chapter 4 were provided by Brewer Science, Inc. The discussion of results in Chapter 4 was provided by Victoria Hicks. The sandblasted paint samples in Appendix A were provided by Erik Alberts.

Funding Sources

Graduate study was supported by an assistantship from Texas A&M University department of chemical engineering and the research work was funded by the U.S. Army Engineer Research and Development Center (ERDC) in Vicksburg, MS under cooperative agreements W912HZ-17-2-0007 and W912HZ-18-BAA-01.

TABLE OF CONTENTS

Page

LIST OF FIGURES

Page

LIST OF TABLES

Page

CHAPTER I

INTRODUCTION

Carbon-based Nanomaterials

Carbon is a unique element due to its ability to form covalent bonds with various hybridization states (sp, sp^2, sp^3). Diamond and graphite are both naturally occurring carbon-based materials which have remarkable differences in their properties due to the nature of the covalent bonds between their carbon atoms. Diamond (sp^3 covalent bonds) is hard, transparent, and an electrical insulator while graphite (sp^2 covalent bonds) is soft, opaque, and an electrical conductor.[1-2] Over the years, many new forms of carbon with dimensions at the nanoscale (1-100 nm) have been identified which have expanded the applications of carbon to a wide range of technologies. Fullerene, C_{60}, was the first carbon nanomaterial to be discovered in 1985.[3] Six years later, in 1991, carbon nanotubes (CNTs) were discovered by Iijima.[4] Graphene is the most recently isolated carbon-based nanomaterial by Andre Geim and Konstantin Novoselov in 2004.[5] CNTs and graphene have attracted the most attention due to their interesting and surprising properties.

CNTs are tubular structures and can be envisioned as rolled up sheets of graphene with shells based on hexagonal lattice of sp^2 carbon atoms as depicted in **Figure I-1**.[6] An individual CNT and a single layer graphene have Young's modulus of around 1.0 TPa [7-8] which makes them the strongest known materials. Single-walled carbon nanotubes (SWCNTs) have diameters around 1 nm and lengths in the micrometer scale making them the most anisotropic materials (aspect ratio exceeding 10,000) and thus flexible.[1, 9] CNTs

can be double-walled (DW) as well as multi-walled (MW) with significant differences in diameters compared to SWCNT which can also lead to differences in their mechanical and electrical properties.[10]

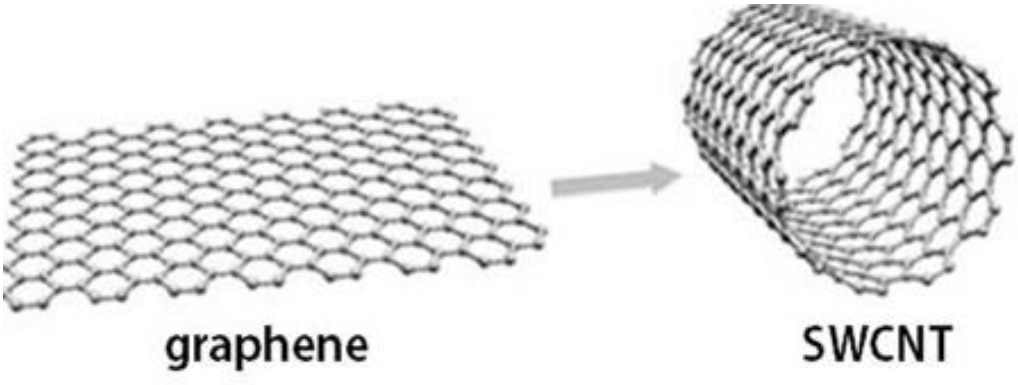

Figure I-1. Graphene and single-walled carbon nanotube (SWCNT).[6]

CNTs and graphene also show unique electrical characteristics. A single layer graphene sheet is considered to be a zero band gap semiconductor or semimetal with carrier mobility reported as high as 2 x 10^5 cm^2 V^{-1} s^{-1}.[11-12] CNTs also share these properties; however, in addition to the diameter, chirality (the angle between the hexagon and the tube axis) is an important parameter to understand electrical properties of CNTs. Depending on the chirality, CNTs can be arranged in armchair, chiral, or zigzag configurations with different electrical behavior and are described by integers (*n*,*m*) related to the chiral vector. For example, armchair (*n*=*m*) CNTs exhibit metallic behavior, chiral (*n*-*m* is a multiple of 3) exhibit semiconducting behavior, and zigzag (*m=0*) exhibit either metallic or semiconducting behavior (**Figure I-2**).[10, 13] The high carrier mobility in graphene and CNTs and the ability to tune the electrical properties of CNTs is one of the extensively studied areas in academia and industry.[14]

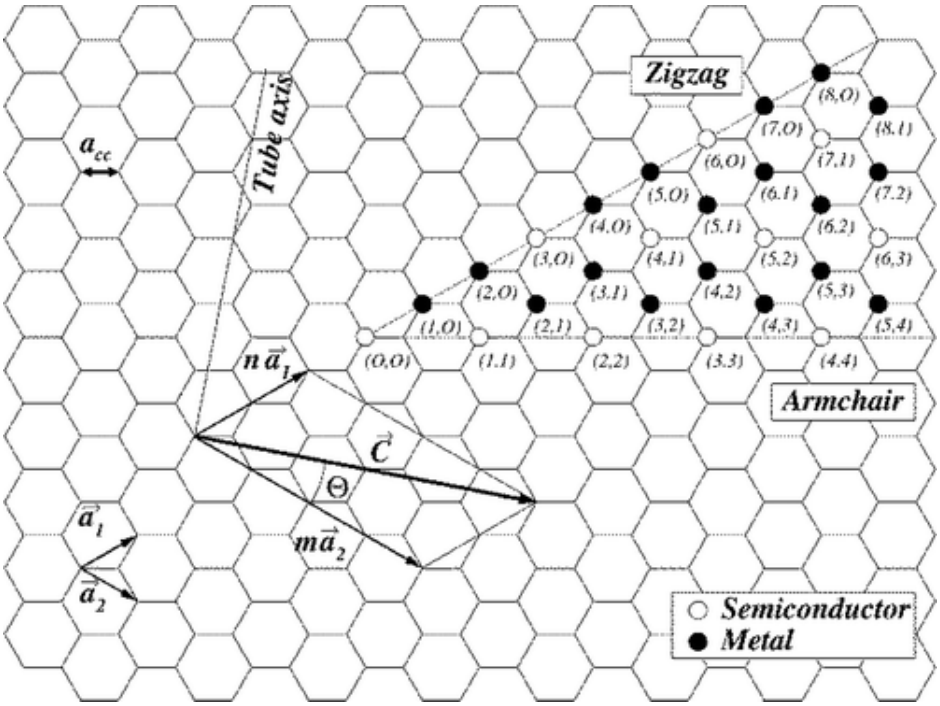

Figure I-2. Schematic of the graphene sheet showing the chirality in SWCNTs. Chiral vector, C = na$_1$ + ma$_2$, where n and m are integers and a$_1$ and a$_2$ are the unit cell vectors of the two-dimensional hexagonal graphene sheet. The chiral angle is the angle between the chiral vector and the zigzag axis. Reprinted with permission from reference [10], Copyright 2005 Elsevier Ltd.

Most of the applications of carbon-based nanomaterials rely on the bulk properties of the ensemble rather than that of an individual nanoparticle.[15] Films of nanomaterials provide reproducible properties due to the statistical averaging of the individuals and both dry and wet processing methods are being employed to fabricate films.

Dry film processing methods usually involves the chemical vapor deposition (CVD) system which provide films of high quality with low defect density; however, the process is not scalable.[16] Nerushev *et al.*[17] was able to fabricate aligned multi-walled CNT films of only 2.0 cm x 2.0 cm using a CVD method with iron (Fe) catalysts. Hsu *et al.*[18] was able to synthesize the CNT films with maximum area of 10 cm x 10 cm using cobalt

(Co) catalyst in a CVD system. High quality graphene sheets can also be directly synthesized on a metal substrate with the CVD method; however, the costs associated with the CVD system can be significantly high.[19-20]

Solution-based film processing methods are low cost and easily scalable. A nanomaterial dispersion can be processed into films via vacuum filtration, spray coating, or printing.[19, 21] Wu *et al.*[22] fabricated a transparent SWCNT film of 10 cm diameter using vacuum filtration of a dilute surfactant-based suspension and then washed away the surfactant with water. Shobin *et al.*[23] spray coated SWCNT dispersions to make 5 cm x 5 cm transparent films. Additionally, printing of CNT and graphene dispersions has also allowed for large area rapid production of nanomaterial-based devices such as transistors,[24-25] sensors,[26] and supercapacitors.[27]

Carbon-based nanomaterials may also be mixed with polymers to synthesize composites of both high and low nanomaterial content for various applications. In the high-nanomaterial content limit, Li *et al.*[28] fabricated a composite by infiltrating polyphenylene resin into a CNT buckypaper with final buckypaper loading of 60 wt.%. The composite showed improvement in tensile strength, Young's modulus, thermal conductivity, and thermoelectric power compared to those of resin and bucky paper individually. Yee *et al.*[29] and Mehmood *et al.*[30] synthesized CNT and graphene buckypaper composites, respectively, by infiltrating polyvinyl alcohol (PVA) and demonstrated that the composites with 65 wt.% CNT and 60 wt.% graphene buckypapers can be used for strain sensing applications. On the other hand, small amount of nanomaterials can also significantly affect the properties of the polymers. For example,

Kashiwagi *et al.*[31] showed that addition of 2.0 wt.% CNTs improved the thermal degradation and flammability of poly propylene. Najafi *et al.*[32] synthesized thin films of poly methyl methacrylate (PMMA)-CNT and showed that 0.5 wt.% CNT-PMMA nanocomposite film degraded slower in the UV ozone and electron beam radiations compared to pure PMMA. Kim *et al.*[33] improved the thermoelectric performance by 10 times of poly(3,4-ethylenedioxythiophene) poly(styrenesulfonate) (PEDOT : PSS) thin films by adding 2.0 wt.% graphene. Even though carbon-based nanomaterials are being explored to enhance a wide range of material properties, the impact of nanomaterials is often focused on these materials' outstanding electrical properties.[34]

Electrical conductivity of individual CNT and a graphene sheet can be in the range of 10^6-10^8 S/m which is comparable to the conductivity of the two best metallic conductors, silver and copper. However, electrical properties of the pure nanomaterial film is affected by the type of the individual nanomaterial as well as the assembly of the individual nanomaterials.[35] There are efforts to improve the electrical properties of the ensemble. SWCNTs can now be sorted by lengths, diameter, and chirality.[36-37] The assembly of CNTs and graphene into films can also be tailored by controlling the dispersion quality, by altering the conditions during the nanomaterial synthesis to increase purity, or by adding functionalities.[38-39]

For electrical properties of nanocomposite films, it is important to consider the loading of nanomaterials in the matrix. As the loading increases, the electrical conductivity does not increase linearly; instead, at a certain nanomaterial concentration, the electrical conductivity abruptly increases and the composite transitions from an insulator to an

electrical conductor (**Figure I-3a**).[40] This is known as percolation, and the onset of the jump in electrical conductivity is termed the percolation threshold.[35, 41] At the percolation, the individual nanomaterials such as CNTs or graphene sheets are in contact with each other and forms a conductive pathway (**Figure I-3b**), thus significantly improving the conductivity of the composite.[42] CNTs have very large aspect ratios, and the sheet-like structure of graphene similarly allows for very small percolation thresholds; this makes both CNTs and graphene ideal nanofillers.[43-44]

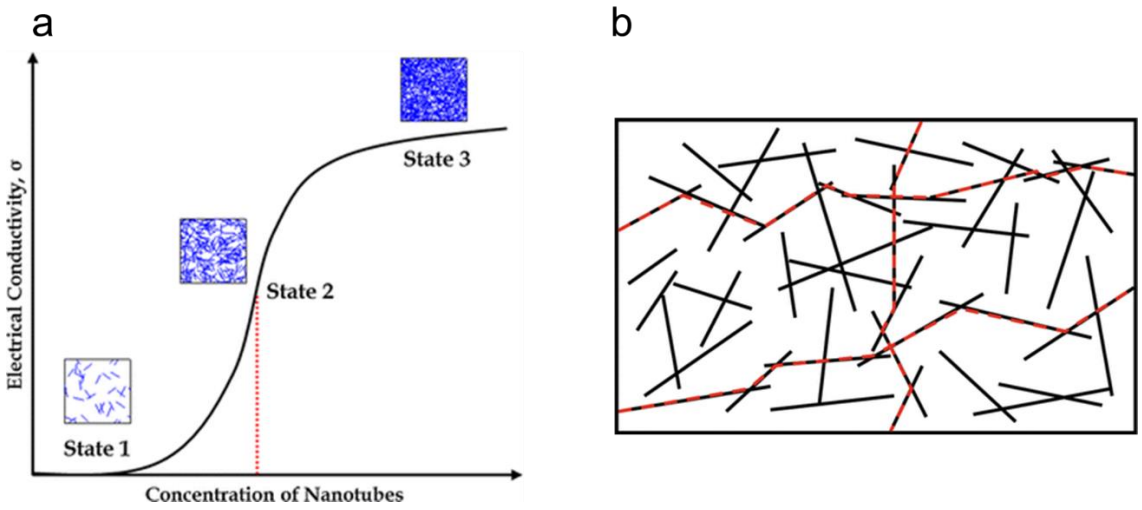

Figure I-3. (a) Electrical conductivity as a function of nanotube concentration showing percolation (State 2), Reprinted by permission from Springer Nature reference [40], Copyright 2015 Springer Science Business Media New York. (b) The dispersion of carbon-based fillers in a matrix with the percolating pathways (dashed red lines), reprinted by permission from Springer Nature, Springer Ebook reference [35], Copyright 2018 Springer International Publishing AG.

Carbon Nanomaterials' Interaction with Electric Fields

Alternating current (AC) electric fields can be used to induce currents in electrically conductive films of nanomaterials and their composites, thus resulting in rapid heating of the materials. Microwave heating is an example of electric field-induced heating which utilizes energy in the range of 300 MHz – 300 GHz to rapidly heat the material.[45-46] Higginbotham *et al.*[47] added 0.75 wt.% MWCNTs to preceramic polymer and used microwave (2.45 GHz) heating to rapidly cure the composite by reaching 500 °C within 1 min at low powers (30-40 W). Rangari *et al.*[48] showed that adding 0.2 wt.% CNTs to epoxy and curing in the microwave oven for 10 min improved the strength of the cured epoxy by 17% compared to neat epoxy cured for 8 hours in a conventional oven. Sweeney *et al.*[49] demonstrated that unusual heating response of CNTs in response to microwave (2.45 GHz) exposure can be used to locally weld interfaces in the three-dimensionally (3D) printed parts. Haile *et al.*[50] showed enhanced microwave absorption and rapid heating and cooling in layer-by-layer thin films of CNTs and poly(diallyldimethyl ammonium chloride). In addition to microwave heating, frequencies in the range of 1-300 MHz can also be used to capacitively couple electric fields with the materials for rapid heating (**Figure I-4**).[51] The lower range or Radio frequency (RF) heating has mostly been used for drying of food and wood[51] and for hyperthermia applications.[52] However, recently, our group has shown tremendous potential of RF heating in a range of applications such as continuous carbon nanofiber (CNF)/epoxy and CNT/epoxy pre-preg manufacturing,[53] rapid curing and pyrolysis of preceramic polymers,[54] and thermoplastic welding.[55-56]

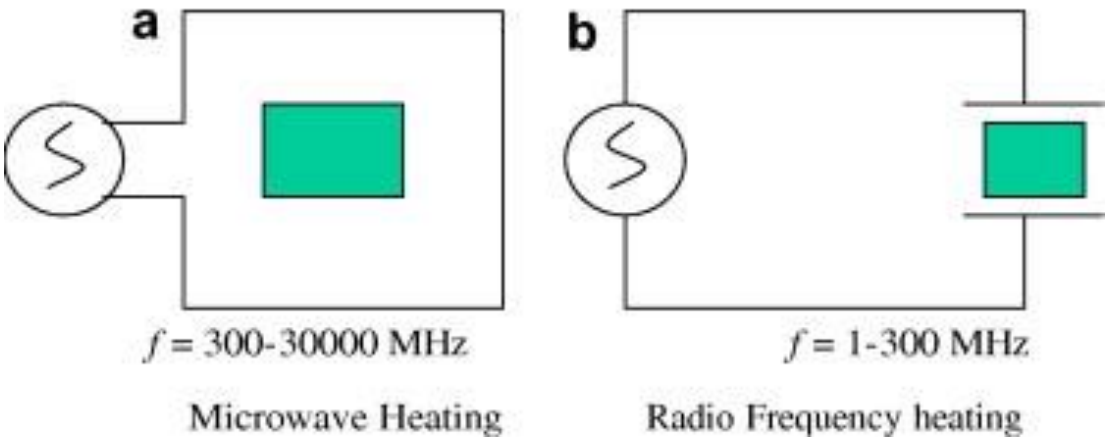

Figure I-4. Schematic of (a) microwave (MW) and (b) radio frequency (RF) heating of a sample (green). Reprinted with permission from reference [51], Copyright 2009 Elsevier Ltd.

RF heating of carbon-based nanomaterial films has shown a number of surprising features, including frequency-dependent heating and a non-monotonic relationship between nanomaterial coverage/loading and heating behavior. For example, Sweeney *et al.*[57] observed that the RF heating of CNT-polylactide (CNT-PLA) composite films increased up to a certain CNT concentration and then decreased with further increase in concentration. These are interesting findings and it is not well understood how RF heating rates vary with conductivity and if the trend is applicable to other types of carbon-based nanomaterials. Remote, localized, and rapid RF heating of carbon-based materials also present great opportunity for disrupting conventional technologies in a variety of areas.

Summary of Dissertation

This dissertation provides understanding of the underlying science associated with the RF heating of carbon-based nanomaterials as well as show some exciting applications of the RF heating phenomenon. Chapter II investigates the RF heating of chirality-sorted metallic and semiconducting single-walled carbon nanotubes. Chapter III shows via experiments and simulations the universal trends in RF heating associated with carbon-based nanomaterials. Chapter IV demonstrates development of a novel method to characterize printed carbon nanotube circuits using RF heating. Chapter V confirms that the underlying science of RF heating is similar for MW heating of carbon-based materials which can be used to generate thermal patterns.

CHAPTER II

RADIO FREQUENCY HEATING OF METALLIC AND SEMICONDUCTING SINGLE-WALLED CARBON NANOTUBES*

Introduction

Carbon Nanotubes (CNTs) possess exceptional properties such as high strength, thermal conductivity, and electrical conductivity which have led to their widespread use in advanced composites,[58-59] energy storage devices,[60-61] filtration membranes,[62-63] multifunctional fabrics,[64-65] and most importantly high-performance electronics.[66-68]

Single-walled carbon nanotubes (SWCNTs) have tunable electronic properties which make them far more valuable in high-performance electronics compared to their multi-walled analogues.[69-72] If a SWCNT is conceived as a rolled-up sheet of graphene, then the rolling direction is defined by chirality. Depending on this chirality, the electronic band structure of SWCNTs can be either metallic (m-) or semiconducting (s-).[73-75]

The typical synthesis of SWCNTs results in a complex mixture of m- and s-SWCNTs but many methods have already been developed to separate these fractions.[76-79] The successful purification of m- and s-SWCNTs has expanded their applications to nanoelectronics.[72, 80-81] The m-SWCNTs could be used as interconnects allowing higher current densities than copper and aluminum.[82-83] The s-SWCNTs with tunable energy

---

* Reprinted with permission from "Radio frequency heating of metallic and semiconducting single-walled carbon nanotubes" by Muhammad Anas; Yang Zhao; Mohammad A. Saed; Kirk J. Ziegler; Micah J. Green. 2019, *Nanoscale*, 11, 9617-9625, Copyright 2019 The Royal Society of Chemistry.

bandgaps could offer miniaturization of electronic devices such as transistors and sensors.[70, 84-87] Although there has been interest in fabricating devices that use individual SWCNT as components, SWCNT films are preferred in electronics as an alternative configuration to directly-grown individual SWCNTs due to their ease of fabrication and reproducible characteristics.[66, 88-92] For example, s-SWCNT films have already been used in thermoelectric devices,[93] field effect transistors (FETs),[94-95] and diodes.[80, 96] Additionally, thin films of m-SWCNT and s-SWCNT can be applied as conductive coatings in photovoltaics [97], electrochromic devices [98], and flat panel displays.[99-100]

All these SWCNT-based devices are either used in circuits for radio frequency (RF) applications or could possibly interact with electric fields (E-field) at RF frequencies during operation.[81, 101] Therefore, it is of great importance to probe the interaction of m- and s-SWCNTs with RF fields since these interactions are not well understood. Prior work on this front is mostly focused on dilute SWCNT dispersions, particularly in medical applications.[52, 102] For example, Gannon *et al.*[52] used RF energy to induce heating in aqueous SWCNT samples. They injected 500 mg/L mixed SWCNTs suspension into rabbit tissues and applied RF power of 600 W at 13.56 MHz to heat the suspension at 8 °C/s. This locally-induced heating of SWCNTs successfully destroyed the tumor cells. The only study that differentiates the response of m-SWCNT and s-SWCNT when exposed to RF fields is by Corr *et al.*[102]. In this study, the interaction of RF fields with 95% pure m-SWCNT and 95% pure s-SWCNT dispersions was investigated at the operating frequency of 13.56 MHz. It was reported that 100 mg/L dispersions of m- and s-SWCNT heated at 0.20 °C/s and 0.35 °C/s, respectively, at RF power of 500 W. The

same study also stated that the presence of a conductive host such as NaCl in dispersions did not enhance the heating rate but rather diminished the electric fields near m- and s-SWCNTs.

Recently, our group has shown that multi-walled carbon nanotube (MWCNT)-loaded polymer composites can directly couple with electric fields at RF frequencies (1-200 MHz) and rapidly heat via Joule heating. We demonstrated different RF electric field applicator configurations such as direct-contact, parallel plate, and interdigitated fringing-field for heating MWCNT-loaded composites. We observed heating rates of 16 °C/s for 5 wt.% MWCNT composites at RF power as low as 10 W.[57] Our RF heating technique cured thermosets faster compared to conventional oven-based curing due to localized volumetric heating. We also applied our technique to rapidly cure thermoset adhesives in metal-metal bonding and assembled an automotive structure. These findings also have applications to curing of thermoset adhesives in plastic-plastic bonding and welding of 3D-printed plastic structures. However, it is not yet understood how m- and s-SWCNTs would behave in the context of RF heating. Delineating how these SWCNTs differ would aid in understanding the effect of m- and s- shells in MWCNTs as well.

In this work, we investigate the heating response of m- and s-SWCNT films to applied RF energy. We successfully separate high-purity m- and s-SWCNTs fractions from an initial SWCNTs mixture and fabricate thin films of low areal densities. We measure electrical properties of the films and use a fringing-field RF applicator to heat the films. We show rapid and non-contact coupling of RF electrical fields with the films and observe heating with high heating rates. We find that RF heating rate scales inversely with

the bulk DC conductivity of the film. The more conductive m-SWCNT films reflect RF fields and heat at lower rates compared to s-SWCNT films. We also observe that the presence of impurities lowers the overall conductivity of m-SWCNT films, which significantly increases the heating rate. Our findings suggest that RF heating could be used as a metric for film purity, and that RF heating may occur in SWCNT-based electronics.

Results and Discussion

We obtained high-purity m- and s-SWCNTs by first injecting an initial SWCNT dispersion into a Sepharose hydrogel-packed chromatography column, and then separating the fractions through elution with different surfactant solutions. **Figure II-1** shows the diameter distribution of initial SWCNT dispersion. The m-SWCNTs were collected first through elution with 1 wt. % aqueous SDS solution and concentrated to 5.10 ppm. A small fraction of m-SWCNTs was also obtained after SDS to DOC surfactant exchange process and concentrated to 2.71 ppm. Finally, the s-SWCNTs were collected through elution with 1 wt. % aqueous DOC solution and concentrated to 11.7 ppm. **Figure II-2** shows images of initial SWCNT dispersion, m-SWCNT SDS-based dispersion, and s-SWCNT DOC-based dispersion. The differences between these samples is clearly noticed from different colors. The initial SWCNT dispersion has a black color, the separated m-SWCNT dispersion has a red color, and the s-SWCNT dispersion has a green color.

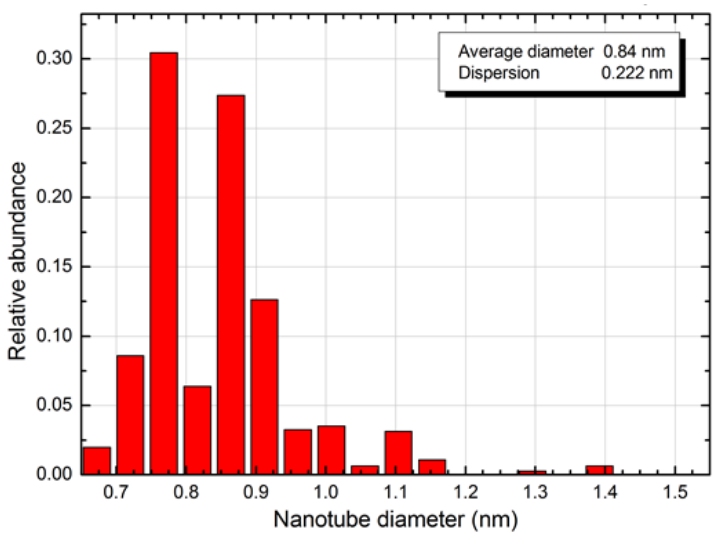

Figure II-1. Diameter distribution of initial SWCNT dispersion using fluorescence analysis. Reprinted with permission from reference [103], Copyright 2019 The Royal Society of Chemistry.

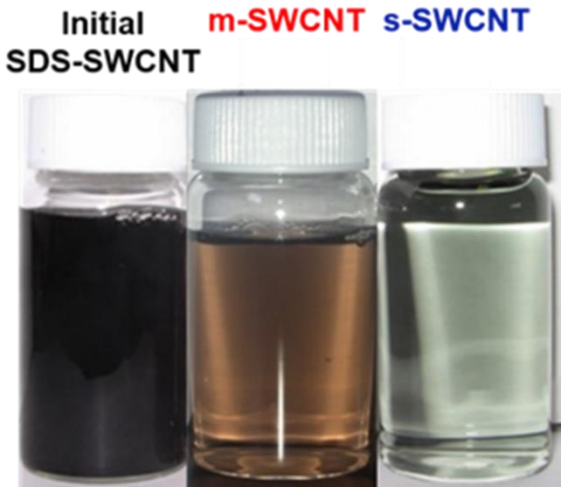

Figure II-2. Images of initial SWCNT dispersion, m-SWCNT SDS-based dispersion, and s-SWCNT DOC-based dispersion. Reprinted with permission from reference [103], Copyright 2019 The Royal Society of Chemistry.

Figure II-3 shows the normalized absorption spectra of s-SWCNTs dispersed in aqueous DOC solution, and m-SWCNTs dispersed in aqueous DOC and SDS solutions, respectively. The absorption in the S_{11} and S_{22} bands of s-SWCNTs dispersed in DOC

solution indicates that this SWCNT dispersion contains major s-SWCNT species. This is because the regions labeled S_{11} and S_{22} correspond to excitonic absorption bands of s-SWCNTs due to first and second one-dimensional van Hove singularities (vHS), respectively.[104] In addition, fluorescence spectra (**Figure II-4**) further confirms the presence of different s-SWCNT species in the dispersion. On the other hand, the absorption in the M_{11} band of m-SWCNTs dispersed in DOC and SDS solutions indicates that these SWCNT dispersions are concentrated with m-SWCNTs because the M_{11} region corresponds to the absorption band of m-SWCNTs.[104] The purities of dispersions were calculated based on areas of the M_{11} and S_{22} bands. The s-SWCNT dispersion purity is nearly 100% while the m-SWCNT dispersions have purities of around 90-98%. The purity can be further increased by using higher concentration of initial SWCNTs dispersion and selecting other high-throughput hydrogels such as Sephacryl 100 HR or 200 HR for separation [105-106]. Note that the absorption peaks due to s-SWCNT impurities are also observed for the DOC-based dispersion of m-SWCNTs.

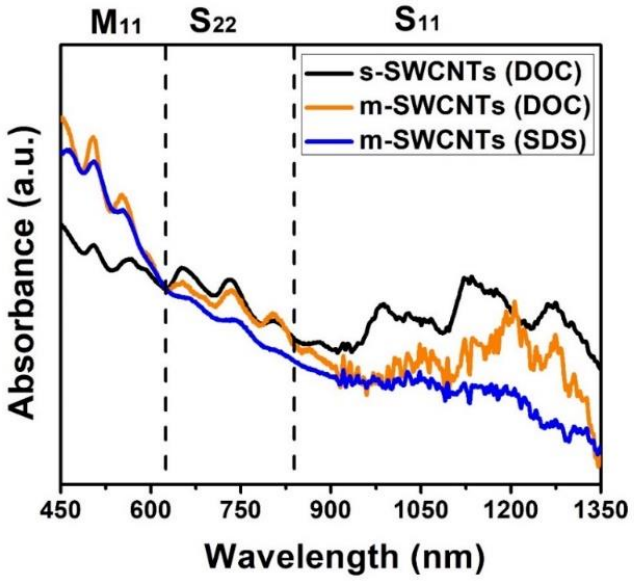

Figure II-3. Normalized absorbance spectra (λ = 626 nm) of 11.7 ppm s-SWCNTs dispersed in DOC solution, 2.71 ppm m-SWCNTs dispersed in DOC solution, and 5.10 ppm m-SWCNTs dispersed in SDS solution. Reprinted with permission from reference [103], Copyright 2019 The Royal Society of Chemistry.

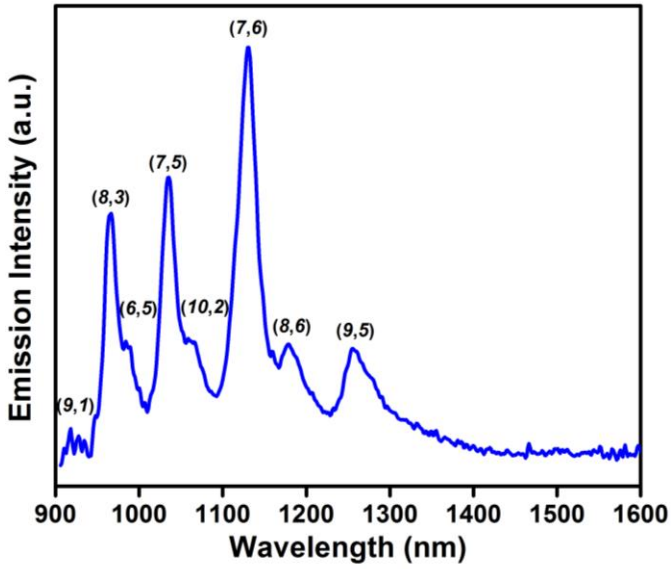

Figure II-4. Normalized fluorescence spectra (excited at 662 nm) of 11.7 ppm s-SWCNTs dispersed in DOC solution. Corresponding major (n,m) types are labeled in the figure. Reprinted with permission from reference [103], Copyright 2019 The Royal Society of Chemistry.

We vacuum filtered m- and s-SWCNT dispersions through a 0.1 μm pore size alumina membrane to make 200 nm thin films with the areal density of 9.6 μg/cm^2. It is also possible to make films using other more efficient techniques such as ultrasonic spraying of CNT dispersions,[93, 107] inkjet printing of CNT dispersions,[108-109] screen printing of CNT dispersions,[110-111] and roll-to-roll printing of CNT dispersions,[112-114] but our findings in this study should not fundamentally change if these other techniques were used. **Figure II-5** shows morphological features of s-SWCNT and m-SWCNT films as observed by SEM. It can be seen that all films have a dense and entangled network of SWCNTs with similar morphology. Surfactant residues are also noticeable especially in the films made using DOC-based dispersions. The images also confirm that the structure of bulk SWCNT film is similar to a CNT network in a composite rather than individual SWCNTs dispersed in a medium.[115-117]

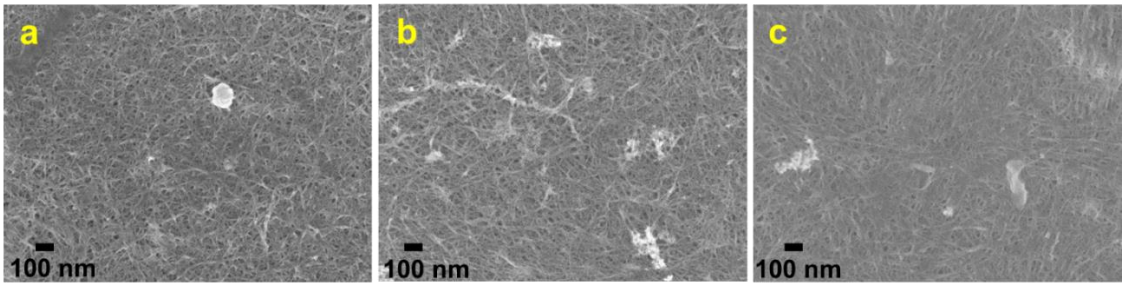

Figure II-5. SEM images of 9.6 μg/cm^2 films of (a) s-SWCNT from DOC-based dispersion, (b) m-SWCNT from DOC-based dispersion, and (c) m-SWCNT from SDS-based dispersion. Reprinted with permission from reference [103], Copyright 2019 The Royal Society of Chemistry.

In order to study RF heating of m- and s-SWCNT films, we used a fringing-field applicator to impose RF fields on the films. Fringing-field RF applicators provide benefits of rapid and non-contact interaction of RF electrical fields with the samples, thus making it also possible to easily apply these applicators to probe RF response of SWCNT-based electronics.[118] **Figure II-6** shows a schematic of the fringing-field applicator. Briefly, two 13-cm long and 6-mm wide parallel copper tracks with a spacing of 2-mm were laid down on a Teflon base. RF power was supplied to the applicator via RF signal generator and a power amplifier. A Forward-Looking Infrared (FLIR) camera was used to monitor the heating response. Note that the length of the applicator is much less than the wavelength of the applied RF field; therefore, making the applicator electrically small (at 70 MHz, the wavelength is approximately 4.0 m). Due to this, the electric field is highly uniform along the copper tracks, and the applicator can be treated as a lumped circuit element instead of a transmission line with standing waves.[118]

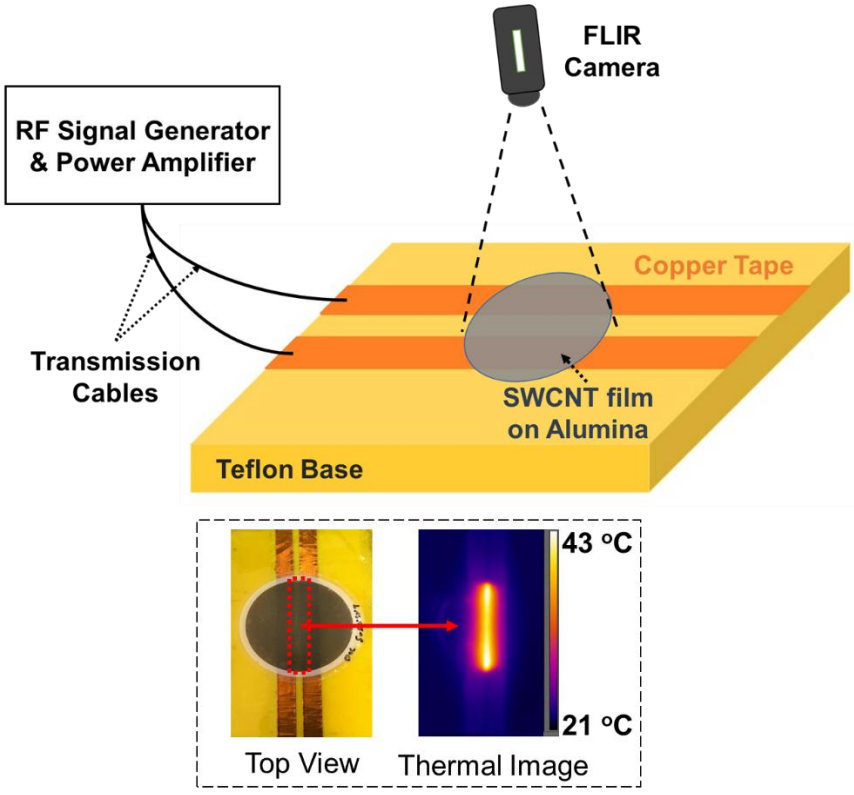

Figure II-6. Schematic of the fringing-field RF applicator for heating SWCNT films. Note that alumina is non-conductive and inert to RF fields. Reprinted with permission from reference [103], Copyright 2019 The Royal Society of Chemistry.

The films were placed on top of the fringing-field applicator, and 1.0 W RF power in the frequency range of 1-200 MHz was applied to determine heating rate as a function of frequency (**Figure II-7**). All films have frequency-dependent heating rates with well-defined resonance in the range of 60-70 MHz. At the frequency of maximum heating rates, the impedance of the RF source (50 Ω) is closely matched to the impedance due to film, applicator, and the connecting cables which leads to efficient coupling between RF energy and films.[57] Note that it is also possible to induce heating in the films by using an impedance matching network and a fixed operating frequency that is within the defined

industrial, scientific, and medicine (ISM) bands.[57, 118] However, our data here shows that the impedance of m- and s-SWCNT films is dependent on the frequency as indicated by different heating rates.

It is seen in **Figure II-7** that the s-SWCNT film has higher heating rates compared to m-SWCNT films. This is primarily due to difference in DC conductivities as shown in **Table II-1**. Since the absorbed RF energy is directly related to the electric field magnitude in the film and the electrical field magnitude is inversely proportional to the electrical conductivity of the film, the s-SWCNT film absorbs more RF energy compared to the m-SWCNT film.[49, 119] The absorbed RF energy induces electric currents in the s-SWCNT film that are more uniformly distributed than those induced in m-SWCNT films. The flow of these currents is opposed in the films due to electrical resistance caused by collisions of electrons with the neighboring atoms or molecules; therefore, resulting in Joule heating [120]. In addition, the m-SWCNT films depict a behavior similar to RF heating of bulk metals. High conductivity metals cannot couple well with RF energy and electric fields attenuate toward the interior of the material.[120-123] Similarly, the RF fields are suppressed inside the high-conductivity m-SWCNT films which lead to induced currents that are non-uniformly distributed, with higher concentrations around the edges; therefore, resulting in overall lower heating rates (**Figure II-8**).

In **Figure II-7**, we also notice that the m-SWCNT film made using DOC-based dispersion has higher heating rates compared to the film made using SDS-based dispersion. This is also correlated with DC conductivity differences as given in **Table II-1**. The difference in conductivities of m-SWCNT films is due to presence of residual

surfactant and s-SWCNT impurities especially in the film made using DOC-based dispersion. The DOC is not easily washed away compared to SDS during vacuum filtration of dispersions because of its high strength of interaction with SWCNTs. This residual DOC creates high resistance barriers at the inter-SWCNT junctions which lowers the conductivity of the film.[124-125] Additionally, the low-conductivity s-SWCNT impurities further contributes to decreasing the overall conductivity of the film. These observations show that it is also possible to use RF heating as a metric for m-SWCNT film purity. The presence of DOC and s-SWCNT impurities decrease the conductivity of the film and this leads to higher RF heating rate, whereas, a relatively pure and high-conductivity m-SWCNT film from SDS-based dispersion show very small RF heating rates.

It is also interesting to note that even though s-SWCNT films heat up more than m-SWCNT films at a given RF power, this is not true when individual SWCNTs are dispersed in a dielectric medium such as a surfactant solution. **Figure II-9** shows that the m-SWCNT dispersion heats up faster compared to the s-SWCNT dispersion. This is because when SWCNTs are dispersed in a dielectric, the overall conductivity, or loss tangent, of the SWCNT dispersion is higher than that of the dielectric alone (which is extremely small compared to SWCNTs). Small amount of high-conductivity m-SWCNTs results in a dispersion with higher loss tangent than that of large amount of low-conductivity s-SWCNTs, which leads to overall higher heating of m-SWCNT dispersion.[120, 126]

It should be noted that the actual conductivity of m- or s-SWCNTs and their films may vary based on differences in synthesis procedures (resulting in varying defect density

or chiral distribution). Nevertheless, our data here shows that regardless of the source, the bulk DC conductivity of the film scales inversely with RF heating rate (**Table II-1**, **Figure II-10**). Of course, at low areal density, this relationship would not hold. We observed a similar behavior for MWCNT-PLA composite films in our earlier work on welding of 3D-printed parts by locally-induced microwave heating.[49] The transmitted, reflected, and dissipated power at the films were measured and correlated with the heating response during 2.45 GHz microwave exposure of various powers. It was determined that higher CNT loadings increased the overall DC conductivity of films,[123, 127] which subsequently decreased the dissipated power at the films and increased the reflected power. Since heating is primarily due to the dissipated power, it can be concluded that the microwave heating rate decreases with increase in conductivity. However, this was not true at lower CNT loadings.[49] Here, we confirm that this non-monotonic relationship also holds for low frequency RF heating of CNT-based materials.

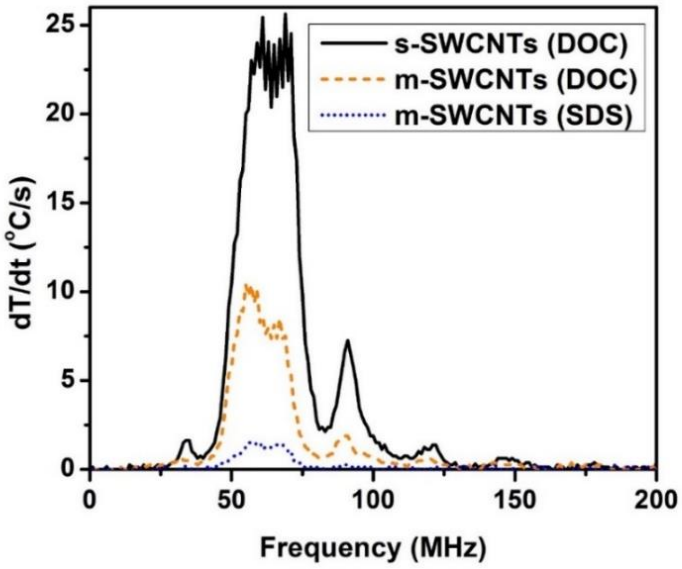

Figure II-7. Heating rate, dT/dt, as a function of radio frequency for s-SWCNT film from DOC-based dispersion and m-SWCNT films from DOC-and SDS-based dispersions. Films were heated using 1.0 W RF power. Reprinted with permission from reference [103], Copyright 2019 The Royal Society of Chemistry.

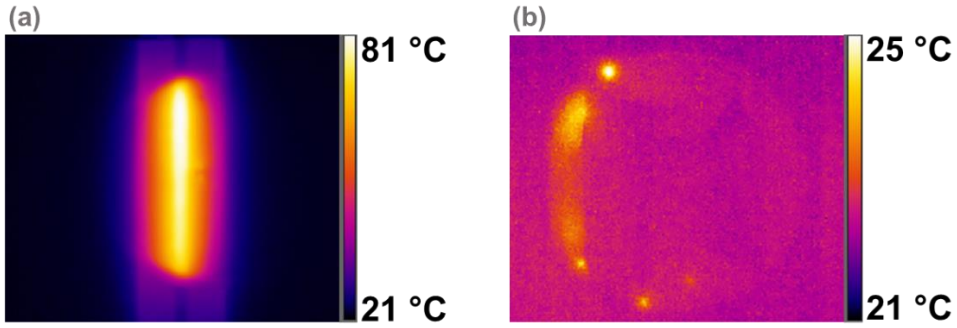

Figure II-8. Thermal images of (a) s-SWCNT film from DOC-based dispersion and (b) m-SWCNT film from SDS-based dispersion heated via 3.2 W RF power at a frequency of 70 MHz. Reprinted with permission from reference [103], Copyright 2019 The Royal Society of Chemistry.

Table II-1. DC conductivity and maximum RF heating rate of m- and s-SWCNT films. Reprinted with permission from reference [103], Copyright 2019 The Royal Society of Chemistry.

	DC Conductivity	Maximum Heating Rate at 1.0 W
Film	**S/m**	**°C/s**
s-SWCNT*	7,800	25.6
m-SWCNT*	22,700	10.4
m-SWCNT**	49,000	1.51

*From DOC-based dispersion, **From SDS-based dispersion.

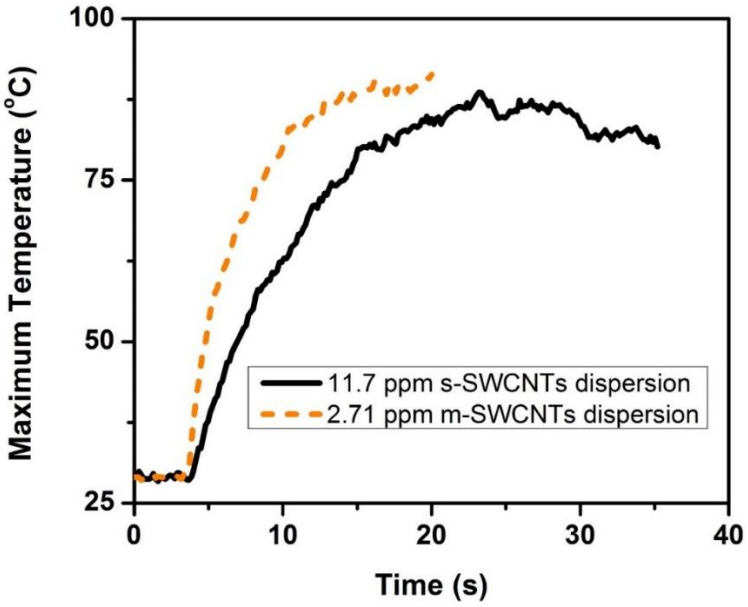

Figure II-9. Maximum temperature as a function of time for a drop of DOC-based dispersions of s- and m-SWCNTs casted on a glass slide and heated via 3.2 W RF power and a resonance frequency of 81 MHz. Reprinted with permission from reference [103], Copyright 2019 The Royal Society of Chemistry.

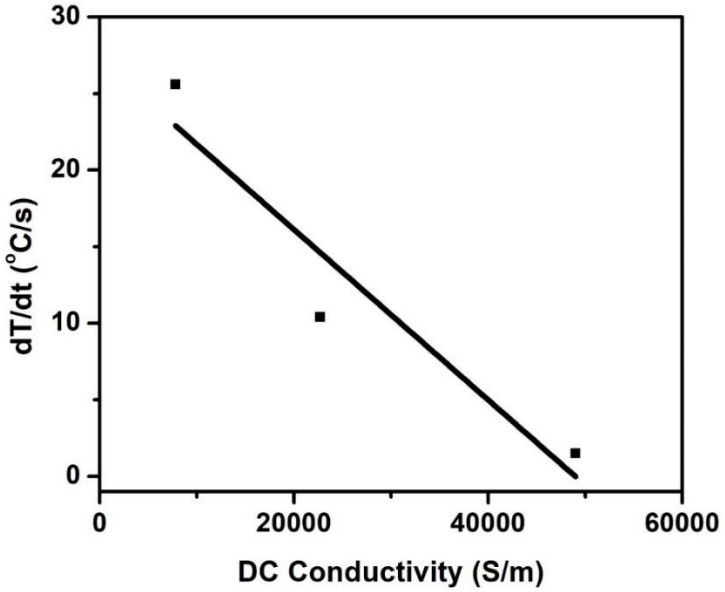

Figure II-10. Heating rate as a function of DC conductivity for m- and s-SWCNT films. Reprinted with permission from reference [103], Copyright 2019 The Royal Society of Chemistry.

Figures II-11a-c show maximum temperature as a function of time for s-SWCNT and m-SWCNT films at different RF powers and a frequency of 70 MHz. The temperature increases with power for all films with s-SWCNT film heating more than 120 °C in less than 5 s at a power of 3.2 W. These tests show that each system reaches thermal equilibrium as the generated heat is balanced by convective losses to the environment. The relationship between the heating rate and power is determined to be directly proportional across all samples as seen in **Figure II-11d**.

The high RF heating rates observed especially for s-SWCNT films is a matter of concern when applied to SWCNT-based electronics. It is because Joule heating has been shown to affect *I-V* characteristics, signal delay, output conductance, and current densities in graphene and s-SWCNT transistors; thus, affecting their overall performance.[128-129]

Additionally, the s-SWCNT films have also attracted tremendous interest as components of RF electronics such as transistors, antennas, amplifiers, and mixers.[101, 130-131] Since these devices utilize radio frequencies in the commercially relevant range of 40 MHz - 25 GHz, we anticipate that RF heating may occur in these devices and heat rates as high as 80 °C/s would decrease their performance and lifetime.[101, 131-133]

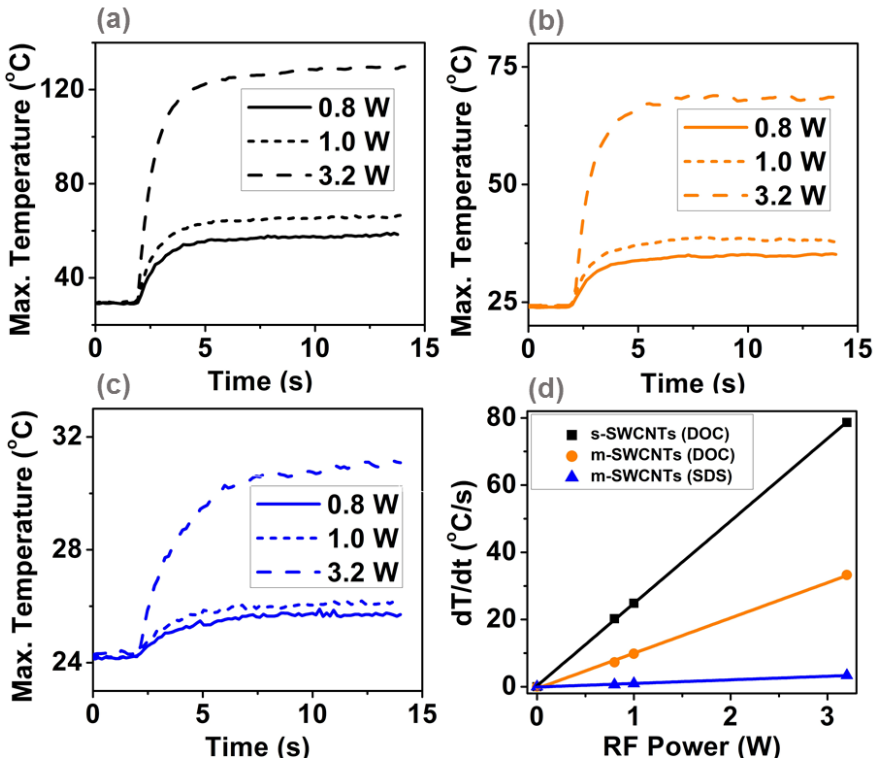

Figure II-11. (a)-(c) Maximum temperature as a function of time for s-SWCNT film from DOC-based dispersion, m-SWCNT film from DOC-based dispersion, and m-SWCNT film from SDS-based dispersion, respectively. (d) Heating rate as a function of RF power for all films. Films were heated using 70 MHz RF fringing-fields at all powers. Reprinted with permission from reference [103], Copyright 2019 The Royal Society of Chemistry.

Conclusions

We investigated the interaction of electric fields at RF frequencies with m- and s-SWCNT films using a fringing-field applicator. We observed Joule heating in all films with m-SWCNT films heating at a much lower rate compared to s-SWCNT films. We also confirmed the complex non-monotonic relationship between RF heating rate and conductivity for CNT-based materials. Our results help in understanding the contributions to RF field interactions of metallic and semiconducting shells in MWCNTs. Additionally, based on our findings, we anticipate that RF heating may occur in SWCNT-based electronic devices and affect their performance and lifetime. Lastly, since impurities in the films affect the conductivity and thus RF heating rate, it is also possible to use RF heating as a metric for film purity.

CHAPTER III

UNIVERSAL PATTERNS OF RADIO-FREQUENCY HEATING IN NANOMATERIAL-LOADED STRUCTURES*

Introduction

Capacitively coupled radio frequency (RF) heating of nanomaterial-loaded structures in the frequency range of 1-200 MHz has shown outstanding potential in material processing applications. This is largely due to the ability to selectively transform electromagnetic energy into heat in a non-contact manner.[57, 134-136] The mechanism for this heating is typically described in the context of Joule heating for macroscale structures composed of nanoscale building blocks. The absorbed RF energy induces electric currents, and the flow of these currents meets electrical resistance caused by collision of electrons with the neighboring atoms or molecules, which results in heating. This happens over a network of connected conductive nanofillers.[103, 137]

A wide range of nanomaterials and their polymer composites has recently been shown to rapidly heat using RF fields. These include multi-walled and single-walled carbon nanotubes (CNTs)[57, 103], carbon black,[138] graphene,[55] carbon nanofibers (CNFs),[53] silicon carbide,[135] and MXenes.[139] RF heating rates as high as 100 °C/s at low RF powers (<10 W) for these materials have allowed for novel material processing methods such as

---

* Reprinted with permission from "Universal patterns of radio-frequency heating in nanomaterial-loaded structures" by Muhammad Anas; Mazin M. Mustafa; Aniruddh Vashisth; Eftihia Barnes; Mohammad A. Saed; Lee C. Moores; Micah J. Green. 2021, *Applied Materials Today*, 23, 101044, Copyright 2021 Elsevier Ltd.
Mazin M. Mustafa is acknowledged for simulation work in this chapter.

continuous CNF/epoxy and CNT/epoxy pre-preg manufacturing,[53] high-throughput CNT circuit screening,[138] and polymer surface welding.[55-56]

However, these RF susceptors have shown a number of surprising features, including frequency-dependent RF heating and a non-monotonic relationship between nanofiller loading and heating behavior. For example, we previously observed that the RF heating of composite films such as CNT-polylactide (CNT-PLA)[57] and MXene-polyvinyl alcohol ($Ti_3C_2T_x$-PVA)[139] increased up to a certain filler loading, but then decreased with further increase in loading. Similarly, we also determined that the highly conductive metallic single-walled carbon nanotubes (m-SWCNTs) showed significantly smaller RF heating rates compared to less conductive semiconducting single-walled carbon nanotubes (s-SWCNTs).[103] These findings confirm that electrical conductivity is required for RF heating, but it is not well understood how RF heating rates vary with conductivity and if the pattern is generalizable for all types of RF susceptor-loaded structures and predictable via simulation.

Here we use experiments and simulations to describe a unifying RF heating perspective that applies to a wide range of nanomaterial-based systems. We find that, for a given applicator, nanomaterial loadings affect bulk dielectric properties, which is correlated with heating. We show that the highest heating rate observed across all frequencies is non-monotonically related with the in-plane electrical conductivity. This relationship has a distinct maximum at the same in-plane electrical conductivity for all nanomaterial films studied. We also find that the point of maximum heating rate is closely associated with the percolation threshold for both thin films and thick composites.

Results and Discussion

Figure III-1 shows the schematic of the fringing-field applicator used for RF heating of nanomaterial-loaded structures. The applicator with the sample behaves like an RLC resonance circuit. The two copper traces electrically behave as inductors (L). The small air gap between the two traces is a capacitor (C). The sample adds a shunt resistance (R) and changes the gap capacitance. The frequency associated with maximum RF absorption is dictated by the dimensions of the applicator. The dimensions were selected to obtain RF absorption in the range of 1-250 MHz. The RF electric fields are concentrated in the capacitor air-gap and couple with the conductive sample.[140]

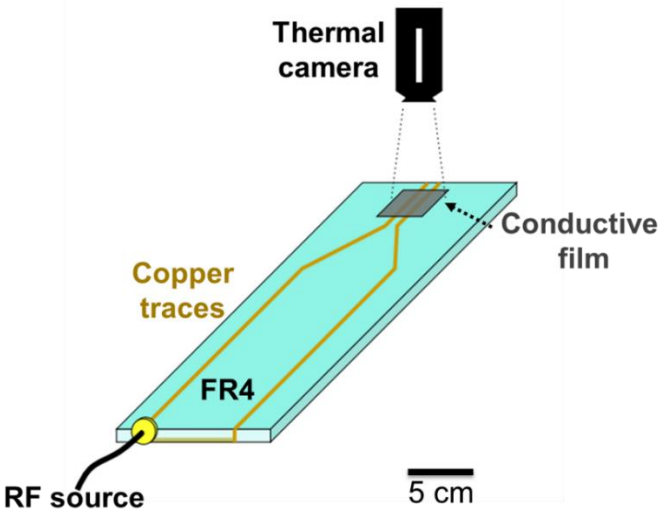

Figure III-1. Schematic of the RF fringing-field applicator used for heating of conductive films in the frequency range of 1-250 MHz. Reprinted with permission from reference [141], Copyright 2021 Elsevier Ltd.

Figure III-2 shows the electric field intensity at 130 MHz for a sample with surface conductivity of 0.46 mS. The capacitive coupling of fields is visible in the side view. This coupling induces surface currents which lead to electromagnetic losses and

thus heating. Note that this applicator is ideal for thin structures as the electric field strength decays exponentially in the vertical direction.[55] The concentration of the electric fields in the capacitor can be controlled by changing the applied RF power or the size of the gap between the traces.

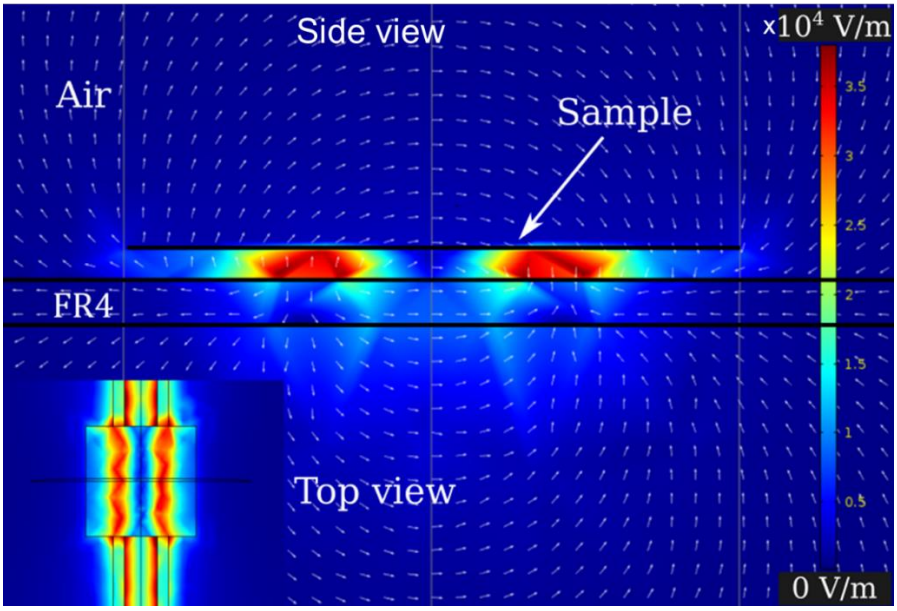

Figure III-2. Electric field distribution at 130 MHz for a sample of surface conductivity 0.46 mS. Reprinted with permission from reference [141], Copyright 2021 Elsevier Ltd.

We used airbrush spraying of MWCNT-COOH ink to make conductive films and varied areal density of CNTs to control the surface conductivity. Functionalized CNTs were used due to their dispersibility in water which prevents use of other additives such as polymeric binders. **Figure III-3** shows DC surface conductivity (inverse of sheet resistance) as a function of areal density for CNT films. A percolation-type behavior is observed where the conductivity suddenly increases with a small change in areal density

indicating the formation of a conductive network. The applicator was used to measure heating rates as a function of frequency for the conductive films.

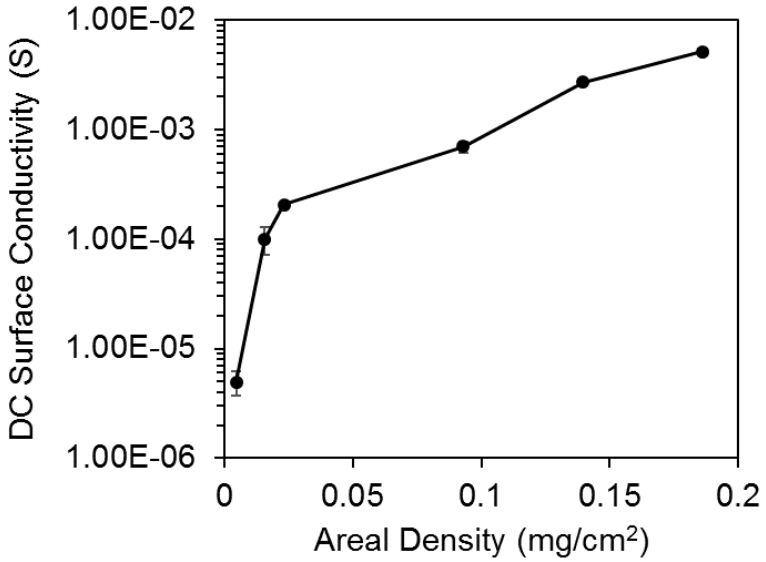

Figure III-3. DC surface conductivity as a function of areal density for CNT films. Reprinted with permission from reference [141], Copyright 2021 Elsevier Ltd.

Figure III-4a shows the frequency-dependent heating response for a MWCNT film with DC surface (in-plane) conductivity of 2.7 mS. The resonance indicated by the maximum heating rate of 19 °C/s is clearly noticeable at around 130 MHz. This corresponds to the maximum absorption of RF fields by the sample. Other prominent peaks are observed at 146 MHz and 110 MHz with heating rates of 10 °C/s and 6 °C/s, respectively. Heating is higher in the frequency range of 100-160 MHz but peaks with smaller heating rates are also observed at 85 MHz and 176 MHz. Multiple peaks are observed due to the non-uniformities in the sample. Since heating rates are directly proportional to the RF power, heating rate can be increased at frequencies which show

small heating rates at low powers. This interesting feature of frequency-dependent heating has attracted interest for applications such as nanomaterial-based actuators.[142] Note that the heating rate was calculated using the maximum temperature observed in the heating area at each instant in time. (**Figure III-5** confirms that similar heating rates are obtained if the average temperature over the heating area is used for the calculation instead of maximum temperature over the heating area.)

We used COMSOL Multiphysics finite element software to simulate the RF absorption phenomenon as well as RF-induced heating. **Figure III-4b** shows the simulated heating rate and the reflection coefficient ($|S_{11}|$) as a function of frequency for a conductive film. The heating rate was calculated using the initial slope of the temperature versus time relationship for each frequency. The resonance is seen at a frequency of 145 MHz, and a minimum $|S_{11}|$ parameter at the same frequency confirms that the reflection of RF fields is minimized at that frequency; this corresponds to maximum RF absorption resulting in maximum heating rate. The simulated RF heating behavior follows a bell curve-like distribution of heating rates. Heating rate increases with the frequency up to the point where the maximum heating rate of 26 °C/s is seen at around the average value of frequency in the range. This frequency value is closely associated with the design frequency of the applicator. The corresponding relationship between $|S_{11}|$ and frequency indicates perfectly coupled electromagnetic and heat transfer phenomena. The overall pattern is universal for all materials because it depends on the in-plane electrical conductivity of the sample; however, heating rates may differ due to differences in heat transfer properties and the level of impedance mismatch ($|S_{11}|$). Note that the difference

in the resonant frequencies for experiment and simulation is due to the non-idealities in the fabricated applicator such as electrical connections.[143] Moreover, simulated heat rates are higher than those observed in the experiments because of the ideal nature of the simulation where no power losses due to electrical components are present. Heat transfer assumptions used in the simulation are other possible reasons for difference in heating rates.

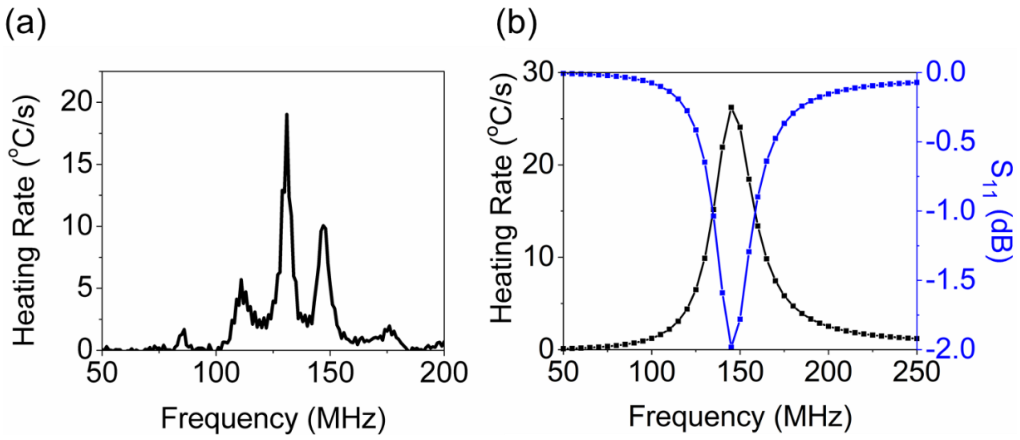

Figure III-4. (a) Experimental heating rate at 2.0 W as a function of frequency for MWCNT film with DC surface conductivity of 2.7 mS. (b) Simulated heating rate at 2.0 W and $|S_{11}|$ as a function of frequency for surface conductivity of 2.7 mS. Reprinted with permission from reference [141], Copyright 2021 Elsevier Ltd.

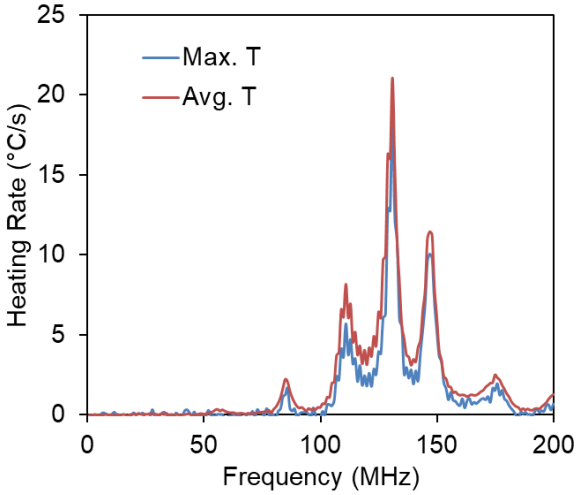

Figure III-5. Initial heating rate at 2.0 W as a function of frequency for MWCNT film calculated using average temperature and the maximum temperature over the heating area. Sample has DC surface conductivity of 2.7 mS. Reprinted with permission from reference [141], Copyright 2021 Elsevier Ltd.

We also determined heating rate as a function of surface conductivity for a specific frequency. **Figure III-6** shows experimental and simulated relationships between surface conductivity and heating rate at a frequency of 130 MHz and a power of 2.0 W. Heating rate is non-monotonically related with the surface conductivity for nanomaterial thin films. This relationship is universal for all materials because surface conductivity primarily determines the RF field absorption in the sample. It is noticed in both experiments and simulation that there is an optimum conductivity associated with maximum heating. In **Figure III-6a**, maximum heating rate of around 20 °C/s is observed in the DC surface conductivity range of 0.20 - 0.70 mS. In **Figure III-6b**, maximum heating rate of 26 °C/s is observed at the AC surface conductivity of 0.46 mS which is in close agreement with the data in **Figure III-6a**. Note that for experiments the DC surface conductivity of the samples were measured instead of the AC due to the challenges associated with in-plane

AC measurements of thin films. These two conductivity values are correlated with one another, which allows us to observe a similar trend. In the region of conductivities lower than the optimum value, heat generation increases with the surface conductivity according to equation 1. In the region of conductivities greater than the optimum value, electric field magnitude decreases in the film due to reflection of RF fields by the conductive network which leads to smaller heating rates.[103] The maximum heating is assumed to be close to the percolation threshold which is the onset of the conductive network and the dielectric properties (AC conductivity and dielectric constant) increase significantly.[144-145]

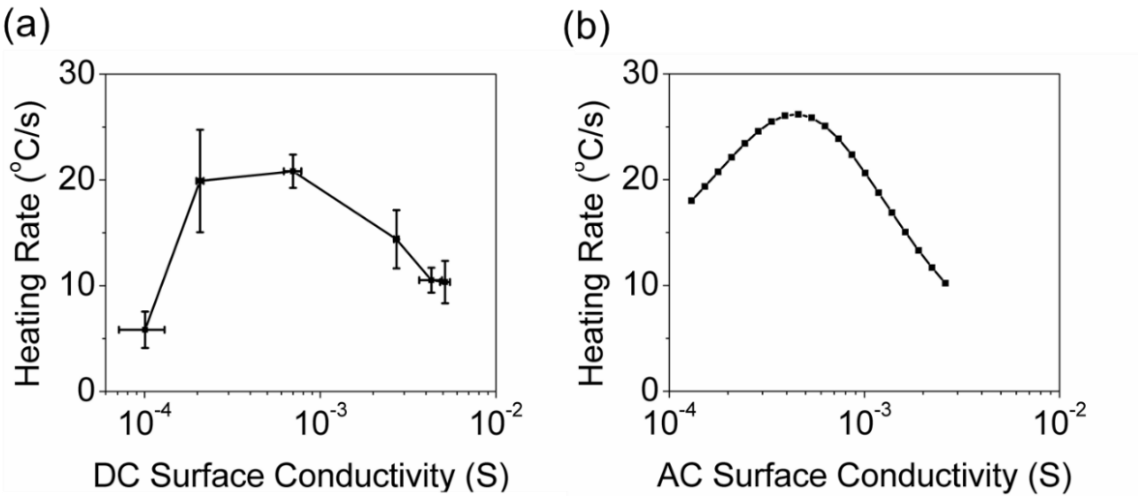

Figure III-6. (a) Experimental and (b) Simulated heating rate as a function of surface conductivity at 130 MHz and 2 W for MWCNT films on PET. Reprinted with permission from reference [141], Copyright 2021 Elsevier Ltd.

For a clear universal pattern of RF heating, it is desired to obtain a full map of heating rate as a function of conductivity and frequency. However, that is experimentally and computationally challenging. Since $|S_{11}|$ correlates with the heating rate as seen in

Figure III-4b, a simple and faster approach is to compute $|S_{11}|$ parameter as a function of conductivity and frequency.

Figure III-7 shows the full map of the $|S_{11}|$ parameter with surface conductivity and frequency using HFSS simulations. (**Figure III-8** confirms that both HFSS and COMSOL compute similar $|S_{11}|$ parameters.) **Figure III-9** shows the $|S_{11}|$ parameter for the applicator without sample and the applicator with the sample of surface conductivity 0.48 mS. The change in reflection coefficient in the presence of the sample indicates the RF field absorption by the sample. For a given applicator, this pattern is universal and is applicable to many materials. For the applicator used in this study, there is an optimum frequency (152 MHz) and surface conductivity (0.32 mS) associated with minimum $|S_{11}|$ (-8.7 dB). $|S_{11}|$ is non-monotonically related with both the surface conductivity and the frequency. For a given frequency, as the conductivity is increased, RF energy absorption increases up to the optimum conductivity. As the conductivity is increased further, electric fields cannot penetrate the material, and the percentage of RF fields absorbed decreases, thus leading to more reflections and higher $|S_{11}|$.[146] As the surface conductivity is varied, a small shift in resonant frequencies is also observed.

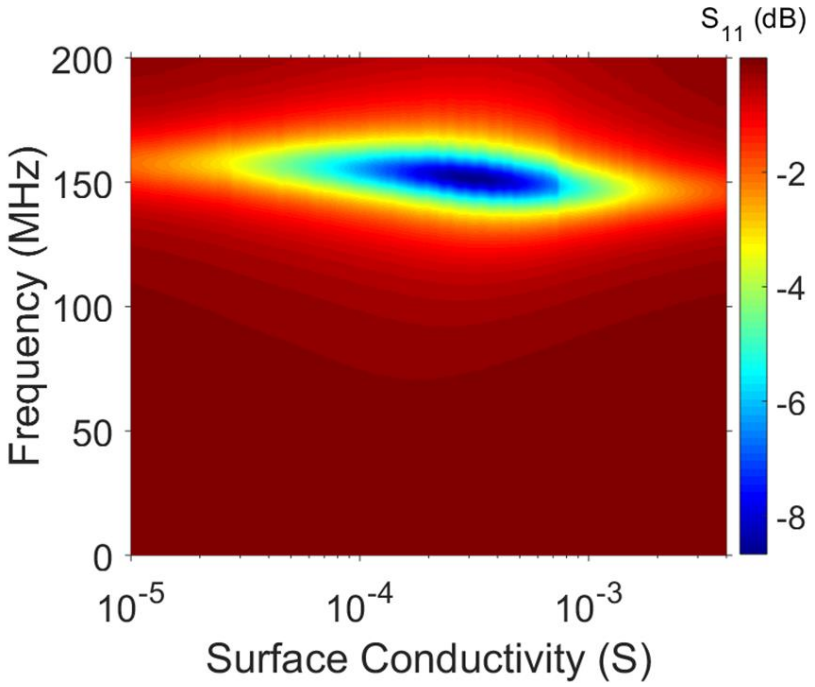

Figure III-7. Simulated |S_{11}| parameter as a function of frequency and surface conductivity. Reprinted with permission from reference [141], Copyright 2021 Elsevier Ltd.

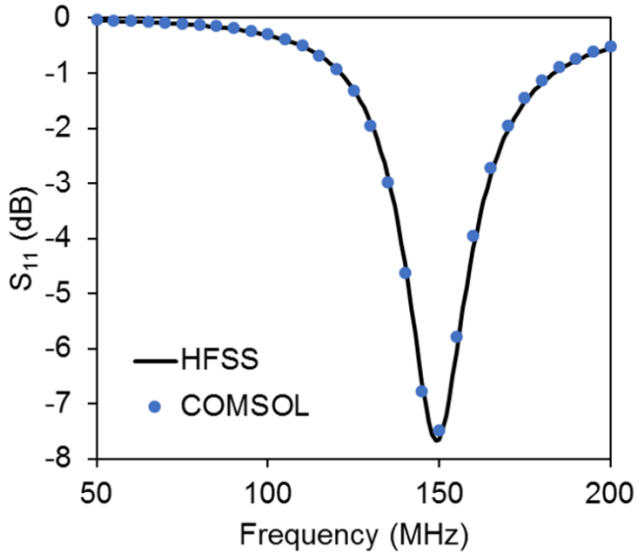

Figure III-8. Comparison of |S_{11}| parameter obtained from COMSOL and HFSS for a sample with surface conductivity of 0.52 mS. Reprinted with permission from reference [141], Copyright 2021 Elsevier Ltd.

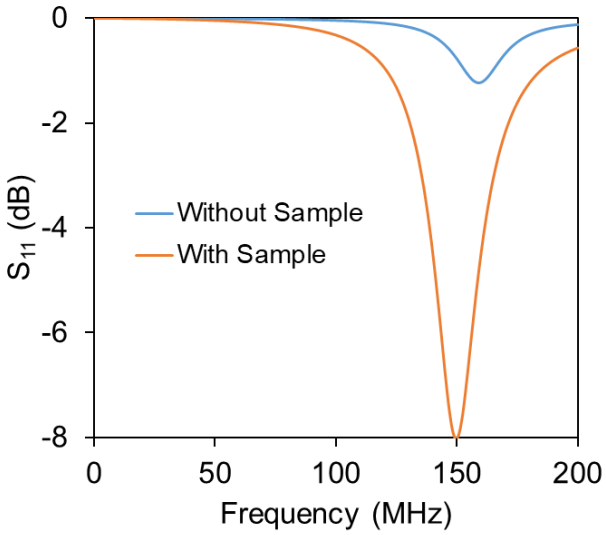

Figure III-9. $|S_{11}|$ as a function of frequency with sample (0.48 mS) and without sample. Reprinted with permission from reference [141], Copyright 2021 Elsevier Ltd.

The universal pattern fits other types of nanofillers as well such as laser-induced graphene (LIG) and carbon nanofiber (CNF) as shown in **Figure III-10**. **Figures III-11** and **III-12** provide DC surface conductivity as a function of laser points per inch (PPI) and CNF loading, respectively.

Note that the maximum heating rate over the frequency range of 1-200 MHz was used. A distinguished maximum is seen at approximately the same DC surface conductivity (in the range of 0.1-0.2 mS) for all materials. LIG@Kapton films show significantly higher heating rates of 65 °C/s at 2.0 W compared to around 25 °C/s for MWCNT and CNF-PA films at the same power primarily due to differences in morphology as seen in the SEM images in **Figure III-13**.

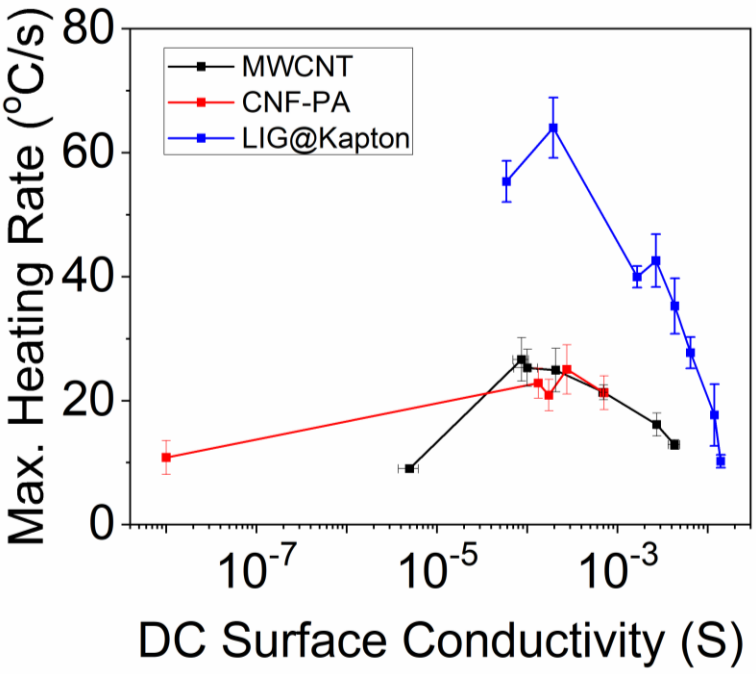

Figure III-10. Maximum heating rate over the full frequency range as a function of DC surface conductivity for MWCNT films, CNF-PA composite films, and LIG@Kapton films. All samples were heated via 2.0 W RF fringing fields. Reprinted with permission from reference [141], Copyright 2021 Elsevier Ltd.

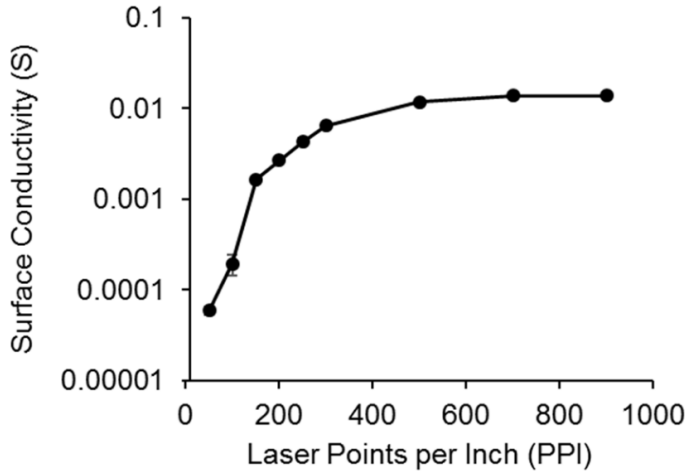

Figure III-11. DC Surface conductivity of LIG@Kapton films as a function of laser PPI at 15% laser power and 200 mm/s laser speed. Reprinted with permission from reference [141], Copyright 2021 Elsevier Ltd.

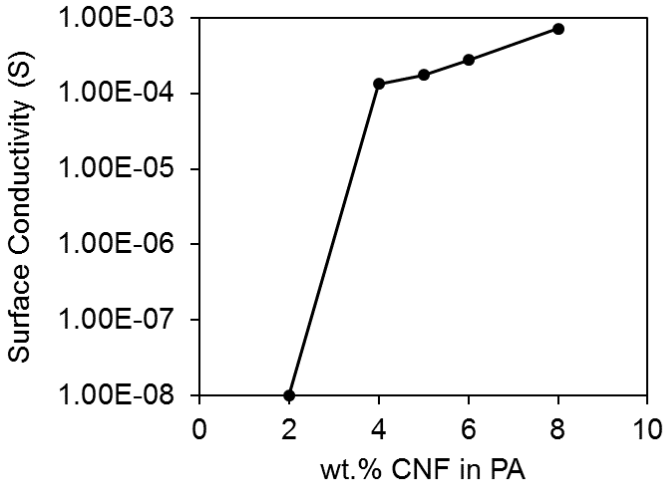

Figure III-12. DC surface conductivity as a function of carbon nanofiber (CNF) loading in polyamide (PA) films (50 µm film thickness). Reprinted with permission from reference [141], Copyright 2021 Elsevier Ltd.

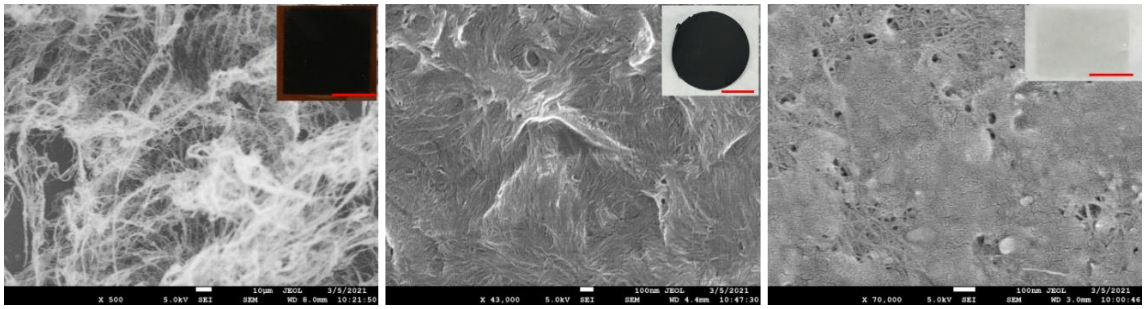

Figure III-13. Scanning electron microscope (SEM) image of LIG@Kapton (left, scale bar: 10 µm), CNF-PA (middle, scale bar: 100 nm) and MWCNT on PET (right, scale bar: 100 nm) films of surface conductivity 0.2 mS. Inset shows the digital images of the films (scale bar is 1 cm). Reprinted with permission from reference [141], Copyright 2021 Elsevier Ltd.

In addition to nanomaterial-loaded thin (micro-nanometer scale) films, the universal pattern of RF heating is also true for thick (centi-millimeter scale) nanomaterial-loaded structures. **Figure III-14** confirms the non-monotonic relationship between heating rate and conductivity for carbon nanostructures-polycarbonate (CNS-PC) composites provided by Cabot Corporation. Maximum heating rate of 0.62 °C/s is

obtained at the DC conductivity of 0.20 S/m which corresponds to the composite with 0.50 wt.% filler loading as shown in **Figure III-15.** Note that the heating rates are lower compared to that of thin films due to difference in the sample thickness.

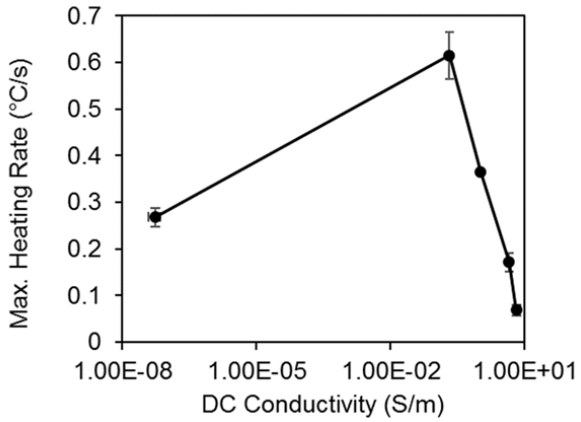

Figure III-14. Maximum initial heating rate over full frequency range as a function of DC conductivity for CNS-PC composites. All samples were heated via 10 W RF fringing fields (4 mm sample thickness). Reprinted with permission from reference [141], Copyright 2021 Elsevier Ltd.

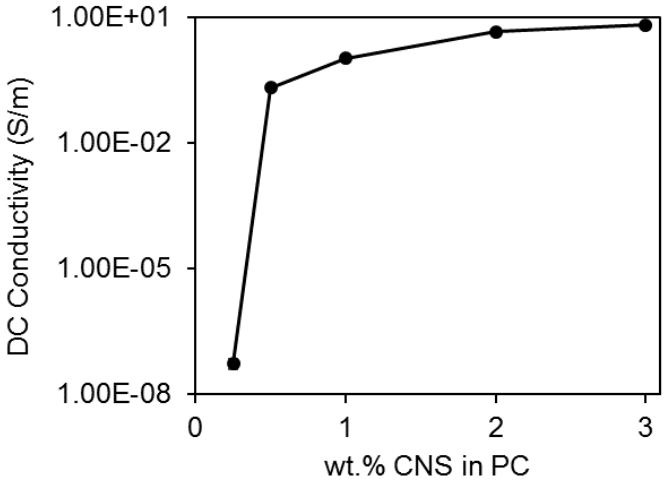

Figure III-15. DC conductivity as a function of carbon nanostructure (CNS) loading in polycarbonate (PC) composites (4 mm sample thickness). Reprinted with permission from reference [141], Copyright 2021 Elsevier Ltd.

Conclusions

We used a fringing-field applicator for RF heating of nanomaterial-loaded structures as a function of frequency and conductivity. We showed using experiments and simulations that the RF heating rates are non-monotonically related with the conductivity of the structure and that this pattern is universal for many different nanomaterials. We found that for thin films, the maximum RF heating response is observed at the same in-plane DC surface conductivity regardless of the nanomaterial. We also determined that this maximum is closely associated with the percolation threshold in the nanomaterial structures. These findings show that RF heating can be optimized by tuning the bulk dielectric properties of the nanomaterial-loaded structures. This would be useful for improving the efficiency of the RF-based material processing techniques.

CHAPTER IV

HIGH THROUGHPUT SCREENING OF PRINTED CARBON NANOTUBE CIRCUITS USING RADIO FREQUENCY HEATING[*]

Introduction

Carbon nanotubes (CNTs) have attracted tremendous interest for high-performance electronics due to their high electrical conductivity, mechanical integrity, and stability.[71-72, 147] The two most common routes to integrate CNTs into electronic devices are solution-based printing and direct growth of individual CNTs on a substrate.[66, 91] Compared to using individual CNTs in a device, solution-based printing of CNTs is a simple approach that is also cost effective and easily scalable.[91, 148] Printed CNT structures can be readily used to make solar cells,[149-150] sensors,[148, 151] antennas,[109] thin-film transistors,[108, 152] and flexible electrodes.[153-154]

Various printing techniques such as inkjet printing,[108-109] screen printing,[110, 155] flexographic printing,[156] and roll-to-roll printing[112-113] have been developed to deposit CNTs onto a substrate for rapid production of electronic devices. For example, Ha *et al.*[157] used inkjet printing of CNT inks to fabricate an array of high-performance digital circuits on a flexible polyimide substrate. Cao *et al.*[110] screen-printed 12 x 10 array of CNT-based circuits on a flexible polyethylene terephthalate (PET) sheet. Lee *et al.*[112] demonstrated

[*] Reprinted with permission from "High-throughput screening of printed carbon nanotube circuits using radio frequency heating" by Victoria K. Hicks; Muhammad Anas; Erin B. Porter; Micah J. Green, 2019. *Carbon*, 152, 444-450, Copyright 2019 Elsevier Ltd.
Victoria K. Hicks is acknowledged for equal contribution in this chapter.

roll-to-roll printing of 20 x 20 CNT circuits on a PET sheet proving fast production of cutting-edge electronics. All these studies show that it is now possible to easily and quickly fabricate CNT-based devices. However, it is also important to develop high-throughput protocols to characterize the functionality of CNT circuits and their print quality.

Prior methods for quality assurance of CNT components in electronics are limited to resistance measurements using a two-point probe or a four-point probe.[154, 158-159] These methods are time-consuming and provide only a scalar measure of CNT prints that may have spatial variations in morphology and areal density of active material. Therefore, it is important to have an efficient method that can rapidly differentiate between the passable and faulty CNT prints for applications in circuits.

CNTs have been known to interact with electromagnetic radiation and rapidly heat up in response to applied fields.[46, 160-161] This phenomenon has been utilized in the past by our group to detect CNTs in biological samples,[162] rapidly cure thermosets by using CNTs as nanofillers,[163] and weld 3D-printed parts with localized heating of CNTs at the filament interface. Recently, we have shown that CNTs also heat up in response to electric fields at low RF frequencies (1-200 MHz).[57] We demonstrated different applicator configurations such as direct contact, parallel plate, and fringing-field for heating the CNT-polymer composites. We determined that the heating rate of a sample is dependent on the frequency, and the maximum heating rate is indicative of closely matched impedances of source and the load. We also tested a new technique for rapidly curing thermoset adhesives in metal-metal bonding which has applications to automotive and

aerospace industries.[57] Now we apply this RF heating phenomenon to printed multi-walled carbon nanotube (MWCNT)-based circuits. Note that MWCNTs are easier to mass produce and have lower cost compared to their single-walled analogs; therefore, making them useful for large scale production of circuits. However, it is also possible to print SWCNTs to make circuits[164-166] and we have recently shown that SWCNTs also heat up under radio-frequency fringing-fields. This makes it possible to apply RF heating phenomenon to printed SWCNT-based circuits as well.

Here we demonstrate a method for reliable, high-throughput quality screening of MWCNT-based circuits by heating in a low frequency RF field. The fields can penetrate dielectric substrates such as the PET and remotely heat MWCNT structures. Thermal camera allows for visual inspection of films based on heat response. Both the RF heating and the thermal imaging are non-contact and thus high-throughput; samples can be characterized as quickly as they are made. This could replace time-consuming conductance measurements for quality screening. This can also potentially be extended to other carbon nanomaterial-based inks, such as graphene.

Results and Discussion

In order for a CNT circuit to be functional, it must have a uniform nanomaterial density and a sufficiently high conductance. Currently, each circuit must be individually tested for functionality in an imprecise and lengthy quality-check process. The goal of this work is to demonstrate a high-throughput technique for screening CNT prints, which is fast and more reliable than the current method.

Specifically, the quality metric for CNT circuits is the 2-point resistance. The resistance across the circuit is determined using a voltmeter or a 2-point probe. If the circuit is found to have an overall resistance above 25 kΩ, it is considered to be faulty according to the manufacturer. This traditional metric is time-intensive to test and flawed as a quality analysis tool. It can take up to 10 minutes to test a single sheet of 377 printed CNT circuits. Additionally, circuits with small gaps in the center can still show sufficiently low overall resistance, despite the defect in the print.

We utilized the unique thermal response of CNTs to low frequency RF fields in order to develop a high-throughput screening technique. The setup is demonstrated in **Figure IV-1.** Briefly, a fringing-field capacitor was used to induce non-contact heating of the circuits. The capacitor was fabricated onto a large Teflon board to have a uniform surface for the sheet of circuits to travel along. The edges of the board were lined with cardboard to create runners which align the sheet during testing. The sheet was placed in between the runners on the board and a piece of tape was used to connect the sheet to a linear stage. The stage was used to pull the sheet across the capacitor at a constant rate of 5.6 mm/s so that each circuit was exposed to the field for 1.0 second. The RF generator

was set to a power of 10 W and an operating frequency of 60 MHz. The RF was activated immediately before the sheet passed over the capacitor. The thermal camera was placed directly above the capacitor so that the thermal response of each circuit could be recorded as it passed over the capacitor. Scanning one sheet of 377 circuits took approximately 30 seconds.

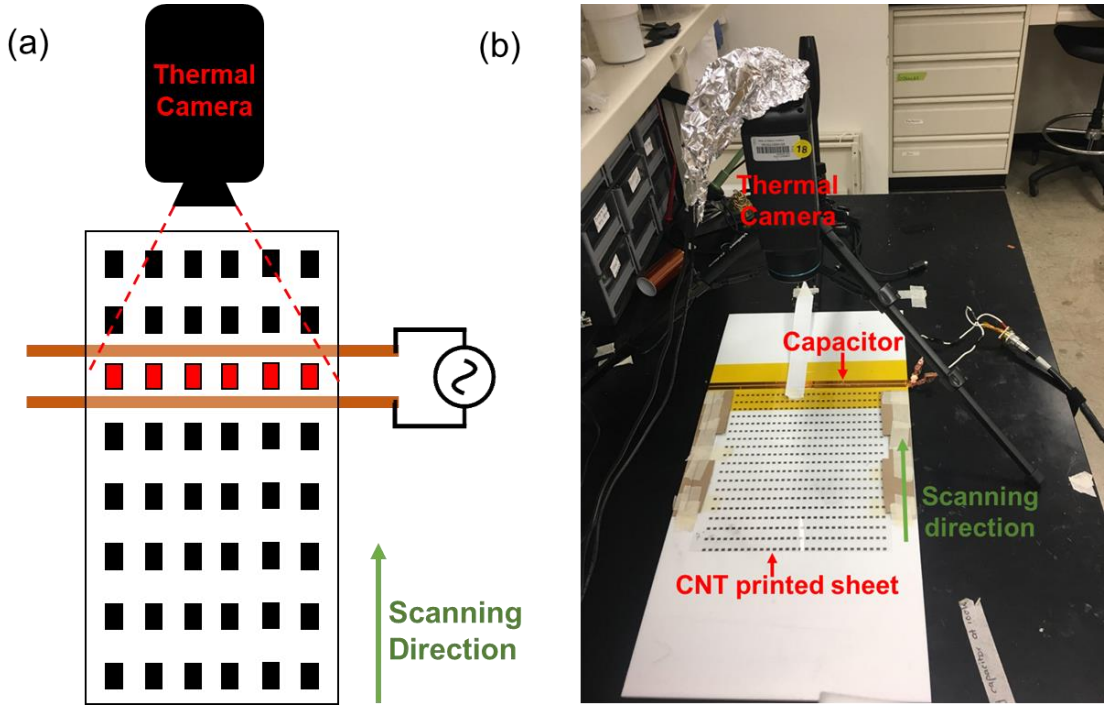

Figure IV-1. (a) Schematic and (b) original picture of the setup to test the quality of CNT prints using RF heating. Sheets of CNT prints are scanned over a fringing-field RF applicator and a vertically mounted infrared camera is used to monitor the heating response. Reprinted with permission from reference [138], Copyright 2019 Elsevier Ltd.

The faulty CNT print is a sheet of CNT circuits where some of the circuits have a decreased areal density, varying (non-uniform) areal density, a blank spot, or a stripe of missing active material that will cause loss of functionality. **Figure IV-2a** shows an example of a faulty CNT print and its thermal response. The thermal response of each

circuit varies according to its areal density. The circuits that have large gaps or very low areal density of active material appear in the thermal image with a much lower temperature rise. Although many of these faulty circuits can be easily identified by visually inspecting the originally printed sheet, several circuits have non-uniformities that are not visually clear but are easily noticeable in the RF heating response.

A CNT print is considered "passable" when all of the circuits on the sheet display a uniform density of active material and each circuit has a sufficiently high conductivity. **Figure IV-2b** shows a passable CNT print and its corresponding RF heating profile. For every circuit on the sheet, the capacitor caused a uniform thermal reaction. In the thermal image, each circuit appears the same, indicating uniformity in the printed sheet. The temperature change of about 4°C is seen for each circuit. The maximum temperature experienced by the sample is too low to cause degradation, therefore the circuits remain functional after the testing process.

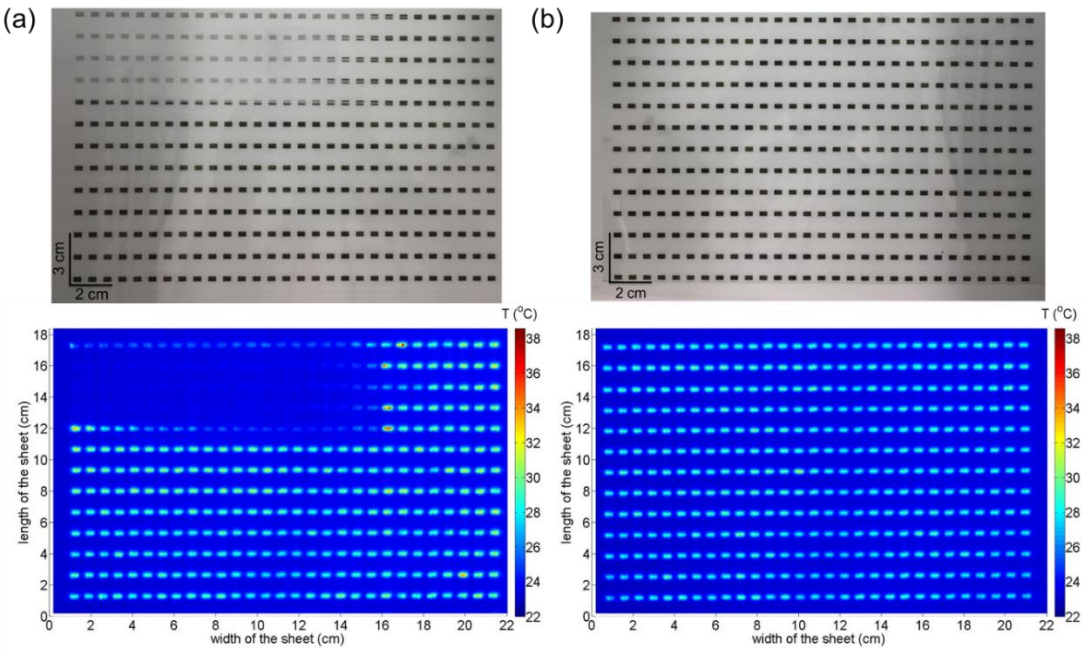

Figure IV-2. (a) Faulty and (b) passable CNT prints and their corresponding RF heating profiles after scanning at the rate of 5.6 mm/s through a 60 MHz, 10 W fringing-field. Reprinted with permission from reference [138], Copyright 2019 Elsevier Ltd.

The original faulty CNT print in **Figure IV-3a** was also tested by the conventional resistance measurement quality-check technique. A voltmeter was used to measure the resistance across each circuit. The probes were placed at opposite corners of each circuit and the DC resistance was measured. The resistance of each circuit was then used to create a conductance map in the MATLAB® as given in **Figure IV-3b**. Circuits with resistance below 25 kΩ (conductance above 0.04 $k\Omega^{-1}$) are considered functional by the conventional method. (Note that the RF heating response is included again in **Figure IV-3c**).

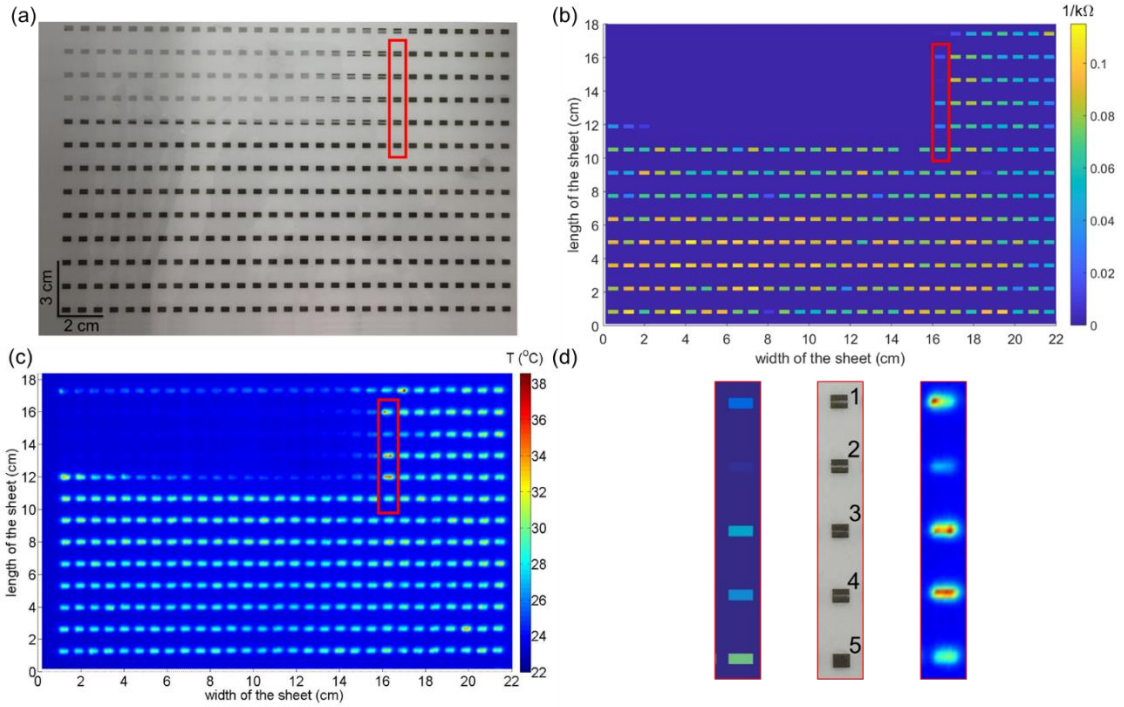

Figure IV-3. (a) Original faulty CNT print, (b) 2.0-point probe conductance map, and (c) RF heating profile. (d) A closer image of selected circuits (#1-5). Note the lack of thermal response from the poor-quality circuits within the array. Reprinted with permission from reference [138], Copyright 2019 Elsevier Ltd.

Most of the faulty circuits were identified by both the traditional resistance-based metric and the RF heating analysis. However, the traditional metric does "pass" several circuits which are faulty. **Figure IV-3d** shows that several circuits have stripes where the CNTs are absent. These circuits would show decreased functionality in sensing applications and should be failed by a reliable quality metric. The thermal images of these circuits show non-uniformities, clearly indicating that the circuits are faulty. However, the traditional metric failed to identify some of the circuits, such as circuit #3 (0.043 $k\Omega^{-1}$), because CNTs run along the border of these circuits, creating a closed loop with a low resistance (several examples are illustrated in **Figure IV-4**). The flaw was identified by

the scanning method because the break in the network changed the heating effects within the circuit and created a distinguishable change in the heating profile; in these cases, scalar metrics are prone to misidentify faulty circuits.

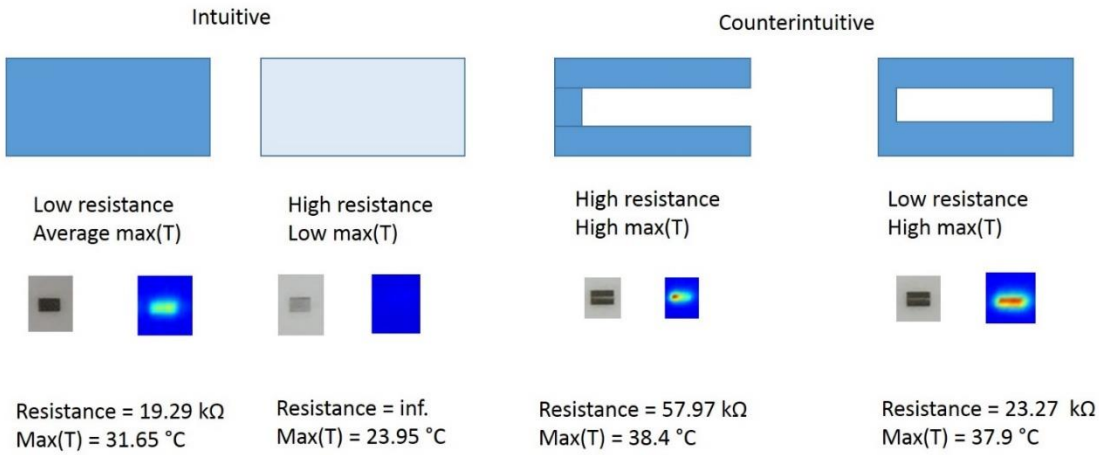

Figure IV-4. These images show examples of how scalar metrics, such as RF heating temperature and resistance, can fail to unequivocally detect faulty circuits. Reprinted with permission from reference [138], Copyright 2019 Elsevier Ltd.

Note that it is also possible to use RF heating measurements as a quantitative metric for determining circuit quality by calculating the average temperature and variance of the temperatures over the full area of each individual circuit. It is seen in **Figure IV-5** that faulty circuits such as # 1, 3, and 4 have higher average temperatures compared to that of passable circuits (#5-8) and also show large variances which indicate non-uniformities in heating. Faulty circuit # 2 has lower average temperature due to insufficient CNT coverage. On the other hand, all passable circuits (#5-8) have similar average temperatures at a specific power with small variances which indicate uniform heating. Differences in variance of passable circuits may be used to indicate different quality grades of the circuits.

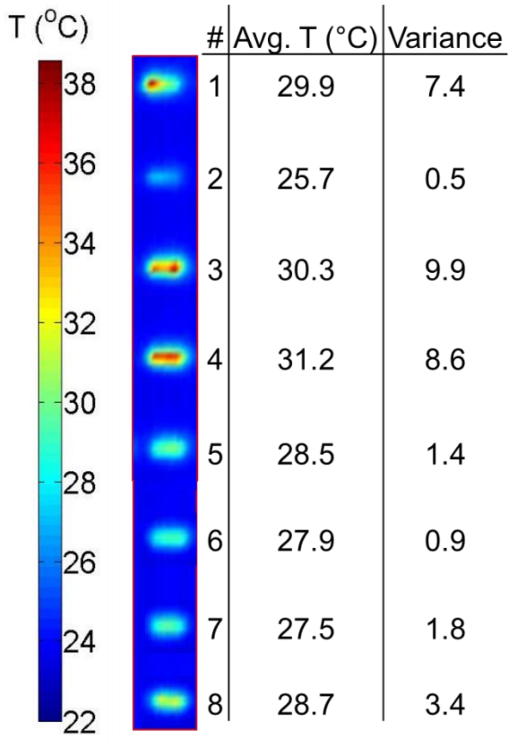

Figure IV-5. Examples of how average RF heating temperatures and the variance of the temperatures over the full area of individual circuit can be used as a quantitative metric of circuit quality. Reprinted with permission from reference [138], Copyright 2019 Elsevier Ltd.

The parameters of the fringing-field can also affect the thermal response of the circuits. The power of the field can determine the heat generated by each circuit. **Figure IV-6** shows a single row of passable CNT circuits. These circuits were placed on the fringing-field capacitor, and the RF was activated for 10 seconds. The thermal camera was placed directly above the capacitors, so the image could be captured as shown. At 10 seconds, the temperature along the green line was measured. The resulting graph shows the temperature of the circuits on that line. This test was repeated at RF powers of 2.5, 5.0, and 10 W. The graph shows that the temperature change of each circuit can be increased

by increasing the power of the field. This means that the method can be used at powers low enough to prevent degradation of the circuit and high enough to generate an unambiguous thermal response.

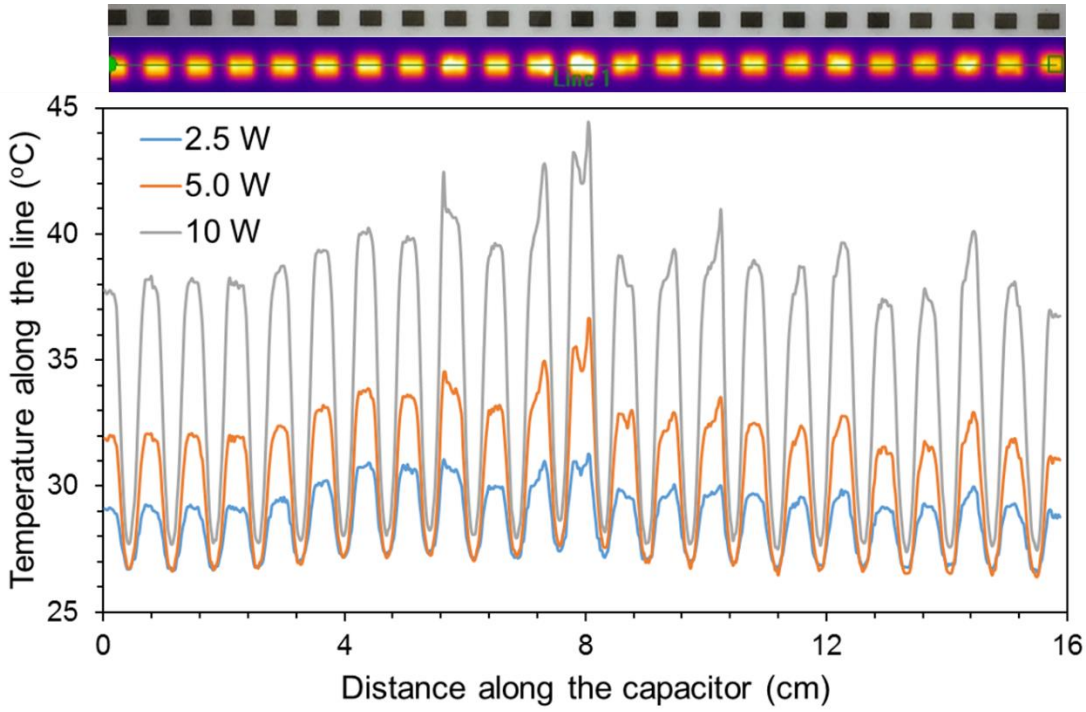

Figure IV-6. Temperature change along the single row of a passable CNT printed sheet at different powers and a frequency of 60 MHz. (Note that the original row of CNT print and its corresponding thermal image during RF heating is also given in the figure.) Reprinted with permission from reference [138], Copyright 2019 Elsevier Ltd.

For each commercial circuit, the CNT ink must be printed on top of a set of silver (Ag) electrodes, which may complicate the analysis. **Figure IV-7** shows a sheet of passable CNT circuits with silver electrodes and its corresponding RF heating profile after scanning through the fringing-field. This image also shows a distinct thermal response for each circuit, indicating that the method can be useful for analyzing circuits that are more

developed. From this response, it is clear that the majority of the circuits are uniform and conductive. (Note that several circuits are not as conductive as the others.) This demonstrates that the thermal imaging analysis is directly applicable to commercial production lines.

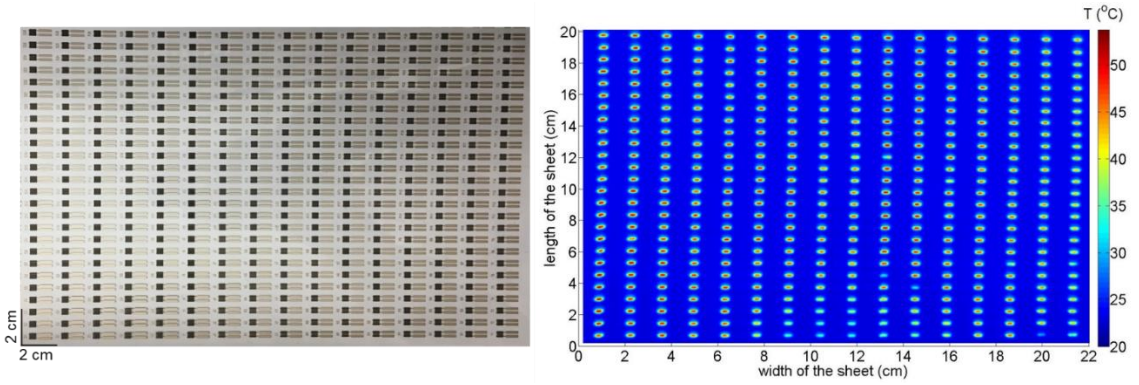

Figure IV-7. CNT circuits with Ag electrodes and the corresponding RF heating profile after scanning at the rate of 5.6 mm/s through a 60 MHz, 2.5 W fringing-field. Reprinted with permission from reference [138], Copyright 2019 Elsevier Ltd.

In addition to CNTs, industry uses a variety of conductive nanomaterials to create conductive circuits, such as carbon black (CB). The conductivity of carbon black also makes it susceptible to low frequency RF fields similar to carbon nanotubes. Since carbon black heats in response to a low frequency fringing-field, the scanning method can also be used on CB-based circuits. **Figures IV-8a and IV-8b** show two sets of CB circuits with corresponding RF heating profiles. These samples were also created by Brewer Science in the same manner as the CNT samples. Each sheet was passed over the fringing-field capacitor in the same manner as the CNT sheets. The thermal image of the faulty print clearly shows the defects in the print. Areas with insufficient carbon black coverage have no noticeable thermal response to the fringing-field, whereas, more covered areas show a

distinct response. The thermal image of the passable print indicates that several of the circuits contain non-uniformities in surface coverage (dark spots) even though the circuits were all classified as passable (resistances <25kΩ) when supplied by the manufacturer. This proves that RF heating is a superior technique that can detect facets of circuit performance which would not have been possible with the 2-point resistance measurements or visual inspection.

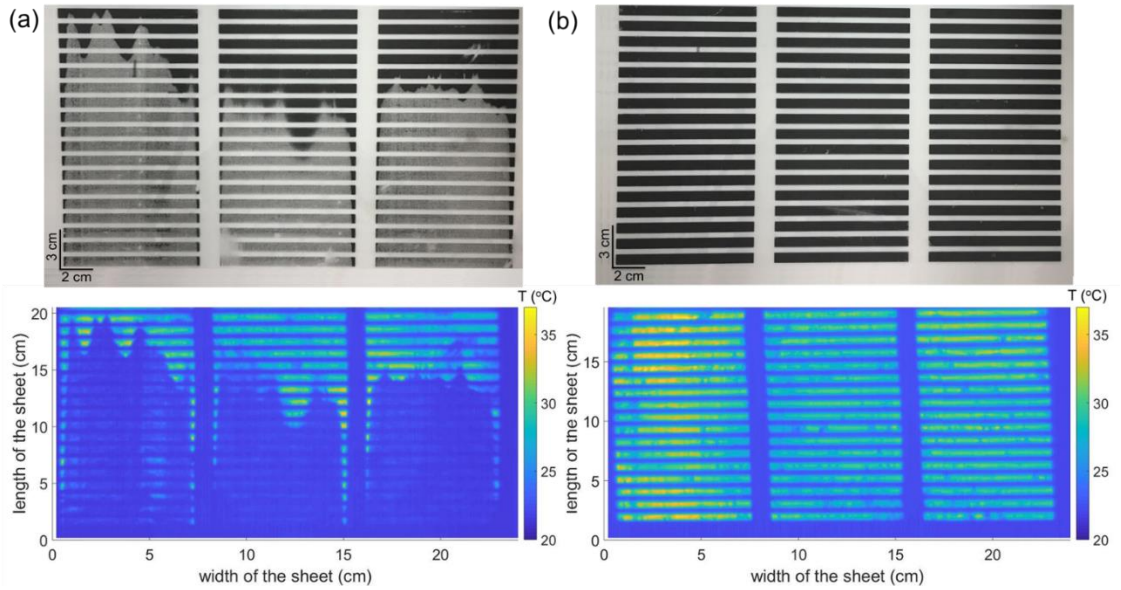

Figure IV-8. (a) Faulty and (b) passable CB prints and their corresponding RF heating profile after scanning at the rate of 5.6 mm/s through a 60 MHz, 2.5 W fringing-field. Note the lack of thermal response from the poor-quality circuits in (a). Reprinted with permission from reference [138], Copyright 2019 Elsevier Ltd.

Finally, the same test was also performed on carbon black/Ag electrode circuits shown in **Figure IV-9**. Compared to CNT/Ag circuits, these have significant amount of silver under the carbon black deposit which prevents the whole circuit to heat up uniformly. Therefore, the thermal response corresponds to areas with no silver underneath.

However, the non-functional circuits can still be quickly and easily identified from the thermal response.

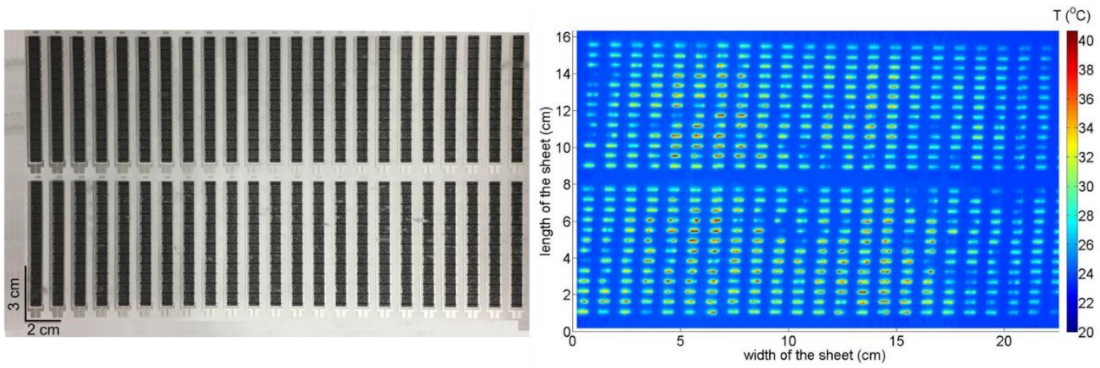

Figure IV-9. CB circuits with Ag electrodes and the corresponding RF heating profile after scanning at the rate of 5.6 mm/s through a 60 MHz, 1.6 W fringing-field. Reprinted with permission from reference [138], Copyright 2019 Elsevier Ltd.

Overall, the results show that this technique makes it possible to remove faulty circuits from the production line without the need to test each circuit individually, and can significantly speed-up the production process of carbon nanomaterial-based electronics.

Conclusions

The scanning method described here can be used as a reliable, high-throughput screening method for printed CNT structures. This method is ideal to replace previous, time-consuming quality metrics for more efficient production of CNT circuits. It provides a tenfold increase of speed, allowing for real-time monitoring of circuits as they are produced. The scanning method is more reliable than the traditional metric in screening-out faulty circuits; this method can also be employed at various stages of the circuit manufacturing process.

Similarly, this scanning method can be used to analyze both carbon nanotube and carbon black-based circuits because both of these carbon materials react to the RF fringing-field. This indicates that the method could be used to analyze circuits created with any type of RF-responsive material, including graphene family materials. The RF field can be tuned for each material and working geometry to adjust the maximum heat experienced by each circuit to prevent damage.

In addition, this method can be used with any substrate that has a low enough dielectric constant. Low dielectric materials are essentially invisible to the RF field and does not affect the response of the conductive circuits. As long as the substrate is thin enough that the fringing-field overlaps the path of the circuits, the method will be successful.

Although these proof-of-concept experiments focus on rectangular and simple circuits, this method is also applicable to complex circuit shapes because any given circuit is heated in increments as it is scanned through the fringing-field. This allows for a scanning and imaging technique that can find defects and inconsistencies in complex 2D printed structures.

CHAPTER V

JOULE HEATING OF CARBON PIXELS FOR ON-DEMAND THERMAL PATTERNING*

Introduction

The Joule heating effect in carbon-based conductive materials such as graphite,[167] carbon nanotubes (CNTs),[168] carbon nanofibers (CNFs),[169] and graphene[170] has allowed for light-weight, low-cost, and energy efficient two-dimensional (2D) heaters for thermotherapy,[171] defrosting and deicing systems,[168, 172] and thermal displays.[173-174] The possibility of non-contact Joule heating of carbon has also extended the applications to characterizing high-performance electronics,[138] composite manufacturing,[53] welding of polymers,[55] and 3D printing.[56] Patterned heating is also possible using carbon-based materials due to the ease of processing into thin films and their assembly into grids.[174-175] The production of scalable and controllable Joule heating elements relies on the method used for processing of carbon-based materials into thin films. Solution-based processing of carbon such as ink printing and spraying provides a high-throughput route compared to solid processing techniques such as array-drawing or direct-spinning.[21] For example, Philip *et al.*[176] showed mass production of large area graphite-based heaters using screen

* Reprinted with permission from "Joule heating of carbon pixels for on-demand thermal patterning" by Muhammad Anas; Mazin M. Mustafa; Daniel G. Carey; Anubhav Sarmah; Joshua J. LeMonte; Micah J. Green, 2021. *Carbon*, 174, 518-523, Copyright 2021 Elsevier Ltd.

printing. Hao *et al.*[177] used a portable commercial spray gun to make highly efficient graphene-based Joule heaters for thermal therapy.

Additionally, the choice of applicator to transform electrical energy into heat is crucial for scalable patterned heating. Both direct current (DC) power and alternating current (AC) power-based applicators are promising for heating of carbon. AC fields at high frequencies provide benefit of non-contact heating as well, which would be useful in applications such as deicing and defrosting to avoid short circuits due to water contacting the electronics.[161] Our group has previously demonstrated contact and non-contact heating of various materials such as CNTs, carbon black, CNFs, and graphene using AC fields at radio frequencies (1-200 MHz) and microwave (2.45 GHz).[50, 53, 55, 138] It is also possible to create large area patternable heaters using a suitable applicator that operates at a specific frequency.

In this work, we show that a range of applicators and materials can be used for patternable heating via thermal "pixels." The heating of an individual pixel is a function of both the material properties and dimensions as well as the applied power. These pixels are quickly produced and are used to create on-demand thermal patterns. The heating of pixels also allows for rapid damage sensing on surfaces.

Results and Discussion

We used airbrush spraying of commercial graphitic ink to rapidly produce thermal pixels. **Figure V-1a** shows the schematic of the spraying setup.

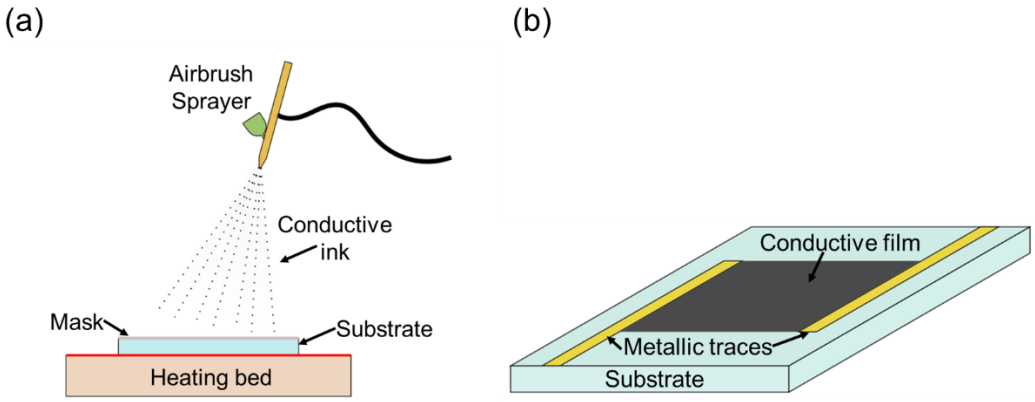

Figure V-1. Schematic of (a) spraying setup for making conductive thin films; (b) DC applicator for heating a single carbon pixel. Reprinted with permission from reference [178], Copyright 2021 Elsevier Ltd.

Different materials such as polyimide (PI), polyethylene terephthalate (PET), ceramic, and FR4 can be used as substrates for spraying graphitic ink to make thermal pixels. Pixels were made in a square (2 cm x 2 cm) using a stencil while spraying. Since surface conductivity (inverse of sheet resistance) is an important property for heating of thin films, it is easy to control the conductivity by varying the number of spray passes while keeping the concentration and flowrate of the ink constant. **Figure V-1b** shows the schematic of a DC applicator for heating a single pixel. The metallic traces are created by using a copper-coated substrate and etching out the copper that is not needed using an

acidic salt such as sodium persulfate. This technique of fabricating metallic traces allows for easy scale up and avoids the use of metallic paint, which is prone to cracking once dried. The graphite ink is then sprayed using a mask such that the sprayed film is in contact with the metallic traces.

Figure V-2a shows the steady-state temperature as a function of surface conductivity (σ_s) for graphite pixel (2 cm x 2 cm) at a constant voltage of 30 V using a DC applicator. **Figure V-2b** shows temperature as a function of time at different absorbed powers for a pixel of surface conductivity of 1.7 mS. It is also possible to increase the steady-state temperature by tuning the power supplied. High temperatures of up to 150 °C are obtained at DC powers as low as 2.1 W. The inset image confirms that the heating is uniform over the area of the pixel.

The temperature increases with the conductivity due to increase in current flow and thus absorbed power. However, the steady-state temperature reaches a maximum with conductivity when the maximum power available from the power supply is absorbed by the pixel. **Figure V-3a** confirms the non-monotonic relationship between steady-state temperature and surface conductivity for a maximum power of 6.9 W (30 V, 0.23 A). The highest temperature of 180 °C observed corresponds to the absorption of maximum available power as seen in **Figure V-3b**. Note that the current and voltage were restricted to 30 V and 0.23 A in the power supply to obtain the non-monotonic relationship.

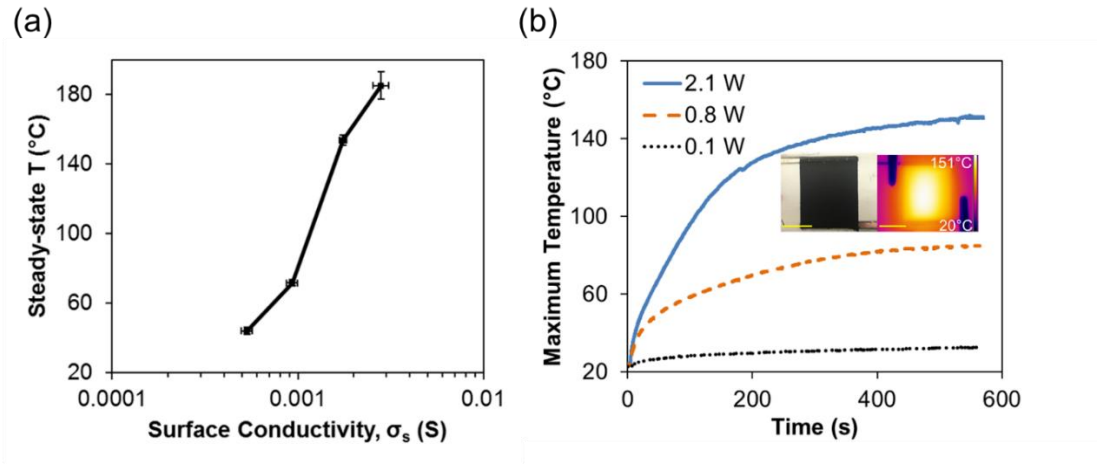

Figure V-2. (a) Steady-state temperature at 30 V as a function of surface conductivity for graphite films on FR4 substrate; (b) Maximum temperature as a function of time at different powers for a graphite film of σ_s = 1.7 mS. Inset: Digital image and steady-state thermal image at 2.1 W of a single graphitic pixel (scale bar: 1 cm). Reprinted with permission from reference [178], Copyright 2021 Elsevier Ltd.

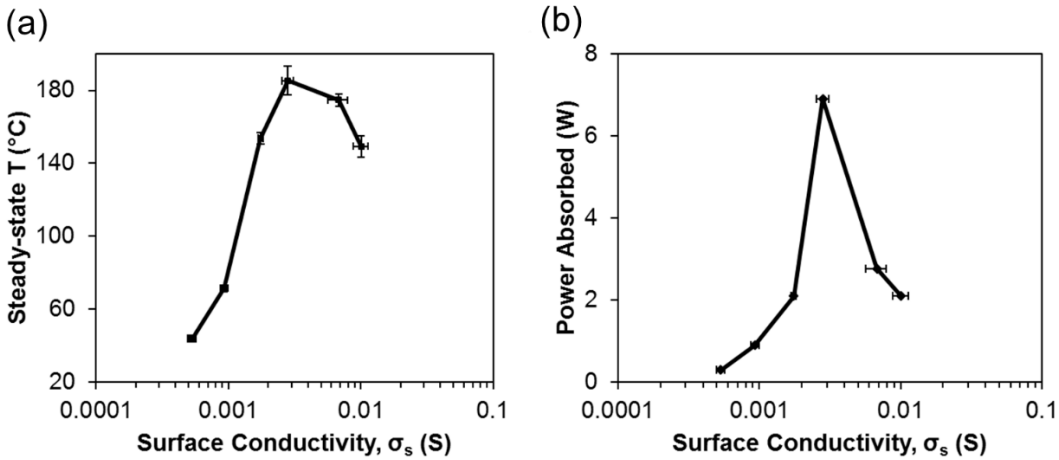

Figure V-3. (a) Steady-state temperature as a function of graphite pixel surface conductivity for maximum available DC power of 6.9 W (going from low to high conductivity: first four data points same as in Figure 2) (b) Power absorbed as a function of surface conductivity. Reprinted with permission from reference [178], Copyright 2021 Elsevier Ltd.

In addition to direct-contact heating using DC power, it is also possible to induce non-contact Joule heating in carbon using AC power. **Figure V-4** shows heating of a graphite pixel (2 cm x 2 cm) using a patch antenna operating at 2.45 GHz. Patch antennas are normally used to radiate communication signals. However, we modified the patch antenna design by first introducing copper walls which confine the radiated electromagnetic waves within the area of the patch. We then used low-loss dielectric foam separators that prevent electromagnetic coupling between individual thermal pixels and acts as a thermal insulator. Note that the thin films were simulated as 2D boundaries rather than extremely thin volumetric objects to avoid numerical challenges.

It is seen in **Figure V-4a** that the steady-state temperature is non-monotonically related with the DC surface conductivity and has a maximum at DC surface conductivity of 2.5 mS. At lower conductivities, absorption of electromagnetic waves induces currents in the conductive film which heat via Joule effect. Therefore, as the conductivity is increased below the optimum, the steady-state temperature also increases. However, as the conductivity is increased beyond the optimum value, the reflection of electromagnetic waves increases, which leads to lower absorption and reduced heating. In order to uniformly and efficiently heat the pixel, it is important to have the surface conductivity which corresponds to maximum power absorption. **Figure V-4b** confirms that the heating can also be controlled by changing the power of the electromagnetic waves at a constant surface conductivity.

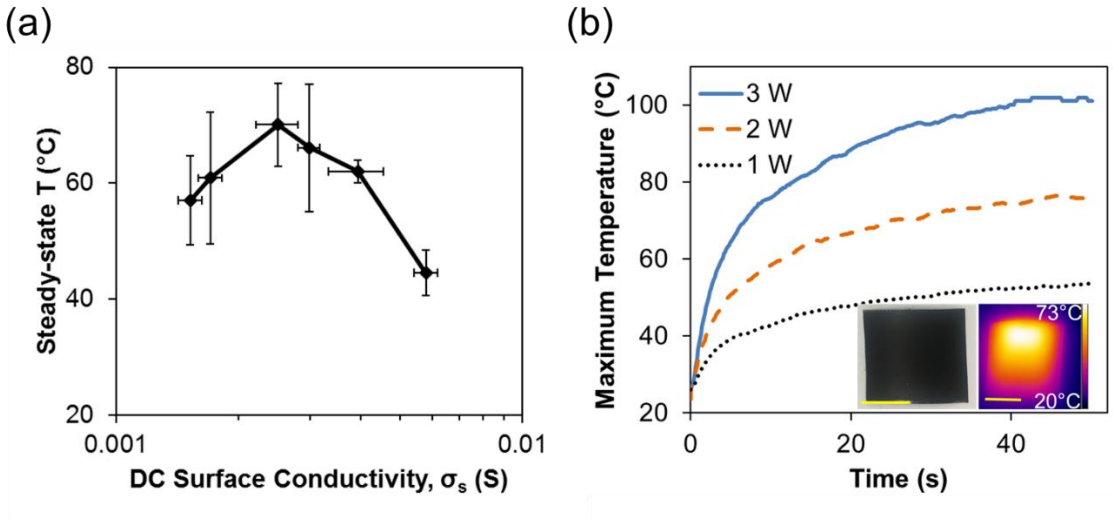

Figure V-4. (a) Steady-state temperature as a function of DC surface conductivity for graphite films on polyimide substrate using patch antenna applicator at a power of 2 W and frequency of 2.45 GHz; (b) Maximum temperature as a function of time at different powers and 2.45 GHz for a graphite film of σ_s = 2.5 mS. Inset: Digital image and steady-state thermal image at 2 W of a single graphitic pixel (scale bar: 1 cm). Reprinted with permission from reference [178], Copyright 2021 Elsevier Ltd.

Figure V-5 shows the simulated electromagnetic heating of a conductive thin film using patch antenna applicator operating at 2.45 GHz. **Figure V-5a** shows steady-state temperature as a function of AC surface conductivity. The simulation also confirms the non-monotonic relationship observed in the experiments. The maximum point is observed at around AC conductivity of 6.0 mS. **Figure V-5b** shows temperature as a function of time at a power of 2 W. Note that the temperature is higher than that in the experiment at the same power due to ideal scenario in the simulation and possible deviations in the heat transfer parameters used in the simulations from those of the actual test materials. The inset confirms similar heating profile to that of the experiment.

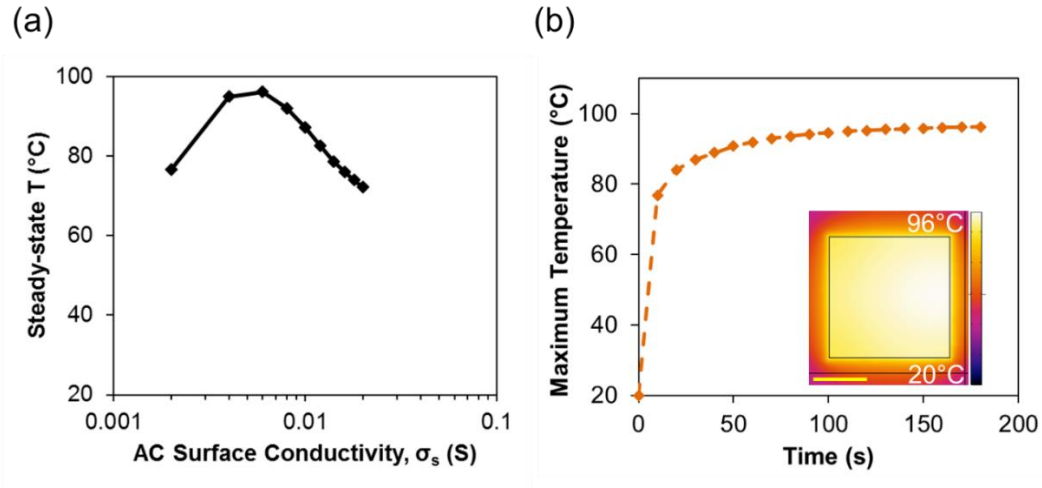

Figure V-5. (a) Simulated steady-state temperature (at 180 s) as a function of AC surface conductivity for conductive films using patch antenna applicator at power of 2 W and frequency of 2.45 GHz; (b) Simulated maximum temperature as a function of time and steady-state thermal profile at 2 W and 2.45 GHz for a conductive film of σ_s = 6.0 mS (inset scale bar: 1 cm). Reprinted with permission from reference [178], Copyright 2021 Elsevier Ltd.

Figure V-6 shows a large area DC applicator for heating multiple pixels and the corresponding steady-state thermal image at 45 W DC power. The applicator consists of the metallic traces and the sprayed graphite pixels. The metallic traces were fabricated using conventional printed circuit board (PCB) manufacturing technique where the metal that is not needed is etched away using an etchant solution such as sodium persulfate. This technique allows for a solid metallic layer to connect graphite pixels rather than using metallic ink which is resistive and is prone to cracking. The design of the metallic traces allows all pixels to be connected in a parallel arrangement so that the voltage difference is the same across all pixels. The pixels are created by spraying graphite ink using a stencil. The equivalent 2-point resistance of the sprayed pixels was around 20 Ω. If maximum

power absorption (and thus Joule heating) is desired, it is important to spray the pixels with a 2-point resistance value given by $R = V_{max}/I_{max}$, where V_{max} and I_{max} are the maximum available voltage and current from the DC power supply.

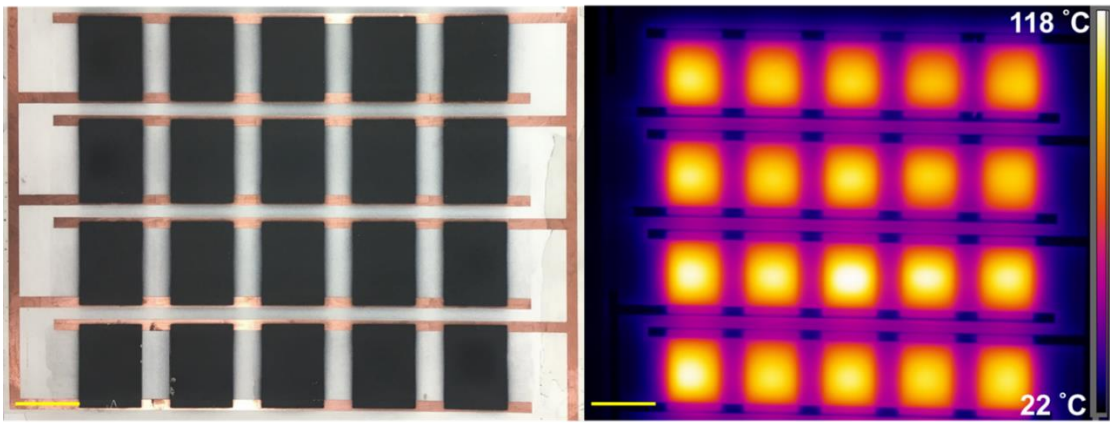

Figure V-6. Scaled-up DC applicator fabricated using persulfate-etched copper circuit on FR4 and airbrush sprayed graphite ink, and the corresponding steady-state thermal image via DC power. Scale bar is 2 cm. Reprinted with permission from reference [178], Copyright 2021 Elsevier Ltd.

Many applications require uniform heating over a full area of the Joule heater; however, there is an interest in making heaters with temperature gradients for applications in thermal displays as well as targeted curing of composites.[175, 179] **Figure V-7** shows a patterned 'T' heating with temperature gradients using a scaled-up DC applicator. The surface conductivity of each pixel can be varied to obtain different temperatures over the heating area. It is also possible to make these applicators flexible by using a flexible metal coated substrate such as Kapton (polyimide). This could potentially be useful in thermochromic structures such as tiles and displays where various colors can be obtained by using thermal gradients.

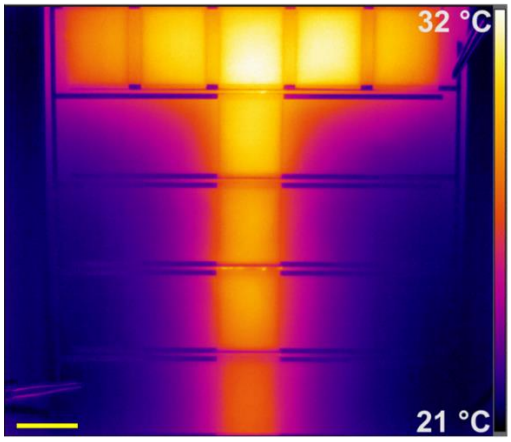

Figure V-7. Steady-state thermal image of patterned 'T' shape made using sprayed graphite ink on FR4 and heated via DC power. Scale bar is 2 cm. Reprinted with permission from reference [178], Copyright 2021 Elsevier Ltd.

It is also possible to scale up the patch applicator for non-contact heating of multiple pixels. **Figure V-8** shows a 2 x 2 array of patch antennas connected for heating a 4 x 4 grid of graphite pixels**.** Since the pixels are not in contact with the applicator, they can be quickly sprayed on any substrate which allows for greater flexibility. A face-like thermal pattern is also shown in **Figure V-9** using an even larger patch applicator (4 x 4 array of patch antennas). Note that a power divider is used to split the power from the source to each individual patch antenna. Since the power divider has a specific power rating, it was not possible to supply high power to each patch antenna for heating large area to high temperatures. Additionally, the Federal Communications Commission (FCC) regulates the maximum radiated power from these applicators, thereby limiting their applications to areas where high temperatures are required, and human interaction is frequent.

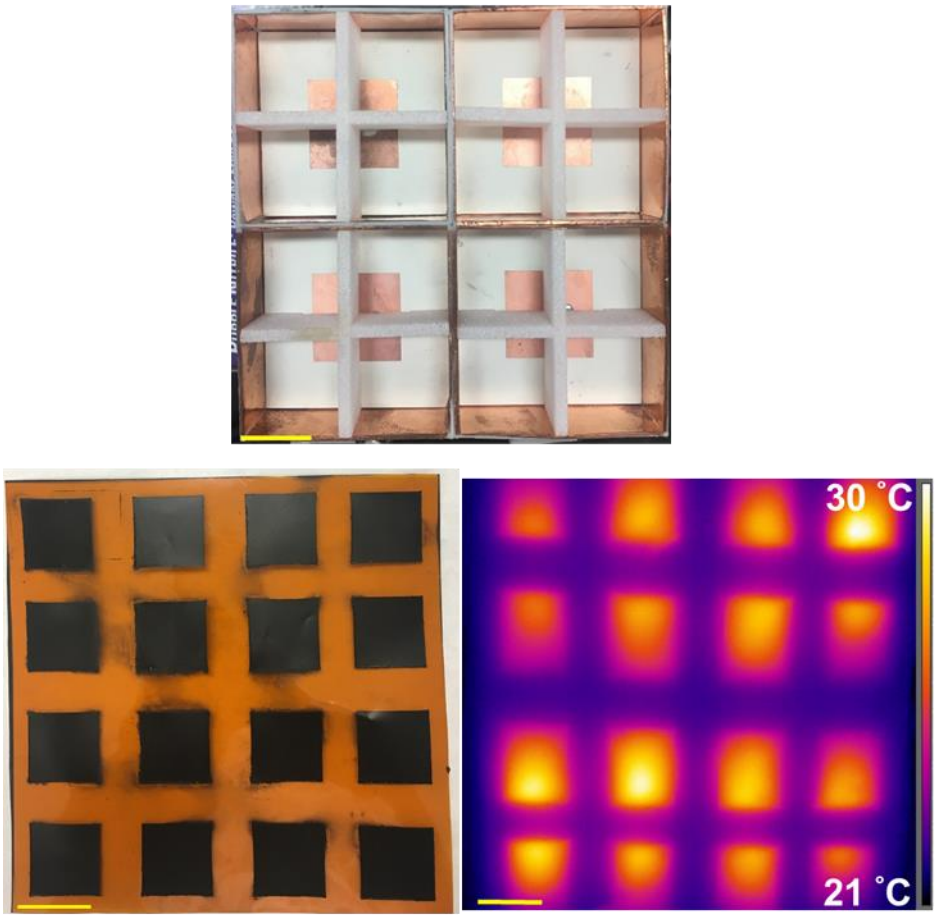

Figure V-8. Scaled-up patch antenna applicator, array of airbrush sprayed graphite pixels on polyimide, and the corresponding steady-state thermal image of array. Scale bar is 2 cm. Reprinted with permission from reference [178], Copyright 2021 Elsevier Ltd.

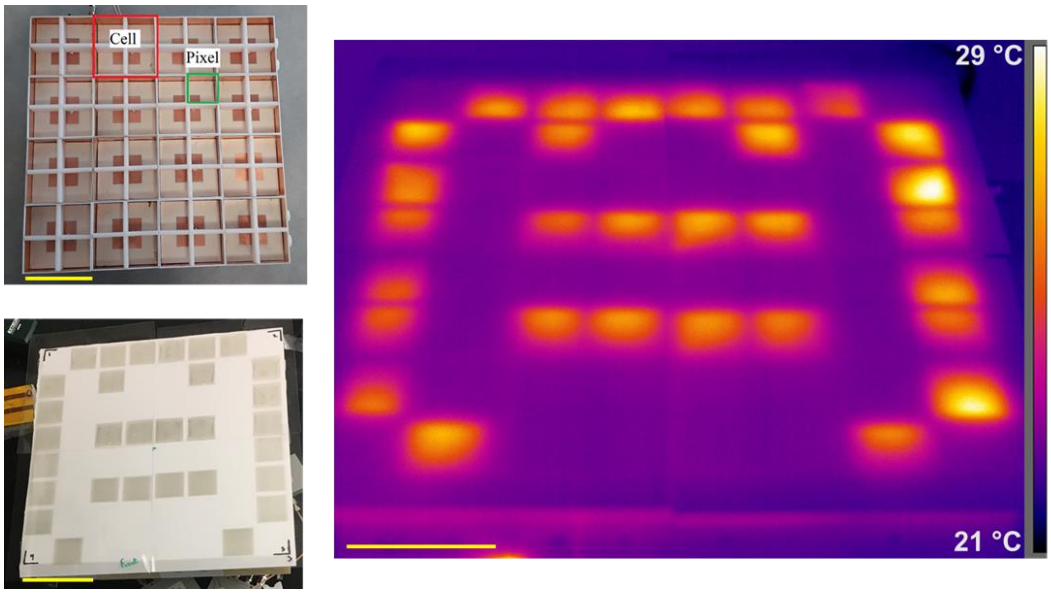

Figure V-9. Scaled-up patch antenna applicator and the steady-state thermal image of a face-like thermal pattern. Scale bar is 6 cm. Reprinted with permission from reference [178], Copyright 2021 Elsevier Ltd.

Figure V-10 shows that other carbon-based materials can also be used for patterned heating using both DC and non-contact AC applicators to make a "TAMU" acronym. The patterned 'A' is made using laser-induced graphene (LIG) on polyether ether ketone (PEEK) and heated using 2 x 2 array of patch antennas. LIG can be coated with polydimethlylsiloxane (PDMS) to protect it from weathering. The patterned 'M' is made using CNT ink and heated via DC applicator. DC applicator can be coated with polyimide (PI) tape to protect the sprayed pixels from weathering. The patterned 'U' is made using graphite ink sprayed on polyimide and heated via a 2 x 2 array of patch antennas.

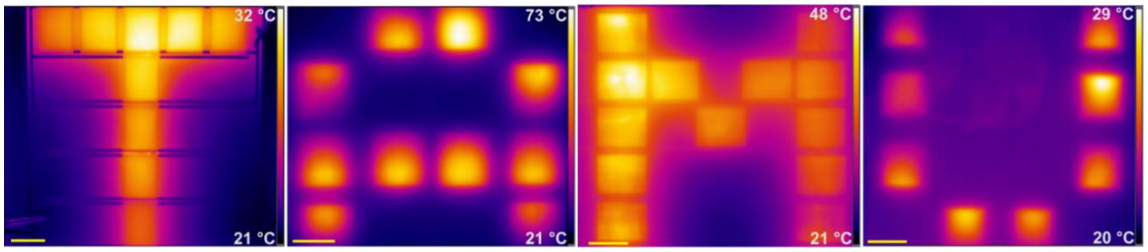

Figure V-10. Multiple sample types and applicators can be used in arrays to create thermal patterns. Examples: (T) Patterned 'T' made using sprayed graphite ink on FR4 and heated via DC power, same as in Figure 6; (A) Patterned 'A' made using LIG on PEEK (coated with PDMS) and heated via microwave; (M) Patterned 'M' made using sprayed CNT ink on FR4 and heated via DC power (applicator coated with PI tape); (U) Patterned 'U' made using sprayed graphite ink on polyimide and heated via microwave. All thermal images are taken at steady state. Scale bar is 2 cm. Reprinted with permission from reference [178], Copyright 2021 Elsevier Ltd.

Joule heating (and thermal imaging) of conductive coatings could also be a helpful metric for sensing damage on surfaces. This is a more reliable technique compared to conventional resistance measurement because it allows for precise detection of spatial variations.[180] **Figure V-11** shows that Joule heating is mostly uniform over the surface of undamaged coating whereas the non-uniformities in heating due to damage are clearly visible in the thermal image. Note that it is possible to detect damages not seen with the naked eye using a high-resolution thermal camera.

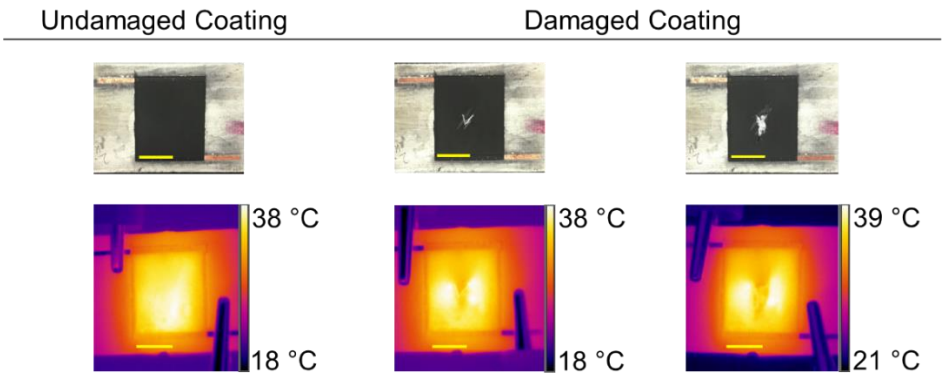

Figure V-11. Damage sensing of graphite coatings using Joule heating for 1 min. Scale bar is 1 cm. Reprinted with permission from reference [178], Copyright 2021 Elsevier Ltd.

Conclusions

We showed that thermal pixels can be quickly produced using a portable airbrush sprayer and a commercial graphitic ink. We demonstrated performance of DC applicator for large area patterned heating using thermal pixels. We also showed that AC fields at high frequencies can be used for non-contact heating via a patch antenna applicator. Multiple patch antennas can be connected in an array to produce heating over a large area. We found that there is an optimum conductivity of the pixel associated with efficient heating in all types of applicators. The conductivity of the individual pixel can also be varied to produce thermal gradients within a specific area. The applicators work with a range of carbon-based materials and could be easily applied to create complex thermal displays. The applicators could also be used to induce Joule heating in the conductive coatings to sense damages.

CHAPTER VI

CONCLUSION

In this dissertation, it is confirmed via experiments and simulations that the radio frequency (RF) heating behavior is non-monotonically related with the electrical conductivity of films. This trend is universal as it applies to a range of carbon-based nanomaterials such as chirality-sorted single-walled carbon nanotubes, laser-induced graphene, and multi-walled carbon nanotubes as well as composites such as carbon nanofiber-polyamide and carbon nanostructures-polycarbonate. We also showed that the underlying science is the same for high frequency microwave (MW) heating. We further demonstrated a novel method to rapidly screen carbon nanotube and carbon black circuits from a production line via scanning over RF fields to generate a heat signature. Finally, we presented techniques to produce large-area thermal patterns using both direct current and alternating current-induced heating of carbon-based materials.

Radio frequency heating of carbon-based nanomaterials is an evolving field and there are still areas to explore for future. In this work, we confirmed that the trend between electrical properties and RF heating is non-monotonic and generalizable; however, both material and the type of applicator can shift this trend horizontally (left right) as well as vertically (up down). One possible area to investigate in the future would be the effect of different forms of nanomaterials on the interaction with electric fields. For instance, the RF field interaction and thus heating is expected to be different for film versus aerogel of

nanomaterial. Additionally, the interaction of RF fields with new types of electrically conductive nanomaterials such as MXenes can also be studied and compared with that of carbon-based nanomaterials. These new investigations would provide a framework to optimize integration of RF responsive materials with catalyst supports that can undergo localized heating via RF fields to drive green manufacturing.[181]

Furthermore, as more materials that heat in response to RF fields are being explored, it is also viable to develop RF heating response as a material characterization technique. Each material shows a unique frequency-dependent heat signature due to its composition, structure, and morphology; therefore, it is possible to characterize materials by studying their RF heating response.

REFERENCES

1. Georgakilas, V.; Perman, J. A.; Tucek, J.; Zboril, R., Broad Family of Carbon Nanoallotropes: Classification, Chemistry, and Applications of Fullerenes, Carbon Dots, Nanotubes, Graphene, Nanodiamonds, and Combined Superstructures. *Chemical Reviews* **2015,** *115* (11), 4744-4822.

2. Popov, I. V.; Görne, A. L.; Tchougréeff, A. L.; Dronskowski, R., Relative stability of diamond and graphite as seen through bonds and hybridizations. *Physical Chemistry Chemical Physics* **2019,** *21* (21), 10961-10969.

3. Kroto, H. W.; Heath, J. R.; O'Brien, S. C.; Curl, R. F.; Smalley, R. E., C60: Buckminsterfullerene. *Nature* **1985,** *318* (6042), 162-163.

4. Iijima, S., Helical microtubules of graphitic carbon. *Nature* **1991,** *354* (6348), 56-58.

5. Novoselov, K. S.; Geim, A. K.; Morozov, S. V.; Jiang, D.; Zhang, Y.; Dubonos, S. V.; Grigorieva, I. V.; Firsov, A. A., Electric Field Effect in Atomically Thin Carbon Films. *Science* **2004,** *306* (5696), 666-669.

6. Vidu, R.; Rahman, M.; Mahmoudi, M.; Enachescu, M.; Poteca, T. D.; Opris, I., Nanostructures: a platform for brain repair and augmentation. *Frontiers in Systems Neuroscience* **2014,** *8* (91).

7. Lee, C.; Wei, X.; Kysar, J. W.; Hone, J., Measurement of the Elastic Properties and Intrinsic Strength of Monolayer Graphene. *Science* **2008,** *321* (5887), 385-388.

8. Wong, E.; Sheehan, P.; Lieber, C., Nanobeam Mechanics: Elasticity, Strength, and Toughness of Nanorods and Nanotubes. *Science* **1997,** *277* (5334), 1971-1975.

9. Popov, V. N., Carbon nanotubes: properties and application. *Materials Science and Engineering: R: Reports* **2004,** *43* (3), 61-102.

10. Belin, T.; Epron, F., Characterization methods of carbon nanotubes: a review. *Materials Science and Engineering: B* **2005,** *119* (2), 105-118.

11. Bolotin, K. I.; Sikes, K. J.; Jiang, Z.; Klima, M.; Fudenberg, G.; Hone, J.; Kim, P.; Stormer, H. L., Ultrahigh electron mobility in suspended graphene. *Solid state communications* **2008,** *146* (9-10), 351-355.

12. Allen, M. J.; Tung, V. C.; Kaner, R. B., Honeycomb Carbon: A Review of Graphene. *Chemical Reviews* **2010,** *110* (1), 132-145.

13. Yang, F.; Wang, M.; Zhang, D.; Yang, J.; Zheng, M.; Li, Y., Chirality Pure Carbon Nanotubes: Growth, Sorting, and Characterization. *Chemical Reviews* **2020,** *120* (5), 2693-2758.

14. Bachtold, A.; Hadley, P.; Nakanishi, T.; Dekker, C., Logic Circuits with Carbon Nanotube Transistors. *Science* **2001,** *294* (5545), 1317.

15. Grobert, N., Carbon nanotubes – becoming clean. *Materials Today* **2007,** *10* (1), 28-35.

16. Wu, K.; Niu, Y.; Zhang, Y.; Yong, Z.; Li, Q., Continuous growth of carbon nanotube films: From controllable synthesis to real applications. *Composites Part A: Applied Science and Manufacturing* **2021,** *144*, 106359.

17. Nerushev, O. A.; Sveningsson, M.; Falk, L. K. L.; Rohmund, F., Carbon nanotube films obtained by thermal chemical vapour deposition. *Journal of Materials Chemistry* **2001,** *11* (4), 1122-1132.

18. Hsu, C. M.; Lin, C. H.; Chang, H. L.; Kuo, C. T., Growth of the large area horizontally-aligned carbon nanotubes by ECR-CVD. *Thin Solid Films* **2002,** *420-421*, 225-229.

19. Hu, L.; Hecht, D. S.; Grüner, G., Carbon Nanotube Thin Films: Fabrication, Properties, and Applications. *Chemical Reviews* **2010,** *110* (10), 5790-5844.

20. Brownson, D. A. C.; Banks, C. E., The electrochemistry of CVD graphene: progress and prospects. *Physical Chemistry Chemical Physics* **2012,** *14* (23), 8264-8281.

21. Janas, D.; Koziol, K. K., A review of production methods of carbon nanotube and graphene thin films for electrothermal applications. *Nanoscale* **2014,** *6* (6), 3037-3045.

22. Wu, Z.; Chen, Z.; Du, X.; Logan, J. M.; Sippel, J.; Nikolou, M.; Kamaras, K.; Reynolds, J. R.; Tanner, D. B.; Hebard, A. F.; Rinzler, A. G., Transparent, Conductive Carbon Nanotube Films. *Science* **2004,** *305* (5688), 1273.

23. Shobin, L. R.; Manivannan, S., Enhancement of electrothermal performance in single-walled carbon nanotube transparent heaters by room temperature post treatment. *Solar Energy Materials and Solar Cells* **2018,** *174*, 469-477.

24. Beecher, P.; Servati, P.; Rozhin, A.; Colli, A.; Scardaci, V.; Pisana, S.; Hasan, T.; Flewitt, A. J.; Robertson, J.; Hsieh, G. W.; Li, F. M.; Nathan, A.; Ferrari, A. C.; Milne,

W. I., Ink-jet printing of carbon nanotube thin film transistors. *Journal of Applied Physics* **2007,** *102* (4), 043710.

25. Liang, X.; Fu, Z.; Chou, S. Y., Graphene Transistors Fabricated via Transfer-Printing In Device Active-Areas on Large Wafer. *Nano Letters* **2007,** *7* (12), 3840-3844.

26. Yavari, F.; Koratkar, N., Graphene-Based Chemical Sensors. *The Journal of Physical Chemistry Letters* **2012,** *3* (13), 1746-1753.

27. Zhang, Y.-Z.; Wang, Y.; Cheng, T.; Yao, L.-Q.; Li, X.; Lai, W.-Y.; Huang, W., Printed supercapacitors: materials, printing and applications. *Chemical Society Reviews* **2019,** *48* (12), 3229-3264.

28. Li, Z.; Liang, Z., Optimization of Buckypaper-enhanced Multifunctional Thermoplastic Composites. *Scientific Reports* **2017,** *7* (1), 42423.

29. Yee, M. J.; Mubarak, N. M.; Khalid, M.; Abdullah, E. C.; Jagadish, P., Synthesis of polyvinyl alcohol (PVA) infiltrated MWCNTs buckypaper for strain sensing application. *Scientific Reports* **2018,** *8* (1), 17295.

30. Mehmood, A.; Mubarak, N. M.; Khalid, M.; Jagadish, P.; Walvekar, R.; Abdullah, E. C., Graphene/PVA buckypaper for strain sensing application. *Scientific Reports* **2020,** *10* (1), 20106.

31. Kashiwagi, T.; Grulke, E.; Hilding, J.; Harris, R.; Awad, W.; Douglas, J., Thermal Degradation and Flammability Properties of Poly(propylene)/Carbon Nanotube Composites. *Macromolecular Rapid Communications* **2002,** *23* (13), 761-765.

32. Najafi, E.; Shin, K., Radiation resistant polymer–carbon nanotube nanocomposite thin films. *Colloids and Surfaces A: Physicochemical and Engineering Aspects* **2005,** *257-258*, 333-337.

33. Kim, G. H.; Hwang, D. H.; Woo, S. I., Thermoelectric properties of nanocomposite thin films prepared with poly(3,4-ethylenedioxythiophene) poly(styrenesulfonate) and graphene. *Physical Chemistry Chemical Physics* **2012,** *14* (10), 3530-3536.

34. Siqueira, J. R.; Oliveira, O. N., 9 - Carbon-Based Nanomaterials. In *Nanostructures*, Da Róz, A. L.; Ferreira, M.; de Lima Leite, F.; Oliveira, O. N., Eds. William Andrew Publishing: 2017; pp 233-249.

35. Wang, Y.; Weng, G. J., Electrical Conductivity of Carbon Nanotube- and Graphene-Based Nanocomposites. In *Micromechanics and Nanomechanics of Composite Solids*, Meguid, S. A.; Weng, G. J., Eds. Springer International Publishing: Cham, 2018; pp 123-156.

36. Rossouw, D.; Botton, G. A.; Najafi, E.; Lee, V.; Hitchcock, A. P., Metallic and Semiconducting Single-Walled Carbon Nanotubes: Differentiating Individual SWCNTs by Their Carbon 1s Spectra. *ACS Nano* **2012,** *6* (12), 10965-10972.

37. Haddon, R. C.; Sippel, J.; Rinzler, A. G.; Papadimitrakopoulos, F., Purification and Separation of Carbon Nanotubes. *MRS Bulletin* **2004,** *29* (4), 252-259.

38. Lee, S. H.; Lee, D. H.; Lee, W. J.; Kim, S. O., Tailored Assembly of Carbon Nanotubes and Graphene. *Advanced Functional Materials* **2011,** *21* (8), 1338-1354.

39. Zhang, Z.; Huang, H.; Yang, X.; Zang, L., Tailoring Electronic Properties of Graphene by π–π Stacking with Aromatic Molecules. *The Journal of Physical Chemistry Letters* **2011,** *2* (22), 2897-2905.

40. Lee, B. M.; Loh, K. J., A 2D percolation-based model for characterizing the piezoresistivity of carbon nanotube-based films. *Journal of Materials Science* **2015,** *50* (7), 2973-2983.

41. Pan, Y.; Weng, G. J.; Meguid, S. A.; Bao, W. S.; Zhu, Z. H.; Hamouda, A. M. S., Percolation threshold and electrical conductivity of a two-phase composite containing randomly oriented ellipsoidal inclusions. *Journal of Applied Physics* **2011,** *110* (12), 123715.

42. Nan, C. W.; Shen, Y.; Ma, J., Physical Properties of Composites Near Percolation. *Annual Review of Materials Research* **2010,** *40* (1), 131-151.

43. Gardea, F.; Lagoudas, D. C., Characterization of electrical and thermal properties of carbon nanotube/epoxy composites. *Composites Part B: Engineering* **2014,** *56*, 611-620.

44. Rosales, L.; González, J. W., Transport properties of two finite armchair graphene nanoribbons. *Nanoscale Research Letters* **2013,** *8* (1), 1.

45. Imholt, T. J.; Dyke, C. A.; Hasslacher, B.; Perez, J. M.; Price, D. W.; Roberts, J. A.; Scott, J. B.; Wadhawan, A.; Ye, Z.; Tour, J. M., Nanotubes in Microwave Fields: Light Emission, Intense Heat, Outgassing, and Reconstruction. *Chemistry of Materials* **2003,** *15* (21), 3969-3970.

46. Vázquez, E.; Prato, M., Carbon Nanotubes and Microwaves: Interactions, Responses, and Applications. *Acs Nano* **2009,** *3* (12), 3819-3824.

47. Higginbotham, A. L.; Moloney, P. G.; Waid, M. C.; Duque, J. G.; Kittrell, C.; Schmidt, H. K.; Stephenson, J. J.; Arepalli, S.; Yowell, L. L.; Tour, J. M., Carbon nanotube composite curing through absorption of microwave radiation. *Composites Science and Technology* **2008,** *68* (15), 3087-3092.

48. Rangari, V. K.; Bhuyan, M. S.; Jeelani, S., Microwave processing and characterization of EPON 862/CNT nanocomposites. *Materials Science and Engineering: B* **2010,** *168* (1), 117-121.

49. Sweeney, C. B.; Lackey, B. A.; Pospisil, M. J.; Achee, T. C.; Hicks, V. K.; Moran, A. G.; Teipel, B. R.; Saed, M. A.; Green, M. J., Welding of 3D-printed carbon nanotube–polymer composites by locally induced microwave heating. *Science Advances* **2017,** *3* (6), e1700262.

50. Haile, M.; Sweeney, C. B.; Lackey, B. A.; Sarwar, O.; Henderson, R.; Saed, M. A.; Green, M. J.; Grunlan, J. C., Ultrafast and Highly Localized Microwave Heating in Carbon Nanotube Multilayer Thin Films. *Advanced Materials Interfaces* **2017,** *4* (15), 1700371.

51. Marra, F.; Zhang, L.; Lyng, J. G., Radio frequency treatment of foods: Review of recent advances. *Journal of Food Engineering* **2009,** *91* (4), 497-508.

52. Gannon, C. J.; Cherukuri, P.; Yakobson, B. I.; Cognet, L.; Kanzius, J. S.; Kittrell, C.; Weisman, R. B.; Pasquali, M.; Schmidt, H. K.; Smalley, R. E.; Curley, S. A., Carbon

nanotube-enhanced thermal destruction of cancer cells in a noninvasive radiofrequency field. *Cancer-Am Cancer Soc* **2007,** *110* (12), 2654-2665.

53. Vashisth, A.; Healey, R. E.; Pospisil, M. J.; Oh, J. H.; Green, M. J., Continuous processing of pre-pregs using radio frequency heating. *Composites Science and Technology* **2020,** *195*, 108211.

54. Patil, N.; Zhao, X.; Mishra, N. K.; Saed, M. A.; Radovic, M.; Green, M. J., Rapid Heating of Silicon Carbide Fibers under Radio Frequency Fields and Application in Curing Preceramic Polymer Composites. *ACS Applied Materials & Interfaces* **2019,** *11* (49), 46132-46139.

55. Gerringer, J. C.; Moran, A. G.; Habib, T.; Pospisil, M. J.; Oh, J. H.; Teipel, B. R.; Green, M. J., Radio Frequency Heating of Laser-Induced Graphene on Polymer Surfaces for Rapid Welding. *ACS Applied Nano Materials* **2019,** *2* (11), 7032-7042.

56. Sweeney, C. B.; Burnette, M. L.; Pospisil, M. J.; Shah, S. A.; Anas, M.; Teipel, B. R.; Zahner, B. S.; Staack, D.; Green, M. J., Dielectric Barrier Discharge Applicator for Heating Carbon Nanotube-Loaded Interfaces and Enhancing 3D-Printed Bond Strength. *Nano Letters* **2020,** *20* (4), 2310-2315.

57. Sweeney, C. B.; Moran, A. G.; Gruener, J. T.; Strasser, A. M.; Pospisil, M. J.; Saed, M. A.; Green, M. J., Radio Frequency Heating of Carbon Nanotube Composite Materials. *Acs Applied Materials & Interfaces* **2018,** *10* (32), 27252-27259.

58. Lee, W. J.; Clancy, A. J.; Fernández-Toribio, J. C.; Anthony, D. B.; White, E. R.; Solano, E.; Leese, H. S.; Vilatela, J. J.; Shaffer, M. S. P., Interfacially-grafted single-

walled carbon nanotube / poly (vinyl alcohol) composite fibers. *Carbon* **2019,** *146*, 162-171.

59. Gu, H.; Zhang, H.; Ma, C.; Xu, X.; Wang, Y.; Wang, Z.; Wei, R.; Liu, H.; Liu, C.; Shao, Q.; Mai, X.; Guo, Z., Trace electrosprayed nanopolystyrene facilitated dispersion of multiwalled carbon nanotubes: Simultaneously strengthening and toughening epoxy. *Carbon* **2019,** *142*, 131-140.

60. Simon, P.; Gogotsi, Y., Materials for electrochemical capacitors. *Nature Materials* **2008,** *7*, 845.

61. Simon, P.; Gogotsi, Y., Capacitive Energy Storage in Nanostructured Carbon–Electrolyte Systems. *Accounts of Chemical Research* **2013,** *46* (5), 1094-1103.

62. Hummer, G.; Rasaiah, J. C.; Noworyta, J. P., Water conduction through the hydrophobic channel of a carbon nanotube. *Nature* **2001,** *414* (6860), 188-190.

63. Kalra, A.; Garde, S.; Hummer, G., Osmotic water transport through carbon nanotube membranes. *Proceedings of the National Academy of Sciences* **2003,** *100* (18), 10175.

64. De Volder, M. F. L.; Tawfick, S. H.; Baughman, R. H.; Hart, A. J., Carbon Nanotubes: Present and Future Commercial Applications. *Science* **2013,** *339* (6119), 535.

65. Luo, X.; Weng, W.; Liang, Y.; Hu, Z.; Zhang, Y.; Yang, J.; Yang, L.; Yang, S.; Zhu, M.; Cheng, H.-M., Multifunctional fabrics of carbon nanotube fibers. *Journal of Materials Chemistry A* **2019,** *7* (15), 8790-8797.

66. Park, S.; Vosguerichian, M.; Bao, Z., A review of fabrication and applications of carbon nanotube film-based flexible electronics. *Nanoscale* **2013,** *5* (5), 1727-1752.

67. Lipomi, D. J.; Vosgueritchian, M.; Tee, B. C. K.; Hellstrom, S. L.; Lee, J. A.; Fox, C. H.; Bao, Z., Skin-like pressure and strain sensors based on transparent elastic films of carbon nanotubes. *Nat Nanotechnol* **2011,** *6*, 788.

68. Rao, R.; Pint, C. L.; Islam, A. E.; Weatherup, R. S.; Hofmann, S.; Meshot, E. R.; Wu, F.; Zhou, C.; Dee, N.; Amama, P. B.; Carpena-Nuñez, J.; Shi, W.; Plata, D. L.; Penev, E. S.; Yakobson, B. I.; Balbuena, P. B.; Bichara, C.; Futaba, D. N.; Noda, S.; Shin, H.; Kim, K. S.; Simard, B.; Mirri, F.; Pasquali, M.; Fornasiero, F.; Kauppinen, E. I.; Arnold, M.; Cola, B. A.; Nikolaev, P.; Arepalli, S.; Cheng, H.-M.; Zakharov, D. N.; Stach, E. A.; Zhang, J.; Wei, F.; Terrones, M.; Geohegan, D. B.; Maruyama, B.; Maruyama, S.; Li, Y.; Adams, W. W.; Hart, A. J., Carbon Nanotubes and Related Nanomaterials: Critical Advances and Challenges for Synthesis toward Mainstream Commercial Applications. *Acs Nano* **2018,** *12* (12), 11756-11784.

69. Avouris, P.; Appenzeller, J.; Martel, R.; Wind, S. J., Carbon nanotube electronics. *Proceedings of the IEEE* **2003,** *91* (11), 1772-1784.

70. Qiu, C.; Zhang, Z.; Xiao, M.; Yang, Y.; Zhong, D.; Peng, L.-M., Scaling carbon nanotube complementary transistors to 5-nm gate lengths. *Science* **2017,** *355* (6322), 271.

71. Rao, S. G.; Huang, L.; Setyawan, W.; Hong, S., Large-scale assembly of carbon nanotubes. *Nature* **2003,** *425*, 36.

72. Avouris, P., Molecular Electronics with Carbon Nanotubes. *Accounts of Chemical Research* **2002,** *35* (12), 1026-1034.

73. Geim, A. K.; Novoselov, K. S., The rise of graphene. *Nature Materials* **2007,** *6*, 183.

74. Weisman, R. B.; Bachilo, S. M., Dependence of Optical Transition Energies on Structure for Single-Walled Carbon Nanotubes in Aqueous Suspension: An Empirical Kataura Plot. *Nano Lett* **2003,** *3* (9), 1235-1238.

75. Hamada, N.; Sawada, S.-i.; Oshiyama, A., New one-dimensional conductors: Graphitic microtubules. *Phys Rev Lett* **1992,** *68* (10), 1579-1581.

76. Zhao, Y.; Clar, J. G.; Li, L. P.; Xu, J.; Yuan, T. Y.; Bonzongo, J. C. J.; Ziegler, K. J., Selective desorption of high-purity (6,5) SWCNTs from hydrogels through surfactant modulation. *Chem Commun* **2016,** *52* (14), 2928-2931.

77. Arnold, M. S.; Green, A. A.; Hulvat, J. F.; Stupp, S. I.; Hersam, M. C., Sorting carbon nanotubes by electronic structure using density differentiation. *Nat Nanotechnol* **2006,** *1*, 60.

78. Ihara, K.; Endoh, H.; Saito, T.; Nihey, F., Separation of Metallic and Semiconducting Single-Wall Carbon Nanotube Solution by Vertical Electric Field. *The Journal of Physical Chemistry C* **2011,** *115* (46), 22827-22832.

79. Liu, H.; Nishide, D.; Tanaka, T.; Kataura, H., Large-scale single-chirality separation of single-wall carbon nanotubes by simple gel chromatography. *Nature Communications* **2011,** *2*, 309.

80. Bradley, K.; Gabriel, J.-C. P.; Grüner, G., Flexible Nanotube Electronics. *Nano Letters* **2003,** *3* (10), 1353-1355.

81. Tang, J.; Cao, Q.; Tulevski, G.; Jenkins, K. A.; Nela, L.; Farmer, D. B.; Han, S.-J., Flexible CMOS integrated circuits based on carbon nanotubes with sub-10 ns stage delays. *Nature Electronics* **2018,** *1* (3), 191-196.

82. Yao, Z.; Kane, C. L.; Dekker, C., High-Field Electrical Transport in Single-Wall Carbon Nanotubes. *Phys Rev Lett* **2000,** *84* (13), 2941-2944.

83. Zaumseil, J., Single-walled carbon nanotube networks for flexible and printed electronics. *Semicond Sci Tech* **2015,** *30* (7).

84. Cao, Q.; Tersoff, J.; Farmer, D. B.; Zhu, Y.; Han, S.-J., Carbon nanotube transistors scaled to a 40-nanometer footprint. *Science* **2017,** *356* (6345), 1369.

85. Kong, J.; Franklin, N. R.; Zhou, C.; Chapline, M. G.; Peng, S.; Cho, K.; Dai, H., Nanotube Molecular Wires as Chemical Sensors. *Science* **2000,** *287* (5453), 622.

86. Liu, L.; Ding, L.; Zhong, D.; Han, J.; Wang, S.; Meng, Q.; Qiu, C.; Zhang, X.; Peng, L.-M.; Zhang, Z., Carbon Nanotube Complementary Gigahertz Integrated Circuits and Their Applications on Wireless Sensor Interface Systems. *Acs Nano* **2019,** *13* (2), 2526-2535.

87. Zhang, H.; Xiang, L.; Yang, Y.; Xiao, M.; Han, J.; Ding, L.; Zhang, Z.; Hu, Y.; Peng, L.-M., High-Performance Carbon Nanotube Complementary Electronics and Integrated Sensor Systems on Ultrathin Plastic Foil. *Acs Nano* **2018,** *12* (3), 2773-2779.

88. Snow, E. S.; Novak, J. P.; Campbell, P. M.; Park, D., Random networks of carbon nanotubes as an electronic material. *Appl Phys Lett* **2003,** *82* (13), 2145-2147.

89. Kocabas, C.; Hur, S.-H.; Gaur, A.; Meitl, M. A.; Shim, M.; Rogers, J. A., Guided Growth of Large-Scale, Horizontally Aligned Arrays of Single-Walled Carbon Nanotubes and Their Use in Thin-Film Transistors. *Small* **2005,** *1* (11), 1110-1116.

90. Zhao, C.; Zhong, D.; Han, J.; Liu, L.; Zhang, Z.; Peng, L.-M., Exploring the Performance Limit of Carbon Nanotube Network Film Field-Effect Transistors for Digital Integrated Circuit Applications. *Advanced Functional Materials* **2019,** *0* (0), 1808574.

91. Menon, H.; Aiswarya, R.; Surendran, K. P., Screen printable MWCNT inks for printed electronics. *RSC Advances* **2017,** *7* (70), 44076-44081.

92. Noyce, S. G.; Doherty, J. L.; Cheng, Z.; Han, H.; Bowen, S.; Franklin, A. D., Electronic Stability of Carbon Nanotube Transistors Under Long-Term Bias Stress. *Nano Letters* **2019**.

93. Avery, A. D.; Zhou, B. H.; Lee, J.; Lee, E. S.; Miller, E. M.; Ihly, R.; Wesenberg, D.; Mistry, K. S.; Guillot, S. L.; Zink, B. L.; Kim, Y. H.; Blackburn, J. L.; Ferguson, A. J., Tailored semiconducting carbon nanotube networks with enhanced thermoelectric properties. *Nat Energy* **2016,** *1*.

94. Javey, A.; Guo, J.; Farmer, D. B.; Wang, Q.; Wang, D.; Gordon, R. G.; Lundstrom, M.; Dai, H., Carbon Nanotube Field-Effect Transistors with Integrated Ohmic Contacts and High-κ Gate Dielectrics. *Nano Letters* **2004,** *4* (3), 447-450.

95. Cao, Y.; Che, Y.; Seo, J.-W. T.; Gui, H.; Hersam, M. C.; Zhou, C., High-performance radio frequency transistors based on diameter-separated semiconducting carbon nanotubes. *Applied Physics Letters* **2016,** *108* (23), 233105.

96. Zhang, D. H.; Ryu, K.; Liu, X. L.; Polikarpov, E.; Ly, J.; Tompson, M. E.; Zhou, C. W., Transparent, conductive, and flexible carbon nanotube films and their application in organic light-emitting diodes. *Nano Lett* **2006,** *6* (9), 1880-1886.

97. Guillot, S. L.; Mistry, K. S.; Avery, A. D.; Richard, J.; Dowgiallo, A.-M.; Ndione, P. F.; van de Lagemaat, J.; Reese, M. O.; Blackburn, J. L., Precision printing and optical modeling of ultrathin SWCNT/C60 heterojunction solar cells. *Nanoscale* **2015,** *7* (15), 6556-6566.

98. Green, A. A.; Hersam, M. C., Colored Semitransparent Conductive Coatings Consisting of Monodisperse Metallic Single-Walled Carbon Nanotubes. *Nano Letters* **2008,** *8* (5), 1417-1422.

99. Miyata, Y.; Yanagi, K.; Maniwa, Y.; Kataura, H., Highly stabilized conductivity of metallic single wall carbon nanotube thin films. *J Phys Chem C* **2008,** *112* (10), 3591-3596.

100. Schindler, A.; Brill, J.; Fruehauf, N.; Novak, J. P.; Yaniv, Z., Solution-deposited carbon nanotube layers for flexible display applications. *Physica E: Low-dimensional Systems and Nanostructures* **2007,** *37* (1), 119-123.

101. Kocabas, C.; Kim, H.-s.; Banks, T.; Rogers, J. A.; Pesetski, A. A.; Baumgardner, J. E.; Krishnaswamy, S. V.; Zhang, H., Radio frequency analog electronics based on

carbon nanotube transistors. *Proceedings of the National Academy of Sciences* **2008,** *105* (5), 1405.

102. Corr, S. J.; Raoof, M.; Cisneros, B. T.; Orbaek, A. W.; Cheney, M. A.; Law, J. J.; Lara, N. C.; Barron, A. R.; Wilson, L. J.; Curley, S. A., Radiofrequency electric-field heating behaviors of highly enriched semiconducting and metallic single-walled carbon nanotubes. *Nano Res* **2015,** *8* (9), 2859-2870.

103. Anas, M.; Zhao, Y.; Saed, M. A.; Ziegler, K. J.; Green, M. J., Radio frequency heating of metallic and semiconducting single-walled carbon nanotubes. *Nanoscale* **2019,** *11* (19), 9617-9625.

104. Bachilo, S. M.; Strano, M. S.; Kittrell, C.; Hauge, R. H.; Smalley, R. E.; Weisman, R. B., Structure-Assigned Optical Spectra of Single-Walled Carbon Nanotubes. *Science* **2002,** *298* (5602), 2361.

105. Clar, J. G.; Yuan, T.; Zhao, Y.; Bonzongo, J.-C. J.; Ziegler, K. J., Evaluation of Critical Parameters in the Separation of Single-Wall Carbon Nanotubes through Selective Adsorption onto Hydrogels. *The Journal of Physical Chemistry C* **2014,** *118* (28), 15495-15505.

106. Silvera-Batista, C. A.; Scott, D. C.; McLeod, S. M.; Ziegler, K. J., A Mechanistic Study of the Selective Retention of SDS-Suspended Single-Wall Carbon Nanotubes on Agarose Gels. *The Journal of Physical Chemistry C* **2011,** *115* (19), 9361-9369.

107. Tenent, R. C.; Barnes, T. M.; Bergeson, J. D.; Ferguson, A. J.; To, B.; Gedvilas, L. M.; Heben, M. J.; Blackburn, J. L., Ultrasmooth, Large-Area, High-Uniformity,

Conductive Transparent Single-Walled-Carbon-Nanotube Films for Photovoltaics Produced by Ultrasonic Spraying. *Adv Mater* **2009,** *21* (31), 3210-+.

108. Okimoto, H.; Takenobu, T.; Yanagi, K.; Miyata, Y.; Shimotani, H.; Kataura, H.; Iwasa, Y., Tunable Carbon Nanotube Thin-Film Transistors Produced Exclusively via Inkjet Printing. *Adv Mater* **2010,** *22* (36), 3981-3986.

109. Subbaraman, H.; Pham, D. T.; Xu, X.; Chen, M. Y.; Hosseini, A.; Lu, X.; Chen, R. T., Inkjet-Printed Two-Dimensional Phased-Array Antenna on a Flexible Substrate. *IEEE Antennas and Wireless Propagation Letters* **2013,** *12,* 170-173.

110. Cao, X.; Chen, H.; Gu, X.; Liu, B.; Wang, W.; Cao, Y.; Wu, F.; Zhou, C., Screen Printing as a Scalable and Low-Cost Approach for Rigid and Flexible Thin-Film Transistors Using Separated Carbon Nanotubes. *Acs Nano* **2014,** *8* (12), 12769-12776.

111. Shi, Y. S.; Zhu, C.-C.; Qikun, W.; Xin, L., Large area screen-printing cathode of CNT for FED. *Diamond and Related Materials* **2003,** *12* (9), 1449-1452.

112. Lee, W.; Koo, H.; Sun, J.; Noh, J.; Kwon, K.-S.; Yeom, C.; Choi, Y.; Chen, K.; Javey, A.; Cho, G., A fully roll-to-roll gravure-printed carbon nanotube-based active matrix for multi-touch sensors. *Sci Rep-Uk* **2015,** *5*, 17707.

113. Fischer, T.; Rühling, J.; Wetzold, N.; Zillger, T.; Weissbach, T.; Göschel, T.; Würfel, M.; Hübler, A.; Kroll, L., Roll-to-roll printed carbon nanotubes on textile substrates as a heating layer in fiber-reinforced epoxy composites. *Journal of Applied Polymer Science* **2018,** *135* (10), 45950.

114. Zhou, B.; Li, Y.; Zheng, G.; Dai, K.; Liu, C.; Ma, Y.; Zhang, J.; Wang, N.; Shen, C.; Guo, Z., Continuously fabricated transparent conductive polycarbonate/carbon nanotube nanocomposite films for switchable thermochromic applications. *Journal of Materials Chemistry C* **2018,** *6* (31), 8360-8371.

115. Che, J.; Chen, P.; Chan-Park, M. B., High-strength carbon nanotube buckypaper composites as applied to free-standing electrodes for supercapacitors. *Journal of Materials Chemistry A* **2013,** *1* (12), 4057-4066.

116. Jin Gyu, P.; Jeffrey, L.; Qunfeng, C.; Jianwen, B.; Jesse, S.; Richard, L.; Ben, W.; Chuck, Z.; James, S. B.; Leslie, K.; Percy, F.; David, D., Electromagnetic interference shielding properties of carbon nanotube buckypaper composites. *Nanotechnology* **2009,** *20* (41), 415702.

117. Du, F.; Scogna, R. C.; Zhou, W.; Brand, S.; Fischer, J. E.; Winey, K. I., Nanotube Networks in Polymer Nanocomposites: Rheology and Electrical Conductivity. *Macromolecules* **2004,** *37* (24), 9048-9055.

118. Mehdizadeh, M., *Microwave/RF Applicators and Probes for Material Heating, Sensing, and Plasma Generation*. William Andrew: 2009.

119. Electrical Conductivity Basics. https://radio-electronics.com/info//formulae/resistance/electrical-conductivity.php.

120. Sun, J.; Wang, W.; Yue, Q., Review on Microwave-Matter Interaction Fundamentals and Efficient Microwave-Associated Heating Strategies. *Materials (Basel, Switzerland)* **2016,** *9* (4), 231.

121. Yoshikawa, N., Fundamentals and Applications of Microwave Heating of Metals. *Journal of Microwave Power and Electromagnetic Energy* **2010,** *44* (1), 4-13.

122. Rybakov, K. I.; Semenov, V. E.; Egorov, S. V.; Eremeev, A. G.; Plotnikov, I. V.; Bykov, Y. V., Microwave heating of conductive powder materials. *J Appl Phys* **2006,** *99* (2), 023506.

123. Cheng, C.; Fan, R.; Ren, Y.; Ding, T.; Qian, L.; Guo, J.; Li, X.; An, L.; Lei, Y.; Yin, Y.; Guo, Z., Radio frequency negative permittivity in random carbon nanotubes/alumina nanocomposites. *Nanoscale* **2017,** *9* (18), 5779-5787.

124. Zeng, X.; Yang, D.; Liu, H.; Zhou, N.; Wang, Y.; Zhou, W.; Xie, S.; Kataura, H., Detecting and Tuning the Interactions between Surfactants and Carbon Nanotubes for Their High-Efficiency Structure Separation. *Advanced Materials Interfaces* **2018,** *5* (2), 1700727.

125. Bekyarova, E.; Itkis, M. E.; Cabrera, N.; Zhao, B.; Yu, A. P.; Gao, J. B.; Haddon, R. C., Electronic properties of single-walled carbon nanotube networks. *J Am Chem Soc* **2005,** *127* (16), 5990-5995.

126. Sillars, R. W., The properties of a dielectric containing semiconducting particles of various shapes. *Institution of Electrical Engineers - Proceedings of the Wireless Section of the Institution* **1937,** *12* (35), 139-155.

127. Hu, C.; Li, Z.; Wang, Y.; Gao, J.; Dai, K.; Zheng, G.; Liu, C.; Shen, C.; Song, H.; Guo, Z., Comparative assessment of the strain-sensing behaviors of polylactic acid

nanocomposites: reduced graphene oxide or carbon nanotubes. *J Mater Chem C* **2017,** *5* (9), 2318-2328.

128. Islam, S.; Li, Z.; Dorgan, V. E.; Bae, M.; Pop, E., Role of Joule Heating on Current Saturation and Transient Behavior of Graphene Transistors. *Ieee Electr Device L* **2013,** *34* (2), 166-168.

129. Xing, C.; Yin, W.; Liu, L.; Huang, J., Investigation on Self-Heating Effect in Carbon Nanotube Field-Effect Transistors. *Ieee T Electron Dev* **2011,** *58* (2), 523-529.

130. Rutherglen, C.; Jain, D.; Burke, P., Nanotube electronics for radiofrequency applications. *Nat Nanotechnol* **2009,** *4* (12), 811-819.

131. Jensen, K.; Weldon, J.; Garcia, H.; Zettl, A., Nanotube Radio. *Nano Lett* **2007,** *7* (11), 3508-3511.

132. Shoucair, F. S., Potential and problems of high-temperature electronics and CMOS integrated circuits (25–250°C) - an overview. *Microelectronics Journal* **1991,** *22* (2), 39-54.

133. Schroder, D. K.; Babcock, J. A., Negative bias temperature instability: Road to cross in deep submicron silicon semiconductor manufacturing. *J Appl Phys* **2003,** *94* (1), 1-18.

134. Mehdizadeh, M., *Microwave/RF Applicators and Probes for Material Heating, Sensing, and Plasma Generation*. William Andrew Publishing: 2015; p 35.

135. Patil, N.; Camacho, A. C.; Mishra, N. K.; Singhla, P.; Sweeney, C. B.; Saed, M. A.; Radovic, M.; Green, M. J., Radio Frequency and Microwave Heating of Preceramic

Polymer Nanocomposites with Applications in Mold-Free Processing. *Adv. Eng. Mater.* **2019,** *21*, 1900276.

136. Moran, C. H.; Wainerdi, S. M.; Cherukuri, T. K.; Kittrell, C.; Wiley, B. J.; Nicholas, N. W.; Curley, S. A.; Kanzius, J. S.; Cherukuri, P., Size-dependent joule heating of gold nanoparticles using capacitively coupled radiofrequency fields. *Nano Res* **2009,** *2* (5), 400-405.

137. Sun, J.; Wang, W.; Yue, Q., Review on Microwave-Matter Interaction Fundamentals and Efficient Microwave-Associated Heating Strategies. *Materials* **2016,** *9* (4).

138. Hicks, V. K.; Anas, M.; Porter, E. B.; Green, M. J., High-throughput screening of printed carbon nanotube circuits using radio frequency heating. *Carbon* **2019,** *152*, 444-450.

139. Habib, T. P. N.; Zhao, X.; Prehn, E.; Lutkenhaus, J.; Miladin, R.; Green, M. J., Heating of Ti3C2Tx MXene/polymer composites in response to radio frequency fields. *Sci. Rep.* **2019**.

140. Nassr, A. A.; Ahmed, W. H.; El-Dakhakhni, W. W., Coplanar capacitance sensors for detecting water intrusion in composite structures. *Measurement Science and Technology* **2008,** *19* (7), 075702.

141. Anas, M.; Mustafa, M. M.; Vashisth, A.; Barnes, E.; Saed, M. A.; Moores, L. C.; Green, M. J., Universal patterns of radio-frequency heating in nanomaterial-loaded structures. *Applied Materials Today* **2021,** *23*, 101044.

142. He, Z.; Satarkar, N.; Xie, T.; Cheng, Y.-T.; Hilt, J. Z., Remote Controlled Multishape Polymer Nanocomposites with Selective Radiofrequency Actuations. *Adv Mater* **2011,** *23* (28), 3192-3196.

143. Kayser, T.; Pauli, M.; Wiesbeck, W., Design of a Microwave Applicator for Nanoparticle Synthesis. *Journal of Microwave Power and Electromagnetic Energy* **2007,** *42* (2), 21-30.

144. Shi, S.-L.; Zhang, L.-Z.; Li, J.-S., Electrical and dielectric properties of multiwall carbon nanotube/polyaniline composites. *Journal of Polymer Research* **2009,** *16* (4), 395-399.

145. Zhao, X.; Koos, A. A.; Chu, B. T. T.; Johnston, C.; Grobert, N.; Grant, P. S., Spray deposited fluoropolymer/multi-walled carbon nanotube composite films with high dielectric permittivity at low percolation threshold. *Carbon* **2009,** *47* (3), 561-569.

146. Antonets, I. V.; Kotov, L. N.; Nekipelov, S. V.; Karpushov, E. N., Conducting and reflecting properties of thin metal films. *Technical Physics* **2004,** *49* (11), 1496-1500.

147. Baughman, R. H.; Zakhidov, A. A.; de Heer, W. A., Carbon Nanotubes--the Route Toward Applications. *Science* **2002,** *297* (5582), 787.

148. Chen, K.; Gao, W.; Emaminejad, S.; Kiriya, D.; Ota, H.; Nyein, H. Y. Y.; Takei, K.; Javey, A., Printed Carbon Nanotube Electronics and Sensor Systems. *Adv Mater* **2016,** *28* (22), 4397-4414.

149. Rowell, M. W.; Topinka, M. A.; McGehee, M. D.; Prall, H.-J.; Dennler, G.; Sariciftci, N. S.; Hu, L.; Gruner, G., Organic solar cells with carbon nanotube network electrodes. *Appl Phys Lett* **2006,** *88* (23), 233506.

150. Lee, W. J.; Ramasamy, E.; Lee, D. Y.; Song, J. S., Efficient Dye-Sensitized Solar Cells with Catalytic Multiwall Carbon Nanotube Counter Electrodes. *ACS Applied Materials & Interfaces* **2009,** *1* (6), 1145-1149.

151. Wang, T.; Guo, Y.; Wan, P.; Zhang, H.; Chen, X.; Sun, X., Flexible Transparent Electronic Gas Sensors. *Small* **2016,** *12* (28), 3748-3756.

152. Lau, P. H.; Takei, K.; Wang, C.; Ju, Y.; Kim, J.; Yu, Z.; Takahashi, T.; Cho, G.; Javey, A., Fully Printed, High Performance Carbon Nanotube Thin-Film Transistors on Flexible Substrates. *Nano Lett* **2013,** *13* (8), 3864-3869.

153. Wallace, G. G.; Chen, J.; Li, D.; Moulton, S. E.; Razal, J. M., Nanostructured carbon electrodes. *Journal of Materials Chemistry* **2010,** *20* (18), 3553-3562.

154. Hecht, D. S.; Hu, L.; Irvin, G., Emerging Transparent Electrodes Based on Thin Films of Carbon Nanotubes, Graphene, and Metallic Nanostructures. *Adv Mater* **2011,** *23* (13), 1482-1513.

155. Fennimore, A. M.; Cheng, L. T.; Roach, D. H., A stable under-gate triode CNT field emitter fabricated via screen printing. *Diamond and Related Materials* **2008,** *17* (12), 2005-2009.

156. Higuchi, K.; Kishimoto, S.; Nakajima, Y.; Tomura, T.; Takesue, M.; Hata, K.; Kauppinen, E. I.; Ohno, Y., High-Mobility, Flexible Carbon Nanotube Thin-Film

Transistors Fabricated by Transfer and High-Speed Flexographic Printing Techniques. *Applied Physics Express* **2013,** *6* (8), 085101.

157. Ha, M.; Xia, Y.; Green, A. A.; Zhang, W.; Renn, M. J.; Kim, C. H.; Hersam, M. C.; Frisbie, C. D., Printed, Sub-3V Digital Circuits on Plastic from Aqueous Carbon Nanotube Inks. *ACS Nano* **2010,** *4* (8), 4388-4395.

158. Li, M.-Y.; Yang, M.; Vargas, E.; Neff, K.; Vanli, A.; Liang, R., Analysis of variance on thickness and electrical conductivity measurements of carbon nanotube thin films. *Measurement Science and Technology* **2016,** *27* (9), 095004.

159. Sharma, P.; Ahuja, P., Recent advances in carbon nanotube-based electronics. *Materials Research Bulletin* **2008,** *43* (10), 2517-2526.

160. Paton, K. R.; Windle, A. H., Efficient microwave energy absorption by carbon nanotubes. *Carbon* **2008,** *46* (14), 1935-1941.

161. Kim, T.; Lee, J.; 이건홍, Microwave Heating of Carbon-Based Solid Materials. *Carbon Letters* **2014,** *15* (1), 15-24.

162. Irin, F.; Shrestha, B.; Canas, J. E.; Saed, M. A.; Green, M. J., Detection of carbon nanotubes in biological samples through microwave-induced heating. *Carbon* **2012,** *50* (12), 4441-4449.

163. Odom, M. G. B.; Sweeney, C. B.; Parviz, D.; Sill, L. P.; Saed, M. A.; Green, M. J., Rapid curing and additive manufacturing of thermoset systems using scanning microwave heating of carbon nanotube/epoxy composites. *Carbon* **2017,** *120*, 447-453.

164. Liu, H.; Takagi, D.; Chiashi, S.; Homma, Y., Transfer and Alignment of Random Single-Walled Carbon Nanotube Films by Contact Printing. *ACS Nano* **2010,** *4* (2), 933-938.

165. Qiu, S.; Wu, K.; Gao, B.; Li, L.; Jin, H.; Li, Q., Solution-Processing of High-Purity Semiconducting Single-Walled Carbon Nanotubes for Electronics Devices. *Adv Mater* **2019,** *31* (9), 1800750.

166. Kamali-Sarvestani, R.; Martin, B.; Brayden, L. In *Design and Fabrication of Ink-Jet Printed Logic Gates using SWCNT-FET for Flexible Circuit Applications*, 2019 IEEE International Symposium on Circuits and Systems (ISCAS), 26-29 May 2019; 2019; pp 1-5.

167. Dinh, T.; Phan, H.-P.; Qamar, A.; Nguyen, N.-T.; Dao, D. V., Flexible and multifunctional electronics fabricated by a solvent-free and user-friendly method. *RSC Advances* **2016,** *6* (81), 77267-77274.

168. Janas, D.; Koziol, K. K., Rapid electrothermal response of high-temperature carbon nanotube film heaters. *Carbon* **2013,** *59*, 457-463.

169. Idris, M. K.; Qiu, J.; Melenka, G. W.; Grau, G., Printing electronics directly onto carbon fiber composites: unmanned aerial vehicle (UAV) wings with integrated heater for de-icing. *Engineering Research Express* **2020,** *2* (2), 025022.

170. Wang, C.-P.; Hsiao, M.-H.; Lee, G.-H.; Chang, T.-L.; Lee, Y.-W., The investigation of electrothermal response and reliability of flexible graphene micro-heaters. *Microelectronic Engineering* **2020,** *228*, 111334.

171. Chen, X.; Gao, H.; Hai, G.; Jia, D.; Xing, L.; Chen, S.; Cheng, P.; Han, M.; Dong, W.; Wang, G., Carbon nanotube bundles assembled flexible hierarchical framework based phase change material composites for thermal energy harvesting and thermotherapy. *Energy Storage Materials* **2020,** *26*, 129-137.

172. Pan, L.; Liu, Z.; kızıltaş,O.; Zhong, L.; Pang, X.; Wang, F.; Zhu, Y.; Ma, W.; Lv, Y., Carbon fiber/poly ether ether ketone composites modified with graphene for electro-thermal deicing applications. *Composites Science and Technology* **2020,** *192*, 108117.

173. Liu, P.; Liu, L.; Wei, Y.; Liu, K.; Chen, Z.; Jiang, K.; Li, Q.; Fan, S., Fast High-Temperature Response of Carbon Nanotube Film and Its Application as an Incandescent Display. *Adv Mater* **2009,** *21* (35), 3563-3566.

174. Liu, P.; Liu, L.; Jiang, K.; Fan, S., Carbon-Nanotube-Film Microheater on a Polyethylene Terephthalate Substrate and Its Application in Thermochromic Displays. *Small* **2011,** *7* (6), 732-736.

175. Chen, J.; Wang, Y.; Liu, F.; Luo, S., Laser-Induced Graphene Paper Heaters with Multimodally Patternable Electrothermal Performance for Low-Energy Manufacturing of Composites. *ACS Applied Materials & Interfaces* **2020,** *12* (20), 23284-23297.

176. Philip, B.; Jewell, E.; Greenwood, P.; Weirman, C., Material and process optimization screen printing carbon graphite pastes for mass production of heating elements. *Journal of Manufacturing Processes* **2016,** *22*, 185-191.

177. Hao, Y.; Tian, M.; Zhao, H.; Qu, L.; Zhu, S.; Zhang, X.; Chen, S.; Wang, K.; Ran, J., High Efficiency Electrothermal Graphene/Tourmaline Composite Fabric Joule Heater

with Durable Abrasion Resistance via a Spray Coating Route. *Industrial & Engineering Chemistry Research* **2018,** *57* (40), 13437-13448.

178. Anas, M.; Mustafa, M. M.; Carey, D. G.; Sarmah, A.; LeMonte, J. J.; Green, M. J., Joule heating of carbon pixels for on-demand thermal patterning. *Carbon* **2021,** *174*, 518-523.

179. Wang, P.-H.; Chen, S.-P.; Su, C.-H.; Liao, Y.-C., Direct printed silver nanowire thin film patterns for flexible transparent heaters with temperature gradients. *RSC Advances* **2015,** *5* (119), 98412-98418.

180. Todoroki, A.; Ueda, M.; Hirano, Y., Strain and Damage Monitoring of CFRP Laminates by Means of Electrical Resistance Measurement. *Journal of Solid Mechanics and Materials Engineering* **2007,** *1* (8), 947-974.

181. Patil, N.; Mishra, N. K.; Saed, M. A.; Green, M. J.; Wilhite, B. A., Radio Frequency Driven Heating of Catalytic Reactors for Portable Green Chemistry. *Advanced Sustainable Systems* **2020,** *4* (11), 2000095.

182. Dresselhaus, M. S.; Dresselhaus, G.; Jorio, A., UNUSUAL PROPERTIES AND STRUCTURE OF CARBON NANOTUBES. *Annual Review of Materials Research* **2004,** *34* (1), 247-278.

183. Moniruzzaman, M.; Winey, K. I., Polymer Nanocomposites Containing Carbon Nanotubes. *Macromolecules* **2006,** *39* (16), 5194-5205.

184. Dong, M.; Wang, C.; Liu, H.; Liu, C.; Shen, C.; Zhang, J.; Jia, C.; Ding, T.; Guo, Z., Enhanced Solid Particle Erosion Properties of Thermoplastic Polyurethane-Carbon

Nanotube Nanocomposites. *Macromolecular Materials and Engineering* **2019,** *0* (0), 1900010.

185. Rafique, I.; Muhammad, B., Review of Applications of Polymer/Carbon Nanotubes and Epoxy/CNT Composites AU - Kausar, Ayesha. *Polymer-Plastics Technology and Engineering* **2016,** *55* (11), 1167-1191.

186. Müller, K.; Bugnicourt, E.; Latorre, M.; Jorda, M.; Echegoyen Sanz, Y.; Lagaron, M. J.; Miesbauer, O.; Bianchin, A.; Hankin, S.; Bölz, U.; Pérez, G.; Jesdinszki, M.; Lindner, M.; Scheuerer, Z.; Castelló, S.; Schmid, M., Review on the Processing and Properties of Polymer Nanocomposites and Nanocoatings and Their Applications in the Packaging, Automotive and Solar Energy Fields. *Nanomaterials* **2017,** *7* (4), 74.

187. Kingston, C.; Zepp, R.; Andrady, A.; Boverhof, D.; Fehir, R.; Hawkins, D.; Roberts, J.; Sayre, P.; Shelton, B.; Sultan, Y.; Vejins, V.; Wohlleben, W., Release characteristics of selected carbon nanotube polymer composites. *Carbon* **2014,** *68*, 33-57.

188. Kuempel, E. D.; Jaurand, M.-C.; Møller, P.; Morimoto, Y.; Kobayashi, N.; Pinkerton, K. E.; Sargent, L. M.; Vermeulen, R. C. H.; Fubini, B.; Kane, A. B., Evaluating the mechanistic evidence and key data gaps in assessing the potential carcinogenicity of carbon nanotubes and nanofibers in humans. *Critical Reviews in Toxicology* **2017,** *47* (1), 1-58.

189. Kobayashi, N.; Izumi, H.; Morimoto, Y., Review of toxicity studies of carbon nanotubes. *Journal of Occupational Health* **2017,** *59* (5), 394-407.

190. Fukushima, S.; Kasai, T.; Umeda, Y.; Ohnishi, M.; Sasaki, T.; Matsumoto, M., Carcinogenicity of multi-walled carbon nanotubes: challenging issue on hazard assessment. *Journal of Occupational Health* **2018,** *60* (1), 10-30.

191. Petersen, E. J.; Zhang, L.; Mattison, N. T.; O'Carroll, D. M.; Whelton, A. J.; Uddin, N.; Nguyen, T.; Huang, Q.; Henry, T. B.; Holbrook, R. D.; Chen, K. L., Potential Release Pathways, Environmental Fate, And Ecological Risks of Carbon Nanotubes. *Environmental Science & Technology* **2011,** *45* (23), 9837-9856.

192. Nowack, B.; David, R. M.; Fissan, H.; Morris, H.; Shatkin, J. A.; Stintz, M.; Zepp, R.; Brouwer, D., Potential release scenarios for carbon nanotubes used in composites. *Environment International* **2013,** *59*, 1-11.

193. Froggett, S. J.; Clancy, S. F.; Boverhof, D. R.; Canady, R. A., A review and perspective of existing research on the release of nanomaterials from solid nanocomposites. *Particle and Fibre Toxicology* **2014,** *11* (1), 17.

194. Harper, S.; Wohlleben, W.; Doa, M.; Nowack, B.; Clancy, S.; Canady, R.; Maynard, A., Measuring Nanomaterial Release from Carbon Nanotube Composites: Review of the State of the Science. *Journal of Physics: Conference Series* **2015,** *617*, 012026.

195. Ging, J.; Tejerina-Anton, R.; Ramakrishnan, G.; Nielsen, M.; Murphy, K.; Gorham, J. M.; Nguyen, T.; Orlov, A., Development of a conceptual framework for evaluation of nanomaterials release from nanocomposites: Environmental and toxicological implications. *Science of The Total Environment* **2014,** *473-474*, 9-19.

196. Wohlleben, W.; Brill, S.; Meier, M. W.; Mertler, M.; Cox, G.; Hirth, S.; von Vacano, B.; Strauss, V.; Treumann, S.; Wiench, K.; Ma-Hock, L.; Landsiedel, R., On the Lifecycle of Nanocomposites: Comparing Released Fragments and their In-Vivo Hazards from Three Release Mechanisms and Four Nanocomposites. *Small* **2011,** *7* (16), 2384-2395.

197. Göhler, D.; Hillemann, L.; Vorbau, M.; Stintz, M., Characterization of Nanoparticle Release from Surface Coatings by the Simulation of a Sanding Process. *The Annals of Occupational Hygiene* **2010,** *54* (6), 615-624.

198. Schlagenhauf, L.; Chu, B. T. T.; Buha, J.; Nüesch, F.; Wang, J., Release of Carbon Nanotubes from an Epoxy-Based Nanocomposite during an Abrasion Process. *Environmental Science & Technology* **2012,** *46* (13), 7366-7372.

199. Wohlleben, W.; Neubauer, N., Quantitative rates of release from weathered nanocomposites are determined across 5 orders of magnitude by the matrix, modulated by the embedded nanomaterial. *NanoImpact* **2016,** *1*, 39-45.

200. Duncan, T. V.; Pillai, K., Release of Engineered Nanomaterials from Polymer Nanocomposites: Diffusion, Dissolution, and Desorption. *ACS Applied Materials & Interfaces* **2015,** *7* (1), 2-19.

201. Lankone, R. S.; Wang, J.; Ranville, J. F.; Fairbrother, D. H., Photodegradation of polymer-CNT nanocomposites: effect of CNT loading and CNT release characteristics. *Environmental Science: Nano* **2017,** *4* (4), 967-982.

202. Hirth, S.; Cena, L.; Cox, G.; Tomović Ž; Peters, T.; Wohlleben, W., Scenarios and methods that induce protruding or released CNTs after degradation of nanocomposite materials. *Journal of Nanoparticle Research* **2013,** *15* (4), 1504.

203. Brame, J. A.; Alberts, E. M.; Schubauer-Berigan, M. K.; Dunn, K. H.; Babik, K. R.; Barnes, E.; Moser, R.; Poda, A. R.; Kennedy, A. J., Characterization and workplace exposure assessment of nanomaterial released from a carbon nanotube-enabled anti-corrosive coating. *NanoImpact* **2018,** *12*, 58-68.

204. Koivisto, A. J.; Jensen, A. C. Ø.; Kling, K. I.; Nørgaard, A.; Brinch, A.; Christensen, F.; Jensen, K. A., Quantitative material releases from products and articles containing manufactured nanomaterials: Towards a release library. *NanoImpact* **2017,** *5*, 119-132.

205. Petersen, E. J.; Flores-Cervantes, D. X.; Bucheli, T. D.; Elliott, L. C. C.; Fagan, J. A.; Gogos, A.; Hanna, S.; Kägi, R.; Mansfield, E.; Bustos, A. R. M.; Plata, D. L.; Reipa, V.; Westerhoff, P.; Winchester, M. R., Quantification of Carbon Nanotubes in Environmental Matrices: Current Capabilities, Case Studies, and Future Prospects. *Environmental Science & Technology* **2016,** *50* (9), 4587-4605.

206. Kovochich, M.; Fung, C.-C. D.; Avanasi, R.; Madl, A. K., Review of techniques and studies characterizing the release of carbon nanotubes from nanocomposites: Implications for exposure and human health risk assessment. *Journal Of Exposure Science And Environmental Epidemiology* **2017,** *28*, 203.

207. Wohlleben, W.; Meier, M. W.; Vogel, S.; Landsiedel, R.; Cox, G.; Hirth, S.; Tomović Ž, Elastic CNT–polyurethane nanocomposite: synthesis, performance and assessment of fragments released during use. *Nanoscale* **2013,** *5* (1), 369-380.

208. Schlagenhauf, L.; Buerki-Thurnherr, T.; Kuo, Y.-Y.; Wichser, A.; Nüesch, F.; Wick, P.; Wang, J., Carbon Nanotubes Released from an Epoxy-Based Nanocomposite: Quantification and Particle Toxicity. *Environmental Science & Technology* **2015,** *49* (17), 10616-10623.

209. Li, Z. F.; Luo, G. H.; Zhou, W. P.; Wei, F.; Xiang, R.; Liu, Y. P., The quantitative characterization of the concentration and dispersion of multi-walled carbon nanotubes in suspension by spectrophotometry. *Nanotechnology* **2006,** *17* (15), 3692-3698.

210. Attal, S.; Thiruvengadathan, R.; Regev, O., Determination of the Concentration of Single-Walled Carbon Nanotubes in Aqueous Dispersions Using UV−Visible Absorption Spectroscopy. *Analytical Chemistry* **2006,** *78* (23), 8098-8104.

211. Das, K. K.; Nava, V.; Chang, C.-W.; Chan, J. W.; Xing, B.; Yang, Y., Emerging investigator series: quantification of multiwall carbon nanotubes in plant tissues with spectroscopic analysis. *Environmental Science: Nano* **2019,** *6* (2), 380-387.

212. Li, R.; Wang, X.; Ji, Z.; Sun, B.; Zhang, H.; Chang, C. H.; Lin, S.; Meng, H.; Liao, Y.-P.; Wang, M.; Li, Z.; Hwang, A. A.; Song, T.-B.; Xu, R.; Yang, Y.; Zink, J. I.; Nel, A. E.; Xia, T., Surface Charge and Cellular Processing of Covalently Functionalized Multiwall Carbon Nanotubes Determine Pulmonary Toxicity. *Acs Nano* **2013,** *7* (3), 2352-2368.

213. Kennedy, A. J.; Hull, M. S.; Steevens, J. A.; Dontsova, K. M.; Chappell, M. A.; Gunter, J. C.; Weiss, J. C. A., Factors influencing the partitioning and toxicity of nanotubes in the aquatic environment. *Environmental Toxicology and Chemistry* **2008,** *27* (9), 1932-1941.

214. Kennedy, A. J.; Gunter, J. C.; Chappell, M. A.; Goss, J. D.; Hull, M. S.; Kirgan, R. A.; Steevens, J. A., Influence of nanotube preparation in Aquatic Bioassays. *Environmental Toxicology and Chemistry* **2009,** *28* (9), 1930-1938.

215. Stanley, J. K.; Laird, J. G.; Kennedy, A. J.; Steevens, J. A., Sublethal effects of multiwalled carbon nanotube exposure in the invertebrate Daphnia magna. *Environmental Toxicology and Chemistry* **2016,** *35* (1), 200-204.

216. Wohlleben, W.; Kingston, C.; Carter, J.; Sahle-Demessie, E.; Vázquez-Campos, S.; Acrey, B.; Chen, C.-Y.; Walton, E.; Egenolf, H.; Müller, P.; Zepp, R., NanoRelease: Pilot interlaboratory comparison of a weathering protocol applied to resilient and labile polymers with and without embedded carbon nanotubes. *Carbon* **2017,** *113*, 346-360.

217. Anas, M.; Porter, E. B.; Kennedy, A. J.; Alberts, E. M.; Green, M. J., Detection and quantification of free carbon nanotubes in abraded polymer nanocomposites using UV–vis spectroscopy. *NanoImpact* **2019,** *16*, 100190.

218. Duan, W. H.; Wang, Q.; Collins, F., Dispersion of carbon nanotubes with SDS surfactants: a study from a binding energy perspective. *Chemical Science* **2011,** *2* (7), 1407-1413.

219. Sun, Z.; Nicolosi, V.; Rickard, D.; Bergin, S. D.; Aherne, D.; Coleman, J. N., Quantitative Evaluation of Surfactant-stabilized Single-walled Carbon Nanotubes: Dispersion Quality and Its Correlation with Zeta Potential. *The Journal of Physical Chemistry C* **2008,** *112* (29), 10692-10699.

220. Hertel, T.; Hagen, A.; Talalaev, V.; Arnold, K.; Hennrich, F.; Kappes, M.; Rosenthal, S.; McBride, J.; Ulbricht, H.; Flahaut, E., Spectroscopy of Single- and Double-Wall Carbon Nanotubes in Different Environments. *Nano Letters* **2005,** *5* (3), 511-514.

221. Blanch, A. J.; Lenehan, C. E.; Quinton, J. S., Optimizing Surfactant Concentrations for Dispersion of Single-Walled Carbon Nanotubes in Aqueous Solution. *The Journal of Physical Chemistry B* **2010,** *114* (30), 9805-9811.

222. Wang, L.; Yang, X.; Wang, Q.; Zeng, Y.; Ding, L.; Jiang, W., Effects of ionic strength and temperature on the aggregation and deposition of multi-walled carbon nanotubes. *Journal of Environmental Sciences* **2017,** *51*, 248-255.

223. Liebscher, M.; Fuge, R.; Schröfl, C.; Lange, A.; Caspari, A.; Bellmann, C.; Mechtcherine, V.; Plank, J.; Leonhardt, A., Temperature- and pH-Dependent Dispersion of Highly Purified Multiwalled Carbon Nanotubes Using Polycarboxylate-Based Surfactants in Aqueous Suspension. *The Journal of Physical Chemistry C* **2017,** *121* (31), 16903-16910.

224. Collier, Z. A.; Kennedy, A. J.; Poda, A. R.; Cuddy, M. F.; Moser, R. D.; MacCuspie, R. I.; Harmon, A.; Plourde, K.; Haines, C. D.; Steevens, J. A., Tiered guidance

for risk-informed environmental health and safety testing of nanotechnologies. *Journal of Nanoparticle Research* **2015,** *17* (3), 155.

225. Golanski, L.; Guiot, A.; Pras, M.; Malarde, M.; Tardif, F., Release-ability of nano fillers from different nanomaterials (toward the acceptability of nanoproduct). *Journal of Nanoparticle Research* **2012,** *14* (7), 962.

226. Huang, G.; Park, J. H.; Cena, L. G.; Shelton, B. L.; Peters, T. M., Evaluation of airborne particle emissions from commercial products containing carbon nanotubes. *Journal of Nanoparticle Research* **2012,** *14* (11), 1231.

227. Meng, L.; Soucek, M. D., Comparison of the carbon additives on the conductivity, thermomechanical, and corrosion properties for TEOS oligomer modified epoxy-amine coating systems. *Progress in Organic Coatings* **2019,** *130*, 168-181.

228. Pal, S.; Chatterjee, T.; Manoharan, P.; Naskar, K., Polymer-Carbon Composites as Anti-corrosive Materials. In *Carbon-Containing Polymer Composites*, Rahaman, M.; Khastgir, D.; Aldalbahi, A. K., Eds. Springer Singapore: Singapore, 2019; pp 545-574.

229. Long, C. J.; Orloff, N. D.; Twedt, K. A.; Lam, T.; Vargas-Lara, F.; Zhao, M.; Natarajan, B.; Scott, K. C.; Marksz, E.; Nguyen, T.; Douglas, J. F.; McClelland, J.; Garboczi, E.; Obrzut, J.; Liddle, J. A., Giant Surface Conductivity Enhancement in a Carbon Nanotube Composite by Ultraviolet Light Exposure. *ACS Applied Materials & Interfaces* **2016,** *8* (35), 23230-23235.

230. Nguyen, T.; Petersen, E. J.; Pellegrin, B.; Gorham, J. M.; Lam, T.; Zhao, M.; Sung, L., Impact of UV irradiation on multiwall carbon nanotubes in nanocomposites: Formation

of entangled surface layer and mechanisms of release resistance. *Carbon* **2017,** *116*, 191-200.

231. Schlagenhauf, L.; Kianfar, B.; Buerki-Thurnherr, T.; Kuo, Y.-Y.; Wichser, A.; Nüesch, F.; Wick, P.; Wang, J., Weathering of a carbon nanotube/epoxy nanocomposite under UV light and in water bath: impact on abraded particles. *Nanoscale* **2015,** *7* (44), 18524-18536.

232. Koivisto, A. J.; Bluhme, A. B.; Kling, K. I.; Fonseca, A. S.; Redant, E.; Andrade, F.; Hougaard, K. S.; Krepker, M.; Prinz, O. S.; Segal, E.; Holländer, A.; Jensen, K. A.; Vogel, U.; Koponen, I. K., Occupational exposure during handling and loading of halloysite nanotubes – A case study of counting nanofibers. *NanoImpact* **2018,** *10*, 153-160.

233. Gnanasekaran, K.; Heijmans, T.; van Bennekom, S.; Woldhuis, H.; Wijnia, S.; de With, G.; Friedrich, H., 3D printing of CNT- and graphene-based conductive polymer nanocomposites by fused deposition modeling. *Applied Materials Today* **2017,** *9*, 21-28.

234. Cholleti, E. R.; Gibson, I., ABS Nano Composite Materials in Additive Manufacturing. *IOP Conference Series: Materials Science and Engineering* **2018,** *455*, 012038.

APPENDIX A

DETECTION AND QUANTIFICATION OF FREE CARBON NANOTUBES IN ABRADED POLYMER NANOCOMPOSITES USING UV-VIS SPECTROSCOPY*

Introduction

Carbon nanotubes (CNTs) possess unique mechanical, electrical, thermal, and optical properties which have led to their widespread use as nanofillers in polymer composites.[59, 182-184] Nanocomposites display remarkable enhancement in material properties compared to neat polymers, and can be used in automotive, aerospace, defense, electronics, energy, and sporting-goods industries.[57, 185-187]

However, the increased proliferation of CNT-based products has raised concerns regarding the potential for CNT release due to inhalation and other hazards associated with free CNTs (CNTs that are not bound to any matrix and can be easily dispersed into a surfactant solution).[188-190] It is speculated that CNTs may release from a product during manufacturing, coating removal, consumer use, or in a landfill after end-of-life disposal.[191-195] Many studies have investigated and attempted to characterize the release of free CNTs from a variety of industrially-relevant polymer matrices.[196-202] However, no

* Reprinted with permission from "Detection and quantification of free carbon nanotubes in abraded polymer nanocomposites using UV-vis spectroscopy" by Muhammad Anas; Erin B. Porter; Alan J. Kennedy; Erik M. Alberts; Micah J. Green, 2019. *NanoImpact*, 16, 100190, Copyright 2019 Elsevier Ltd.

studies have been able to conclude with confidence the presence or absence of free CNTs. In particular, proving the negative (i.e., absence of free CNTs) is difficult but extremely important for providing risk assessors with scientific justification for concluding there is a lack of exposure. This difficulty is exasperated by the lack of a standard method to quantify free CNTs that can be readily applied by industries to evaluate their products.[203-204]

The most common technique to detect free CNTs in the debris of nanocomposites is look-and-find microscopy, which is conceptually simple but logistically cumbersome, expensive, time consuming, and not intrinsically quantitative.[205-206] The techniques which are quantitative and frequently employed are analytical ultracentrifugation (AUC)[196, 207] and single-particle inductively-coupled mass spectrometry (sp-ICP-MS);[201, 208] however, these techniques have drawbacks that make them difficult to be accepted as standards. For example, AUC characterizes samples by size only and is unable to differentiate between free CNTs and small solid fragments. Moreover, it is also not very sensitive to detecting low amounts of nanometer-sized fragments in the presence of other solids.[202] The sp-ICP-MS is expensive and measures metal nanoparticles bound to free CNTs, which is then related to the CNT content via a calibration curve.[201] In order for sp-ICP-MS to work effectively, it is necessary to have either initial CNTs with large amounts of metal catalyst residues or CNTs that are pre-labelled with metal ions prior to composite production.[201, 208] Thus, there is a need to explore methods that can quantify free CNTs rapidly and at low cost.

Ultraviolet-visible (UV-vis) spectroscopy is an inexpensive technique that is widely available and can detect CNTs at low concentrations due to strong absorbance of CNTs in the UV-vis spectrum. It is also possible to quantify the CNT content using a relevant calibration.[209-210] Previously, UV-vis spectroscopy has been used to determine uptake of CNTs in plants[211] and biological cells,[212] and concentrations of pristine and functionalized CNTs in aqueous environment.[213-215] Wohlleben *et al.*[216] used UV-vis spectroscopy to assess CNT release from UV-weathered CNT-epoxy and CNT-polyamide composites by measuring the absorbance of CNT. The UV-weathered composite panels were immersed into a leaching fluid (EPA method 1311) and shaken for 24 h at 2 Hz in an incubator to release loose fragments into the fluid. The leaching fluid was then mixed with 1% (v.v.) sodium dodecyl sulfate (SDS) solution and bath sonicated for 1 h prior to UV-vis analysis. Differences observed in absorption coefficients of these solutions relative to the control samples were used as indicators of CNT release. The results from UV-vis analysis correlated with those from the ICP-MS analysis which indicates that UV-Vis spectroscopy is a viable method to quantify CNT release. However, in order to determine free CNT content using UV-vis spectroscopy, it is necessary to separate out these CNTs from the nanocomposite debris which may contain polymer fragments with embedded or protruding CNTs. It is also important that any calibration curve generated to correlate the absorbance of free CNTs to the CNT content in the debris takes into account the presence of polymer matrix in order to accurately quantify free CNTs.

In this work, we develop and demonstrate a rapid and easy protocol to detect and quantify free CNTs using UV-vis spectroscopy. We show a simple procedure to generate calibration curves which takes into account the presence of the polymer matrix. These calibration curves allow quantification of free CNT content with low limits of detection. In order to use this method, we generate debris of various nanocomposites by considering different CNT release scenarios and quantify free CNT content in the debris. We find that sanding of epoxy composites releases significant amount of free CNTs. We also determine that the debris of sandblasted UV-weathered anticorrosive paint and abraded CNT-polylactic acid (PLA) coatings have no free CNTs above the detection limit.

Results and Discussion

Quantification of Free CNTs using UV-vis Spectroscopy

Figure A-1 shows the schematic of the process to analyze nanocomposite debris and quantify its free CNT content using UV-vis spectroscopy. The underlying concept is that if the debris of nanocomposite is mixed with the SDS solution, the SDS will selectively wrap and disperse individual free CNTs but not CNTs that are aggregated, completely embedded in the polymer fragments, or protruding from the polymer fragments. Simple centrifugation can then isolate the dispersed surfactant/CNT colloid, and UV-vis spectroscopy can be used to measure the absorbance of free CNTs in the supernatant, which is then correlated to the total free CNT content in the debris via a calibration curve. It is possible that some free CNT aggregates are also separated out

during the centrifugation process; due to this, the calibration correlates the absorbance of free CNTs in the supernatant with the total free CNT content in the debris.

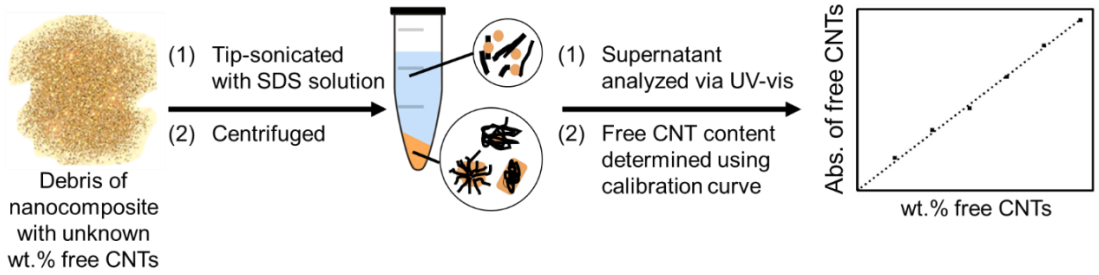

Figure A-1. Schematic of the process to detect and quantify wt.% free CNTs in the debris generated after abrasion of CNT-polymer composites. Reprinted with permission from reference [217], Copyright 2019 Elsevier Ltd.

In order to understand the separation process, it is important to consider different states of CNT-polymer particles that may be present in the debris of nanocomposite and whether or not they will be separated out during the centrifugation step. **Figure A-2** provides schematics of different states of particles that may or may not get dispersed due to the different forces acting on the particles. Many prior studies have already shown that surfactants can wrap and disperse sonicated CNTs,[218-221] and it is also clear that if the CNTs are completely embedded in the polymer matrix, they cannot be dispersed due to inaccessibility of the surfactant molecules. However, the dispersion of particles in other states (bundled or partially embedded CNTs) depends on the balance of forces acting on the suspended particles. If the random Brownian forces are stronger than the gravitational forces, then the particles stay suspended in the dispersion (**Figure A-2 a-d**), whereas if

gravitational forces overcome random Brownian forces, then the particles settle down and are separated out during the centrifugation step (**Figure A-2 e-g**).

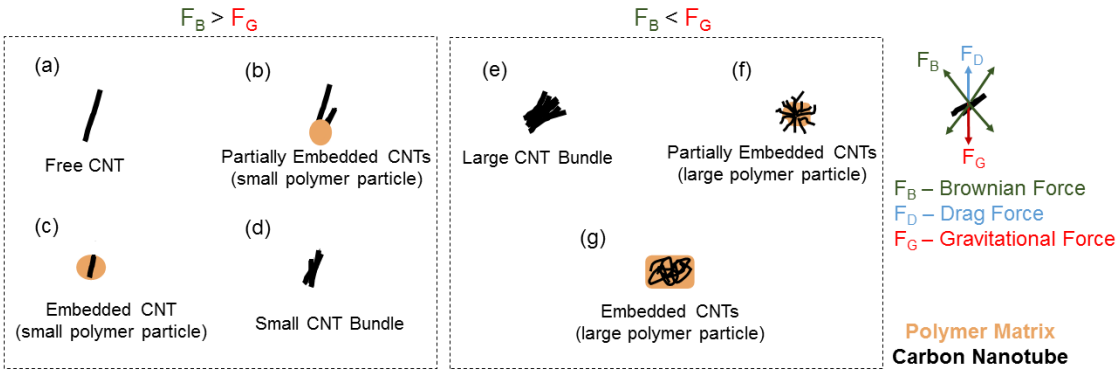

Figure A-2. Schematic of the states of dispersible (left) and non-dispersible (right) particles in the debris of abraded nanocomposite. Reprinted with permission from reference [217], Copyright 2019 Elsevier Ltd.

The calibration curve to quantify free CNT content is generated by adding known amounts of free CNTs to the debris of neat polymer matrix which is then dispersed into the SDS solution using tip-sonication. After centrifugation of dispersions, the UV-vis absorbance spectra of the supernatants are measured and the absorbance of free CNTs at 670 nm is calculated by subtracting out the absorbance of neat polymer debris at 670 nm. The absorbance of free CNTs is then correlated with the total wt.% CNTs to account for free CNT aggregates that are separated out during centrifugation. Based on prior studies, wavelength of 670 nm was used for calibration to avoid interference from other species since most of the polymers also absorb in the lower wavelength range associated with maximum absorbance of CNTs.[211-212, 216] Note that care must be taken in preparing the surfactant-aided dispersion because conditions of low pH and increased ionic strength lead

to agglomeration of CNTs[222-223] which would alter the slope of the calibration curves. This would be particularly important if the debris being analyzed can alter the solution properties.

We used our method to detect free CNTs in the debris of: (1) sanded CNT-epoxy composites; (2) sandblasted UV-weathered CNT-based anti-corrosive paint previously described in Brame *et al*.[203]; and (3) filed CNT-PLA 3D printer filament coatings. This analysis allows for quantitative thresholds of CNT release from different CNT-based products which would be beneficial to industries in terms of compliance to regulations, and for hygienists to be able to estimate exposure.

Free CNT Release from Epoxy Composite

There are several scenarios by which free CNTs can release from a nanocomposite; these include drilling, sawing, sanding, or degradation of polymer matrix by UV-weathering.[196, 198, 224] To represent a relevant release scenario, we used a sanding machine which imposes high mechanical stresses on the CNT-epoxy composites. The debris generated was then analyzed for free CNT content using UV-vis spectroscopy.

A calibration curve was first generated by adding known amounts of free CNTs to debris of neat epoxy and relating absorbance of free CNTs in the supernatant at 670 nm, Abs_{670}, to wt.% free CNTs, C_{CNT}, as shown in **Figure A-3**. A strong linear relationship ($Abs_{670} = 0.467C_{CNT}$, $R^2 = 0.99$) is seen between the absorbance of free CNTs at 670 nm and the total free CNT content in the debris which confirms that the absorbance at 670 nm can be used for quantification of free CNTs [211]. The detection limit (LOD) of free CNTs

in 0.10 g of sanded epoxy debris was calculated to be 1.6 x 10^{-2} wt.% from the calibration curve. Note that the absorbance of free CNTs is determined by subtracting out the absorbance of supernatant of neat epoxy from all samples which results in an intercept of zero.

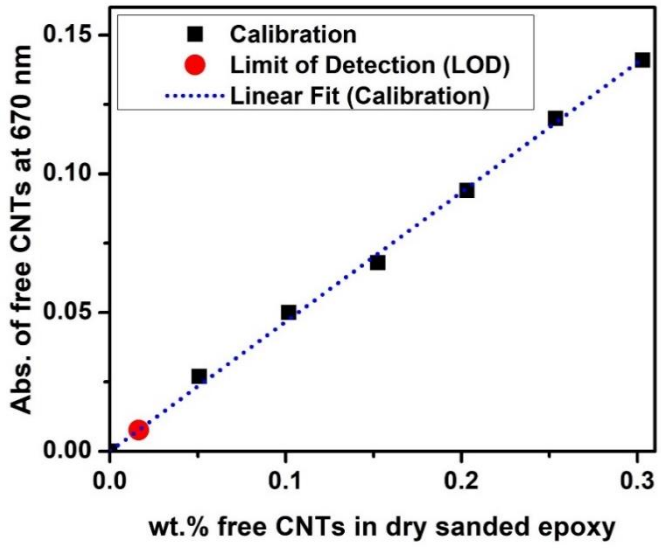

Figure A-3. Calibration curve relating absorbance of free CNTs in the supernatants with total wt.% CNTs added to 0.10 g portions of the debris of sanded epoxy. Reprinted with permission from reference [217], Copyright 2019 Elsevier Ltd.

It is also possible to generate multiple calibration curves, each associated with a particular wavelength, as shown in **Figure A-4**. It is noticed that at higher wavelengths, there is a stronger correlation between the absorbance of free CNTs in the supernatant with the initial free CNTs added to the polymer debris; this is associated with a lower limit of detection (LOD). This suggests that the subtraction of UV signal of polymer debris is more accurate at higher wavelengths because of the low absorbance of the polymer signal in this range.

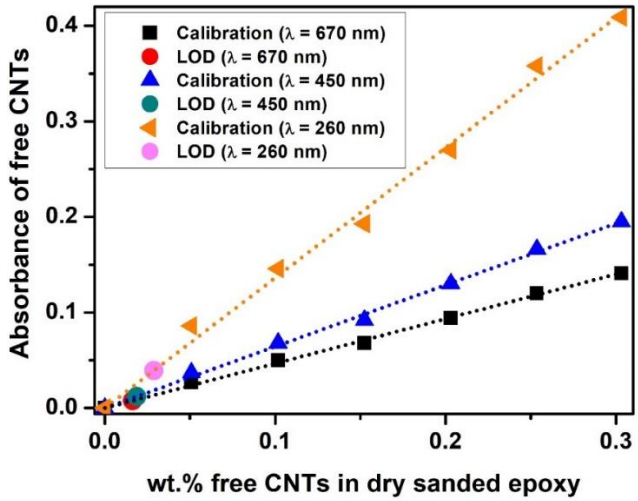

Figure A-4. Calibration curves relating absorbance of free CNTs at different wavelengths in the supernatants with total wt.% CNTs (same source) added to 0.10 g portions of the debris of sanded epoxy. Reprinted with permission from reference [217], Copyright 2019 Elsevier Ltd.

In order to use the method, three different CNT-epoxy composites with varying CNT wt.% were prepared and characterized for their dispersion status. **Figure A-5** shows the scanning electron microscopy (SEM) images of the fractured surfaces of the composites. CNT aggregates are clearly observed on the surface which indicate that the CNTs are not well dispersed in the composites. Note that it is still not well known whether poorly dispersed CNTs in composites would release more free CNTs as compared to well dispersed CNTs due to the contradicting prior reports.[208, 225]

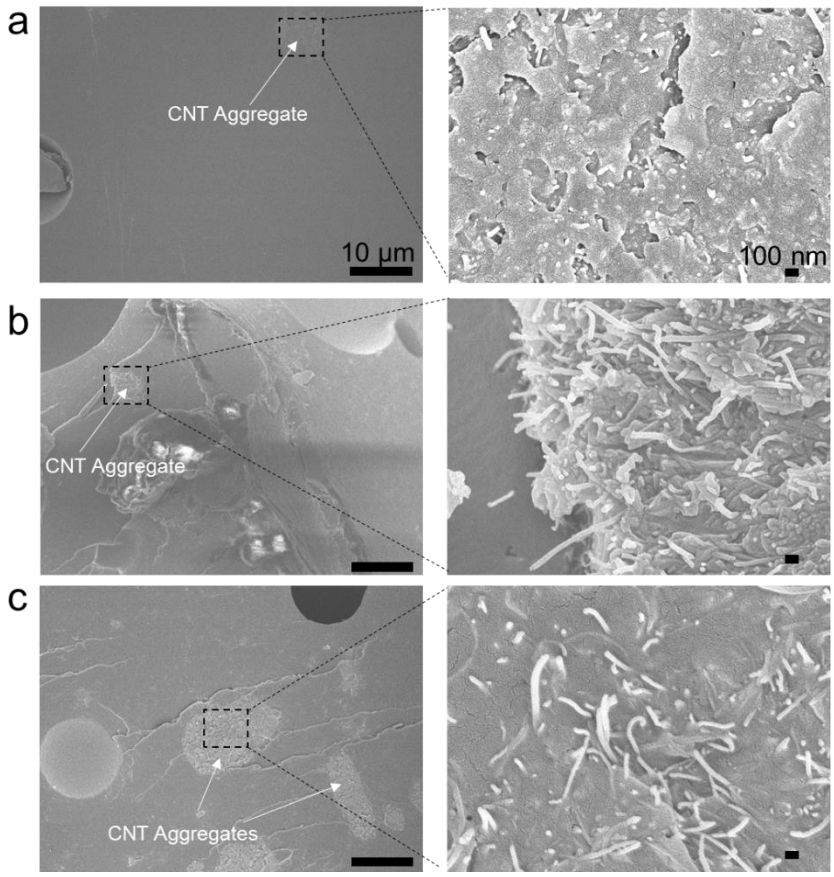

Figure A-5. Scanning electron microscope (SEM) images of fractured surfaces of (a) 1 wt.% CNT-epoxy composite; (b) 2 wt.% CNT-epoxy composite; and (c) 4 wt.% CNT-epoxy composite. Reprinted with permission from reference [217], Copyright 2019 Elsevier Ltd.

The epoxy composites were sanded and the debris generated were analyzed for free CNT content. Using the absorbance at 670 nm and the calibration curve, we detected 1.5×10^{-2} wt.% free CNTs in 0.10 g debris of 1.0 wt.% composite (note that the average is comparable to the statistical LOD), 2.2×10^{-2} wt.% free CNTs in 0.10 g debris of 2.0 wt.% composite, and 4.2×10^{-2} wt.% free CNTs in 0.10 g debris of 4.0 wt.% composite as given in **Figure A-6**. The data show that the wt.% free CNTs are proportional to wt.%

CNTs embedded in the composite. Variations in free CNT content of the replicates of the same composites were observed due to the CNT dispersion quality of the composites and the amount of mechanical energy experienced by the composite during sanding [208]. Note that the released MWCNTs after abrasion of nanocomposites might be shorter than the original MWCNTs used for calibration. However, the calibration can still be used because well-dispersed (free) MWCNTs have been found to have the same absorption coefficient independent of the CNT length [209].

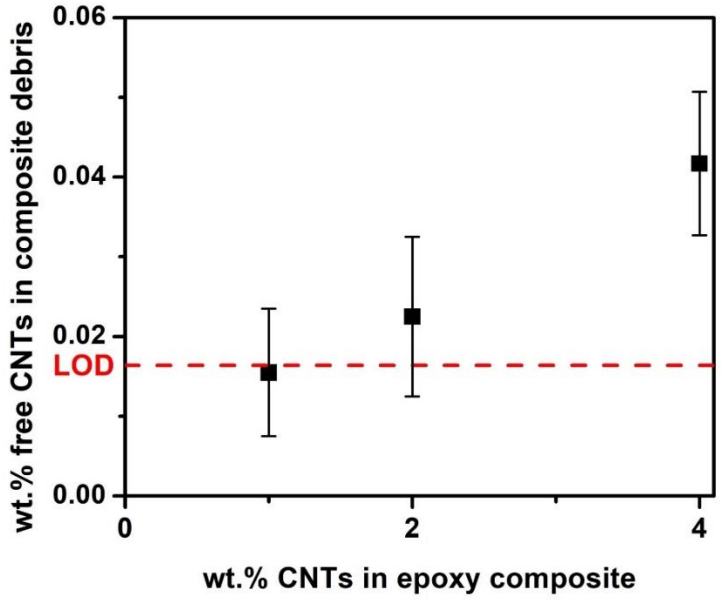

Figure A-6. Wt. % free CNTs detected in 0.10 g debris of sanded 1.0 wt.%, 2.0 wt.%, and 4.0 wt.% CNT-epoxy composites. (Using calibration curve at λ = 670 nm). Reprinted with permission from reference [217], Copyright 2019 Elsevier Ltd.

Since the supernatant of 4.0 wt.% CNT-epoxy composite showed the highest free CNT presence, it was also analyzed via SEM in order to provide a direct evidence of free CNT presence. **Figure A-7** shows the SEM images of vacuum-filtered film of the supernatant in which free CNTs can be clearly seen. This confirms that the UV-vis spectroscopy is a reliable technique to quickly detect free CNTs.

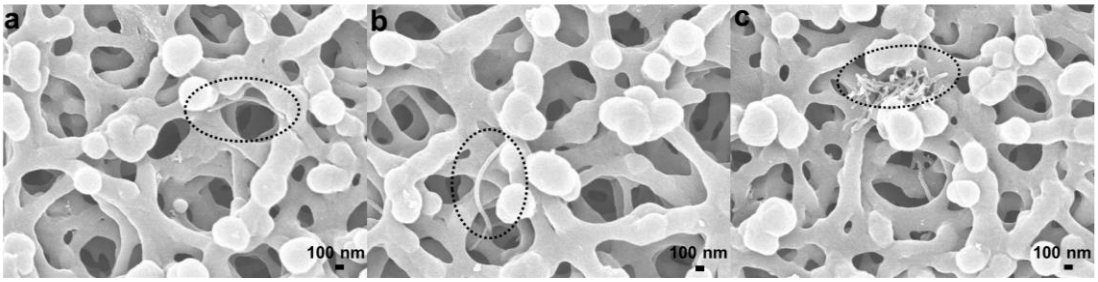

Figure A-7. Scanning electron microscope (SEM) images of vacuum-filtered film of the supernatant obtained using 4.0 wt.% CNT-epoxy composite debris. Note that the porous background is due to the polysulfone filter. Reprinted with permission from reference [217], Copyright 2019 Elsevier Ltd.

Prior reports have confirmed release of free CNTs after sanding of CNT-epoxy composites. For example, Schlagenhauf *et al.*[198] used Transmission Electron Microscopy (TEM) and found free CNTs after sanding (using Taber Abraser) of 1.0 wt.% epoxy composite. Huang *et al.*[226] also used TEM to observe free CNTs released after sanding (using sandpaper and disk sander) of 1.0 – 4.0 wt.% epoxy composites and found free CNTs in the debris of 4.0 wt.% composite. The only study that quantified free CNTs after sanding of epoxy composite is by Schlagenhauf *et al.*[208]. In that study, the CNTs were labeled with lead ions prior to 1.0 wt.% composite production and the composite was then sanded using a Taber Abraser. The sanded composite debris was immersed in 0.1 M nitric

acid (HNO_3) and sonicated for 30 min. The concentration of released lead ions was then measured using ICP-MS which was correlated to free CNT content via a calibration. Based on the concentration of lead ions, the worst-case scenario free CNT content was determined to be 4.0 x 10^{-3} wt.% in 1.0 g debris (40 μg free CNTs) of 1.0 wt.% epoxy composite which would also be easily detected by our method because the free CNT content is above the detection limit (1.6 x 10^{-2} wt.% in 0.10 g debris, 16 μg free CNTs). Note that the difference in CNT contents may be primarily due to the different type of CNTs used in this study and the study by Schlagenhauf *et al.*[208]. We show later that the slope of the calibration for free CNT quantification using UV-vis spectroscopy is significantly affected by the type of CNTs. In addition, other factors such as the type of epoxy matrix, nanocomposite preparation technique, and the sanding method may also affect the amount of free CNTs that are released during the abrasion process.

We have shown here that the epoxy matrix is prone to releasing free CNTs and our approach is simple and quick in quantifying free CNT content compared to other methods.

Free CNT Release from Anti-corrosive Paint

CNTs have also shown to enhance anti-corrosive properties of paints, [227-228] which have led to their use in commercial products.[206, 213] We applied our method to assess release of CNTs from anti-corrosive paints manufactured by Tesla Nanocoatings, Inc. In order to mimic a real-life release scenario, the paint was first UV-weathered at an accelerated rate for a time equivalent to useful lifetime of the paint. The weathered paint

was then removed from the steel panels via sandblasting. The debris generated contained the paint and the sandblast media and was analyzed for detection of free CNTs.

Since the debris contained a significant amount of sandblast media, it is important to have a calibration that can detect CNTs in large amounts of debris. **Figure A-8** shows the calibration curve for free CNT detection in 10 g debris. The strong linear correlation ($Abs_{670} = 88C_{CNT}$, $R^2 = 0.99$) shows that the calibration is possible even in the presence of significant amount of other solids. The detection limit of free CNTs in 10 g debris consisting of UV-weathered paint and sandblast media was determined to be 1.3×10^{-4} wt.%.

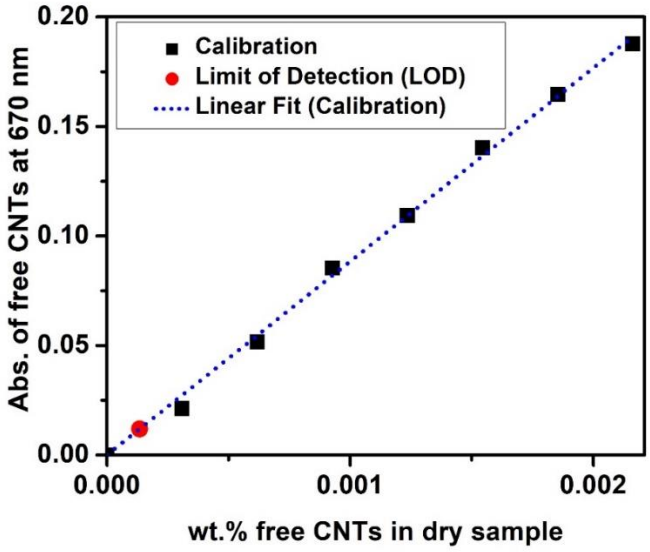

Figure A-8. Calibration curve relating absorbance of free CNTs in the supernatants with total wt.% CNTs added to 10 g portions of the debris of sandblasted weathered anticorrosive paint. Reprinted with permission from reference [217], Copyright 2019 Elsevier Ltd.

The calibration curve was used to determine free- CNT content in the debris of CNT-loaded paint. Using the absorbance at 670 nm and the calibration curve, we did not detect any free CNTs above the LOD in all replicates of the debris of CNT-loaded paint. (Note that the information about total embedded CNT content in the paint is proprietary).

It has been reported previously that UV-weathering of CNT-based composites degrades the polymer matrix on the surface; therefore, exposing a densified layer of CNTs [229-230]. This dense and entangled layer of CNTs prevents further degradation of the matrix underneath and has a strong resistance to release due to either strong van der Waals interaction or the possibility that part of the CNTs in the exposed layer are still embedded in the matrix [230-231]. Since the paint was UV-weathered prior to removal via sandblasting, it is possible that no free CNTs are released at all or very small amount of free CNTs are released that is below the statistical detection limit. Recently, Brame *et al.* [203] assessed free CNT release from the same type of paint after sanding (using Taber Abraser) the UV-weathered paint. Scanning electron microscopy (SEM) was used to analyze the paint debris and no free CNTs were found after extensive SEM analysis. However, it was not possible to conclude that free CNTs are not released at all because SEM analysis uses very small amounts of samples and significantly large number of images need to be analyzed before making a definitive statement about CNT release [232]. In contrast to inconclusive free CNT detection analysis, our method here rapidly gives reliable information that no free CNTs are present above 1.3×10^{-4} wt.% in 10 g debris of paint generated after end-

of-life paint removal via sandblasting. This is useful for both industries and risk assessors in evaluating the CNT exposure potential of CNT-based products.

Free CNT Release from PLA Filament Coating

Polymer filaments commonly used in additive manufacturing are now coated with CNT-composites to enhance the strength of the printed structures [233-234]. There are huge questions facing the three-dimensional (3-D) printing companies like Essentium, Inc. [185] about whether the free CNTs would be released from the CNT-loaded filaments during abrasion. Therefore, as a relevant simple release scenario, we used a file for abrading commercial CNT-PLA coated filaments and applied our method to detect and quantify free CNTs in the debris.

The calibration curve generated by adding known amounts of free CNTs to the filed PLA debris is shown in **Figure A-9**. The absorbance of free CNTs at 670 nm and the total free CNT content in the debris are directly correlated ($Abs_{670} = 1.26C_{CNT}$, $R^2 = 0.99$) for PLA as well. The detection limit of free CNTs in 0.10 g of filed PLA debris was determined to be 2.5×10^{-2} wt.%.

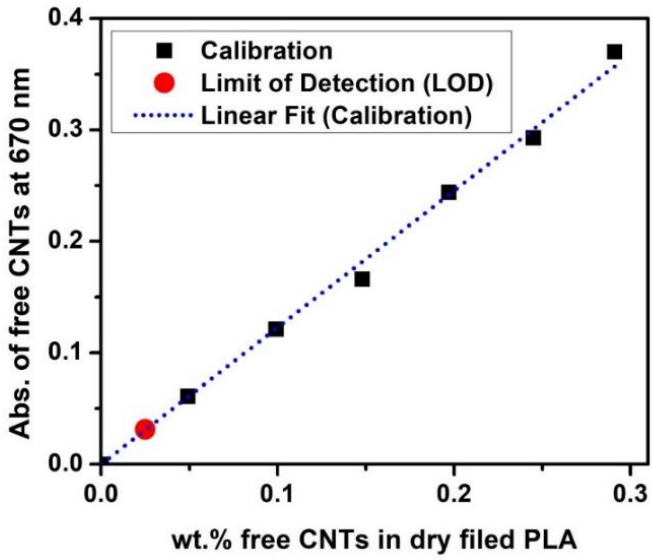

Figure A-9. Calibration curve relating absorbance of free CNTs in the supernatants with total wt.% CNTs added to 0.10 g portions of the debris of filed PLA. Reprinted with permission from reference [217], Copyright 2019 Elsevier Ltd.

We analyzed debris of two different commercial CNT-PLA filament coatings for free CNT presence. Both coatings are CNT-PLA composites near the percolation threshold. (Note that the information about CNT loadings in these coatings is proprietary). Using the calibration curve and the absorbance at 670 nm, we did not detect any free CNTs above the LOD for both coatings.

Overall, we tested three different products and did not detect free CNT release in two of them. These results help clarify several uncertainties associated with the method. For example, it is possible that the debris particles with embedded CNTs may be present in the supernatant (**Figure A-2 b-c**). If this is the case, then the debris with embedded CNTs would show a different UV-vis signature than the debris without CNTs (used as a

baseline in the calibration) and would result in a false positive if no free CNTs are actually present. Since no false positives were observed in two of the scenarios tested, it shows that this uncertainty is not prominent.

Moreover, it is also possible that the tip-sonication of abraded nanocomposite debris may release additional free CNTs during the process which would result in an overestimation of free CNT content. However, the fact that the method gives negative results (no detection in CNT-loaded paint and PLA) indicates that free CNTs are not being artificially released. Note that this limitation does not affect the overall technique significantly and given the lack of other reliable techniques for quick detection and quantification, this method still has the potential to be accepted as an industrial standard.

In addition to the composites and commercial CNT-based products tested here, this method is applicable to many other CNT-based products. However, a new calibration curve is needed for each different product being tested because the calibration slope is affected by the type of CNTs embedded in the product. **Figure A-10** shows the calibration curves generated by adding known amounts of free CNTs from two different sources to the debris of filed PLA. These calibrations have different slopes not because of the different absorption coefficient of CNTs; rather it is that CNTs may vary in dispersibility due to differences in purity, number of walls, and aspect ratio which affect the fraction of CNTs retained in the supernatant and thus the absorbance [209]. Therefore, it is important to generate calibration curves using the same type of CNTs as those used in the composites being analyzed for free CNT release. Additionally, note that **Figures A-11 and A-12**

confirm that the slope of the calibration is not affected by the type of the matrix and the release scenario. This makes it possible to have a universal calibration curve that can be used to detect free CNT release from different composites as long as the type of CNTs remain the same.

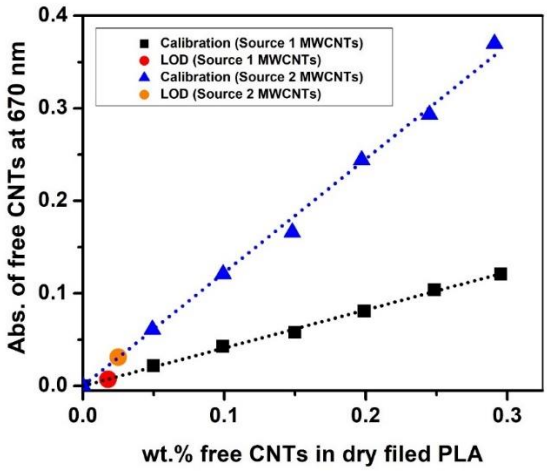

Figure A-10. Calibration curves relating absorbance of free CNTs in the supernatants with total wt.% free CNTs (two different sources) added to 0.10 g portions of the debris of filed PLA. Reprinted with permission from reference [217], Copyright 2019 Elsevier Ltd.

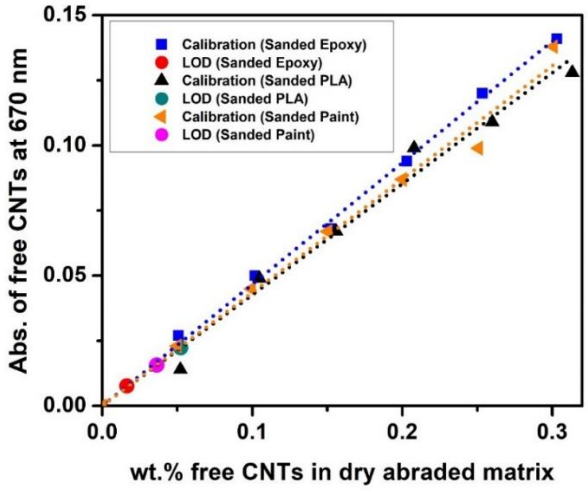

Figure A-11. Calibration curves relating absorbance of free CNTs in the supernatants with total wt.% free CNTs (same source) added to 0.10 g portions of the debris of sanded epoxy, PLA, and paint. Reprinted with permission from reference [217], Copyright 2019 Elsevier Ltd.

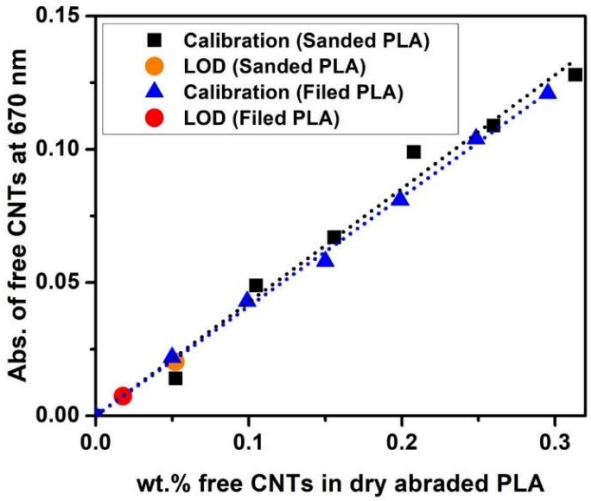

Figure A-12. Calibration curves relating absorbance of free CNTs in the supernatants with total wt.% free CNTs (same source) added to 0.10 g portions of the debris of sanded and filed PLA. Reprinted with permission from reference [217], Copyright 2019 Elsevier Ltd.

Conclusions

We have shown here that the UV-vis spectroscopy can be used to rapidly detect and quantify free CNTs in the debris of abraded nanocomposites. Since a calibration is crucial to determine free CNT content, we presented a simple procedure to generate calibration curves which takes into account the presence of polymer matrix in the debris to accurately quantify free CNTs.

We analyzed debris of various sanded CNT-epoxy composites and detected free CNTs above the detection limit of 1.6×10^{-2} wt.% (in 0.10 g debris). We also determined that no free CNTs are present above 1.3×10^{-4} wt.% in 10 g debris of CNT-based anticorrosive paint after end-of-life removal via sandblasting. Finally, we also found that when CNT-PLA coatings on commercially available 3D printer PLA filaments are filed, no free CNTs are released above the detection limit of 2.5×10^{-2} wt.% (in 0.10 g debris).

Overall, our method is reliable and quicker than any other method currently available to quantify free CNT content. It offers risk assessors and industrial hygienists a novel tool for rapidly characterizing the environmental and occupational exposure potential of CNTs in different products. Additionally, the quantitative information obtained regarding free CNT content can be included in the product safety data sheet (SDS) which has not been possible so far. Lastly, this method can also be potentially used for detecting and quantifying release of other graphene-family materials from composites.